Fall 2010

Functionalized silica nanostructures for biosensing applications

Hector Nuno
San Jose State University

Follow this and additional works at: https://scholarworks.sjsu.edu/etd_theses

FUNCTIONALIZED SILICA NANOSTRUCTURES
FOR BIOSENSING APPLICATIONS

A Thesis

Presented to

The Faculty of the Department of Chemical and Materials Engineering

San Jose State University

In Partial Fulfillment

of the Requirements for the Degree

Master of Science

by

Hector Nuño

December 2010

The Designated Thesis Committee Approves the Thesis Titled

FUNCTIONALIZED SILICA NANOSTRUCTURES
FOR BIOSENSING APPLICATIONS

by

Hector Nuño

APPROVED BY THE DEPARTMENT OF CHEMICAL AND MATERIALS
ENGINEERING

SAN JOSE STATE UNIVERSITY

December 2010

Dr. Melanie McNeil   Department of Chemical and Materials Engineering

Dr. Roger Terrill   Department of Chemistry

Dr. Robert Miller   IBM Almaden Research Center

Dr. Joseph Sly   IBM Almaden Research Center

ABSTRACT

FUNCTIONALIZED SILICA NANOSTRUCTURES
FOR BIOSENSING APPLICATIONS

By Hector Nuño

This work covers both two dimensional (2D) and three dimensional (3D) silica-based nanostructures for use in biomedical sensing applications. The first section of this study discusses the formation of 2D nanostructured surface plasmon resonance (SPR)-based biosensor substrates. The surface of these biosensors was nanostructured by adding sacrificial star polymers or block copolymers to a silicate precursor solution. Subsequent vitrification resulted in two distinct morphological patterns: random and ordered porosity. Amino groups on the surface of the biosensors enabled the installation of analyte receptors and antifouling agents such as oligo (ethylene oxide).

The second section discusses the development of 3D core-shell silica nanoparticles (SNPs). For this work, star polymers were generated to provide hydrophobic interiors capable of sequestering large hydrophobic porphyrinoid dyes and hydrophilic exteriors capable of templating the growth of silica shells. The diameter of the SNPs (25–100 nm) varied depending on reaction time, template size, and reagent concentration. The shell thickness was also controlled in order to either release or retain the hydrophobic dyes. The SNPs were surface-functionalized with biocompatible "stealth" materials such as poly (ethylene oxide) to generate non-toxic, water-soluble nanoparticles for the *in vivo* delivery of various hydrophobic imaging and therapeutic materials.

ACKNOWLEDGEMENTS

TABLE OF CONTENTS

LIST OF FIGURES

LIST OF TABLES

CHAPTER ONE
INTRODUCTION

In the last twenty years, there has been significant interest in the development of 2D ultrasensitive biosensors to detect medically important biomolecules or other chemicals. There are a variety of optical methods to detect and quantify chemicals and biological molecules, such as spectroscopy, ellipsometry, interferometry, and surface plasmon resonance (SPR) [1]. Recently, scientists have developed increasingly complex 3D silica nanoparticles that perform a wide range of tasks, including biosensing, drug delivery, and intracellular imaging [2, 3].

This study examines the development of SPR biosensors as an *in vitro* approach in conjunction with the application of physical and chemical parameters to improve the overall sensitivity and selectivity of the biosensor. Using this method, biological reactions can be detected in real time without the use of labels or tags [1]. SPR allows the analysis of a wide range of molecules, such as drugs, cofactors, proteins, and nucleic acids. SPR detection is independent of the chemical characteristics of the target molecules [1, 4]. This 2D method of constructing biosensors was modified to generate templated 3D silica nanoparticles (SNPs) by an *in vivo* approach.

This study also investigates the development of particles affected by different parameters such as size, peripheral functionality, water solubility, cargo release, and capability to encapsulate organic dyes. These templated SNPs with core-shell architecture are engineered to be multifunctional and can potentially be used in biological imaging, drug delivery, catalysis, and as biological sensory agents [2, 5].

1.1 Surface Plasmon Resonance

A typical SPR setup uses a prism of specific glass material and a thin film of a noble metal applied onto the glass substrate. In addition, a light source and a set of optical devices are needed to polarize and focus the laser beam. The light beam is directed through the prism; when it hits the metal, excitation of free electrons occurs. At the resonance angle, surface plasmons resonate with the energy of the light, minimizing the reflected intensity. A light detector measures the reflected intensity, which is recorded graphically on a PC. A refractive index matching fluid (RIMF) is applied between the prism and the glass substrate to exclude trapped air, so that a continual optical coupling of the light with coherent plasmonic responses exists [6].

1.1.1 History

The first observation of the surface plasmon phenomena was made in 1902 by Woods, who observed irregularities in the spectrum of the light diffracted by a metallic grating [7]. In the late 1960s, researchers demonstrated that plasmons could be generated by the excitation of metal surfaces by attenuated total reflection. The researchers concluded that the diminishing energy involved the excitation of conducting electrons, which created a phenomenon called plasma oscillation. The researchers demonstrated that plasma oscillations were affected by material applied onto the surface. In the 1970s, researchers termed this phenomenon "evanescent waves" due to the exponential decay of the waves with distance [8, 9]. In the early 1980s, Liedberg *et al.* [10] successfully used SPR as a biosensing tool. Since then, scientific progress has led to the development of better SPR-sensing devices. Currently, more than 75% of scientific articles that focus on

biosensing research involve SPR-sensing devices for detecting biomolecular interactions [1].

1.1.2 SPR Theory

As light passes through a medium with a higher refractive index to a medium with a lower refractive index, the light beam bends away from the normal axis [11]. Figure 1 shows several beams of light at different angles going through two different mediums, one with a high refractive index (blue area) and the other with a lower refractive index. As the angle of the incident light changes, part of the light is transmitted and part of the light is reflected, as shown by the red light beams (a) and (b) in Figure 1. When the angle of the incident light is greater than the critical angle (θ_c), all of the light is reflected, as shown by the red light beam (c) in Figure 1[11]. In order to use SPR effectively as a biosensing tool, the angle of the incident light must be greater than the critical angle.
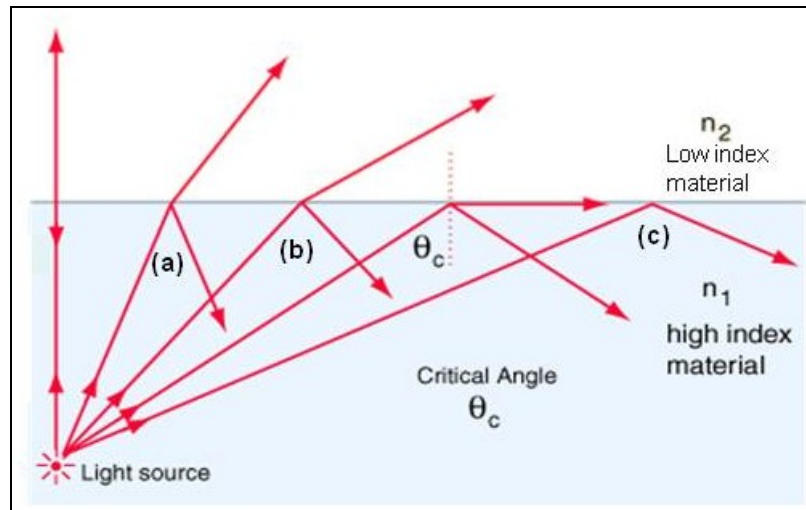
Figure 1. Total internal reflection [11] (reprinted with permission from HyperPhysics).

A plasmon is generated when a beam of polarized light under total internal reflection (TIR) is directed through a prism and strikes the surface of the metal [9]. These plasmons are charge density oscillations of free electrons; the electromagnetic wave (EMW) normally propagates along the metal to the dielectric interface. This EMW decays exponentially with distance [12, 13]. If the light electromagnetic vector matches the propagation constant of the metal, then the light vector couples with the metal surface, generating a surface plasmon. However, if the wave number of the light is smaller than the propagation constant at the metal dielectric interface, a surface plasmon cannot be excited. A prism is the ideal tool with which to overcome this problem because it enhances and couples the electromagnetic light wave with the propagation constant and allows for the excitation of surface plasmons [1, 7]. Using the method of attenuated total reflection, light passes through the prism and the light is totally reflected, generating an evanescent wave that penetrates the thin metal across the dielectric. The propagation constant of the thin film can be coupled with the surface plasmon by adjusting the angle of incidence of the light. If the following conditions in Equation 1 are met, then the evanescent wave can be coupled to the surface plasmon. In Equation 1, θ is the angle of incidence of the light, n_p is the refractive index of the prism, and β is the propagation constant of the surface plasmon [1, 7, 12].

$$(2\pi/\lambda)\, n_p \sin\theta = Re\{\beta_{SP}\} \qquad\qquad \text{Equation 1}$$

Various metals can be used to excite the plasmon, but gold and silver are most commonly used [13]. Figure 2 shows a common SPR apparatus with its sensorgram

graphs displaying the angular shifts taken at two different times and different conditions

[14]. The sensor substrate in this setup has two main components: a glass attached to the

prism and a thin film of metal permanently fused to the glass.
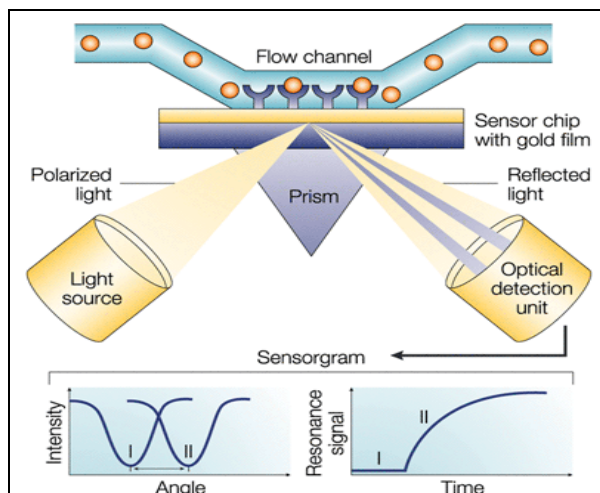
Figure 2. A representation of an SPR biosensor setup. The main components are: the light source, the prism, the SPR substrate, the flow cell, and the light detector [14] (reprinted with permission from Nature Publishing Group).

1.1.3   Surface Plasmon Resonance Sensors

As stated in Section 1.1.2, plasmons are excited when a beam of light passing

through a high refractive index (RI) prism hits a noble metal. This wave propagation has

a signature resonance angle that is accurately recorded by the detector in the SPR setup.

Any slight modification on the surface of the metal changes the refractive index of the

substrate, yielding a different resonance signal. The SPR can pick up these small changes

accurately, making the SPR a powerful sensory tool. A typical SPR biosensing study

uses a solution of target analytes, which adheres to specific binding sites on the surface of

the SPR biosensor. Thiolates can anchor to the gold surface, and recognition elements

(RE) can be attached to the thiolates [15]. Attaching analytes to the RE changes the

refractive index and the resonance angle. These changes are recorded; the angular shifts are compared to SPR standards without the attached analytes [16]. Due to the high sensitivity of these sensors, they are an essential tool for sensing a range of molecules and cells such as pathogens, toxins, drugs, vitamins, proteins, and biomarkers [7, 13].

1.2   Methods for Silica Formation and Nanoparticles

Approximately 60% of the earth's crust is silicon dioxide, which may be present in free form or combined with other elements to form silicates. This makes SiO_2 one of the most abundant compounds on earth, even more abundant than carbon [17]. Furthermore, silica has been the basis of one of the oldest industries of humankind: the ceramics and glass industry. In fact, interest in the sol-gel process arose in the mid-1800s during the processing of inorganic ceramics [17, 18]. The process of producing glass or ceramics involves the following steps: making the sol, drying the gel, and heating the material. At elevated temperatures, the particles fuse together to make either glass or ceramic, depending on the composition of the material [19]. Scientists have focused on the first step of this procedure, and the sol-making step was transferred from industry to the lab. After intense investigations of this step, the sol-gel method became one of the most popular methods for making colloidal silica nanoparticles [19].

1.2.1   The Sol-Gel Process

A sol is composed of two phases: a solid phase of suspended particles usually in colloidal sizes (1-100 nm), and a liquid phase in which the particles are suspended. A sol is usually stable as a solution due to the small size of the particles, but if the particles

6

aggregate, they may precipitate. During the precipitation process, the particles make a

three-dimensional continuous network, and the sol loses its mobility but maintains its

shape without the need for a mold. When this phenomenon occurs, the sol has formed

into a solid gel [18, 19]. The sol-gel process is a chemical solution procedure employed

to make silica with materials that have metal oxides as the basis for their composition. In

the 1950s and 1960s, this method was utilized to make different ceramic oxide

compositions that involved aluminum, silicon, or titanium [18]. During this time, work

by Iler [17] in silica chemistry demonstrated that colloidal size silica nanoparticles were

obtainable under acidic conditions from silicon alkoxide precursors. As shown by

Equation 2, the mechanism for particle formation was hydrolysis of the silicon alkoxide

precursor. This hydrolysis generated silicic acid $Si(OH)_4$, which condensed into

polymers of SiO_2 networks, as illustrated by Equations 3 and 4 [18, 19].

Equation 2

Equation 3

Equation 4
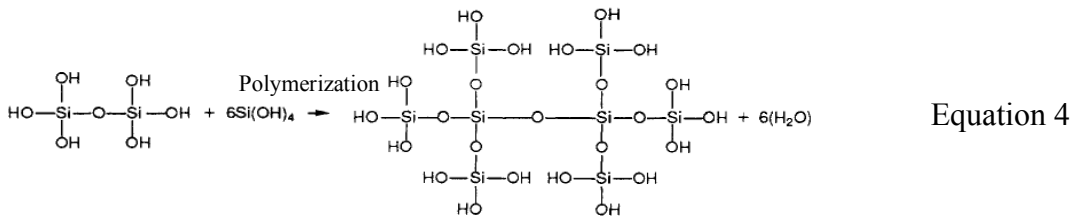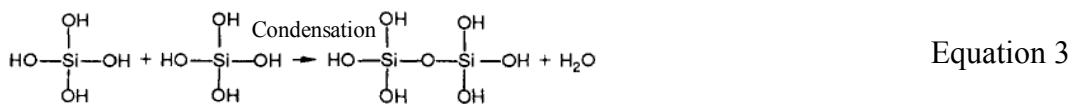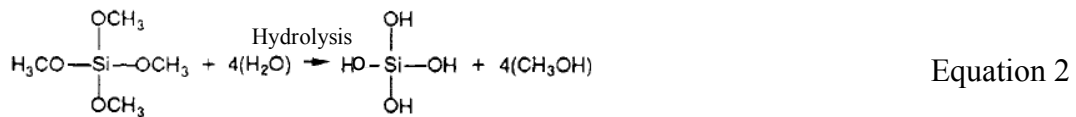
The formation of metal oxide requires connecting the metal center with an oxo

linkage (Si-O-Si) or a hydroxyl group (Si-OH) to form rigid polymeric networks, whose

gelation morphologies range from discrete individual particles to continuous polymeric

7

networks [18]. The study by Iler [17] demonstrated that the surface of the particles

contained hydroxyl groups (also known as silanol groups), as shown in Figure 3(a).

Ravinovich [19] showed that the networks of the silica dioxide matrix contained pores, as

shown in Figure 3(b), and that the surface of the silica particles contained 6.6 (Si-OH)

groups per 11 nm^2. Because of these findings, researchers focused more on the sol-gel

transition, and more studies were performed to obtain homogenous particles of uniform

shape and size.
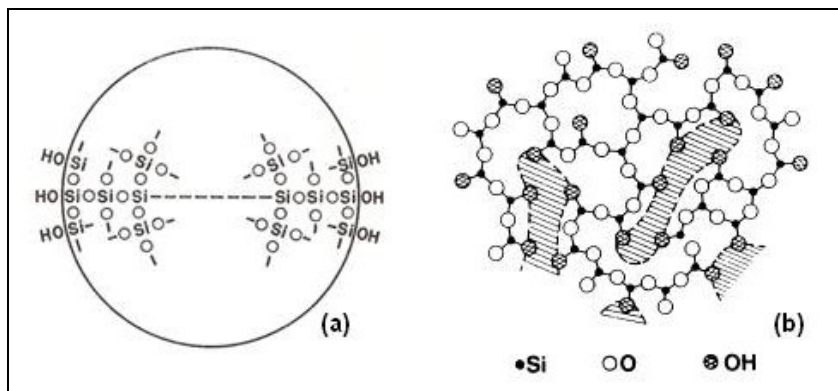
Figure 3. Representation of the surface of the silica particles (a) postulated by Iler [17].
The shaded regions (b) represent internal pores in the silica network that are common in
alkoxides sol-gel solutions [19] (used by permission of the publisher, Cornell University
Press).

Researchers discovered that homogenous particles had applications in hydrosol or

aerosol studies. As a result, the need to make sol solutions of uniform shape and size

greatly increased [17, 19].

1.2.2   Making Sols: The Stöber Method

Iler [17] showed that colloidal particles or sol solutions were produced by

adjusting the pH while reacting tetraalkyl silicates. In 1956, Kolbe [20] demonstrated

that silica nanoparticles could be obtained by reacting tetraalkyl silicates in various

alcoholic base solutions. Exceptionally pure reactants were needed in order to obtain

uniform spherical silica particles; the reaction was slow, and reproducibility was poor.

Then in 1968, Stöber and Fink [21] extended the findings of Iler and Kolbe, and after

some notable changes in experimental conditions, monodispersed silica particles were

obtained. The authors used ammonia as the catalyst and tetramethylorthosilicate (TEOS)

as the silica precursor in ethanol (EtOH) solutions. They varied the concentrations of

water and ammonia to obtain uniform monodispersed solid silica spheres. Equation 5

shows the hydrolysis, condensation, and polymerization of the silica precursor in the

presence of ammonia.

$$Si(OEt)_4 \xrightarrow[\text{EtOH}]{\text{NH}_4\text{OH}} Si(OH)_4 \xrightarrow{\text{Polymerization}} \begin{array}{c} \text{-Si-O-Si-} \\ \text{O} \quad \text{O} \\ \text{-Si-O-Si-} \end{array} + H_2O \qquad \text{Equation 5}$$
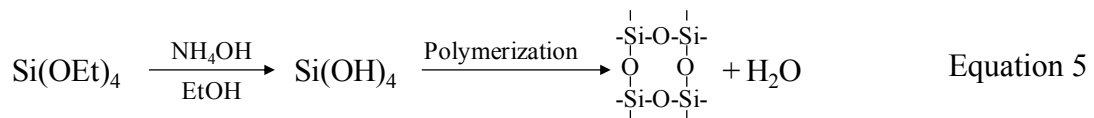
When the reaction conditions were varied, the resulting spherical silica particles

ranged between 0.05 and 1.7 μm in diameter. These particles were termed Stöber

spherical silica particles; the name "Stöber Method" originated from this terminology

[18, 21]. Figure 4(a) shows the uniform monodispersed silica nanoparticles in ethanol

obtained from the precursor TEOS and the ammonia catalyst. Stöber and Fink

demonstrated that the particle size was controlled by varying the ammonia concentration

and water (Figure 4(b)). The concentration of the silica precursor TEOS was kept

constant at 0.28 mol/liter, while the concentration of ammonia was varied up to 8

mol/liter. The highest diameter particles were produced at the highest concentration of

ammonia and at water concentration of 6 mol/liter [21].
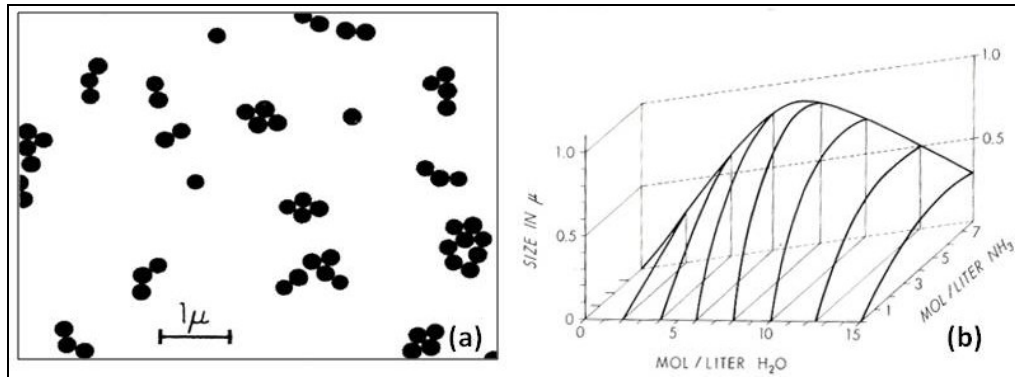
Figure 4. Electron micrograph (a) of silica particles obtained from an ethanol solution with TEOS as the silica precursor and ammonia as the catalyst. Graph (b) shows the particle size distribution obtained by varying ammonia and water, with constant TEOS concentration [21] (reprinted with permission from Elsevier).

In the late 1980s, Bogush *et al*. [22] mentioned that the previous work by Stöber was difficult to reproduce. The Bogush group stated that the graphical results produced by previous researchers in the sol-gel silica spheres system were difficult to read and covered limited concentration ranges. The Bogush group presented an extensive study on hydrolysis of TEOS in ethanol solutions containing ammonia and gave detailed experimental data of the reagents. Furthermore, they also included the influence of temperature on particle synthesis and mentioned that agitation of the reaction did not affect the particle size and distribution. As shown in Equation 6, they developed correlations to predict the final size of the spherical particles for a given set of TEOS, water, and ammonia concentrations. In Equation 6, d is the diameter of spherical particles; the concentrations of the reactants are given in mol/liter. The experimental data were plotted against the theoretical data as shown in Figure 5; the correlation had a 20% deviation [22].

$$d = A[H_2O]^2 \, exp(-B[H_2O]^{1/2})$$

with

$$A = [TEOS]^{1/2}(82-151[NH_3] + 1200[NH_3]^2 - 366[NH_3]^3$$

and

$$B = 1.05 + 0.523[NH_3] - 0.128[NH_3]^2$$
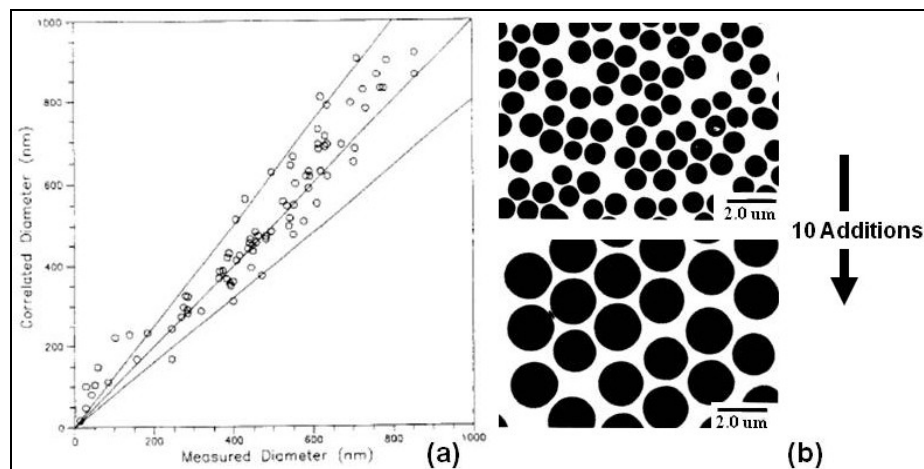
Equation 6

Figure 5. Correlation (a) between experimental data and theoretical data on the particle size by Equation 6 depicting 20% error in the fitting of the equation to the experimental data. Seeded method shown by the transmission electron microscopy (TEM) images (b) generated larger Stöber spheres [22] (reprinted with permission from Elsevier).

Another important experimental development by Bogush's group was an alternative method to increase the diameter of the particles. In this method, known as "seeded growth," a preformed silica particle was the template for additional silica deposition. Figure 5(b) shows the size increment of the seeded growth method after 10 additions of TEOS and water. These findings facilitated the production of Stöber silica spheres with different target sizes and permitted the use of simple experimental procedures to control the size of the particles by adding more reagents to the preformed Stöber silica spheres [22]. A decade later, Grun *et al.* [23] optimized the Stöber method

and used amphiphilic templating agents to generate mesoporous silica spheres. The researchers added the cationic surfactant cetyltrimethylammonium bromide (CTAB) to the hydrolyzing reaction of tetraalkoxysilane in ethanol and aqueous ammonia. The surfactant formed a micelle-like structure that functioned as the template and directed the formation of mesoporous silica spheres [23]. Since then, the modified Stöber method has been used to generate templated silica nanoparticles of different sizes and shapes. Currently, many inorganic templates, such as quantum dots, aluminum, gold, and silver seeds, can be encapsulated with silica. A few scientists have used organic templates, such as polystyrene latexes, or organic-based micelles, and coated these nanoparticles with silica [24-26]. Figure 6 reveals some of the applications of the Stöber particles, including bioimaging, therapeutics, sensing, and drug delivery [27].

Figure 6. Versatility of the silica particles generated by modified Stöber synthesis. Different materials, such as organic dyes, small proteins, and quantum dots, can be incorporated within the silica, and nanoshells can be grown outside the spheres [27] (reproduced by permission of The Royal Society of Chemistry).

Burns *et al*. [27] mentioned that the silica matrix serves as a physically and chemically stable vehicle that enhances and protects the properties of the encapsulating material, such as organic dyes, small proteins, and quantum dots. The emerging field of nanobiotechnology uses Stöber spheres to bond dyes into fluorescent core-shell architectures. Scientists have incorporated this technology into metal nanoshells, mesoporous structures, and chemical sensors. These multifunctional materials are also used in the fields of photonics, optoelectronics, and nanomedicine [27-29].

1.2.3   Biocompatibility of Silica Nanoparticles

Silicon and carbon are two elements that resemble each other in many ways, but have different roles in living creatures. Silicon, one of the most abundant elements on the planet, was once considered non-essential for most living things. On the other hand, carbon, which is less plentiful, is considered the most important primary element [17]. The biocompatibility of silica, according to Iler's theory, implies that the crystal pattern of silicate left an imprint on living matter millions of years ago. When life originated, silica played an essential role in the reproduction of organisms. Silicon (not in the elemental form) is present in all living organisms and serves an essential role in the structure of biomaterials, from single cell organisms to higher plants and animals [30]. As shown in Figure 7(a), diatoms, radiolarians, and bacteria use silica deposits to reinforce their cell walls. In plants (b), such as horsetail and bamboo, silica contributes to the rigidity of cell walls and increases resistance to parasitic pathogens [17, 30-32]. In humans (c), silicon is found in glands, teeth, skin, bones, and cartilage. In rats and

chickens, silicon deficiency can result in problems with connective tissue, bone

metabolism, collagen synthesis, and cartilage formation [33].
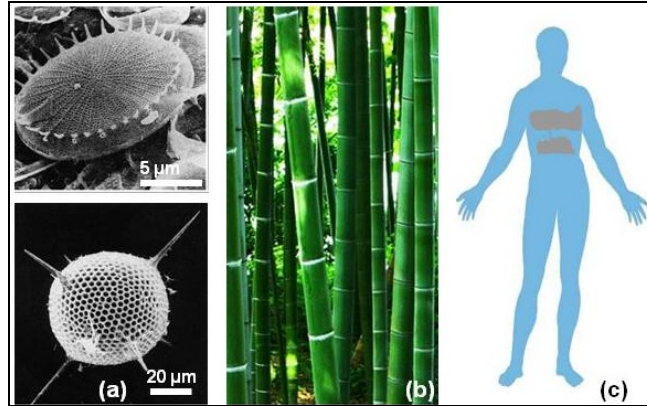
Figure 7. Organisms that contain silica. Single cell diatoms and radiolarians (a) have silica skeletons shown by the SEM images. Bamboo (b) uses silica for cell wall rigidity. The human (c) body utilizes silica in connective tissue, bones, glands, teeth, and skin [30, 32] (reprinted with permission from Springer).

Scientists have used the bio-acceptance of silica to construct and design silica-

based synthetic structures inspired by nature. However, to be applicable for biosystems,

these synthetic structures must be small enough to penetrate cell membranes and must

exhibit wettability, biocompatibility, long-term stability, low cytotoxicity, and *in vivo*

targeting efficacy [34, 35]. Silica nanoparticles possess these characteristics and have

been proven to be biocompatible without significant evidence of cytotoxicity. In a study

by Luo *et al.* [36], the authors designed a self-assembling DNA delivery system using

silica nanoparticles as vehicles for delivery. To test the cytotoxicity of their system, the

scientists incubated eukaryotic cells with silica nanoparticles with the transfection reagent

Superfect, and with both agents concurrently. As shown in Figure 8, from bottom to top,

cell growth proliferation remained constant when the amount of silica nanoparticles was

increased, but after 60 million/ml silica nanoparticles, the cell growth proliferated at

approximately 15%. The cell growth of the silica nanoparticles with the transfection

agent was inhibited, but this inhibition was due to the reagent and not to the silica

nanoparticles. There was no evidence of cytotoxic effects on the eukaryotic cells due to

the silica nanoparticles when they were incubated for 2 h or 24 h [36].
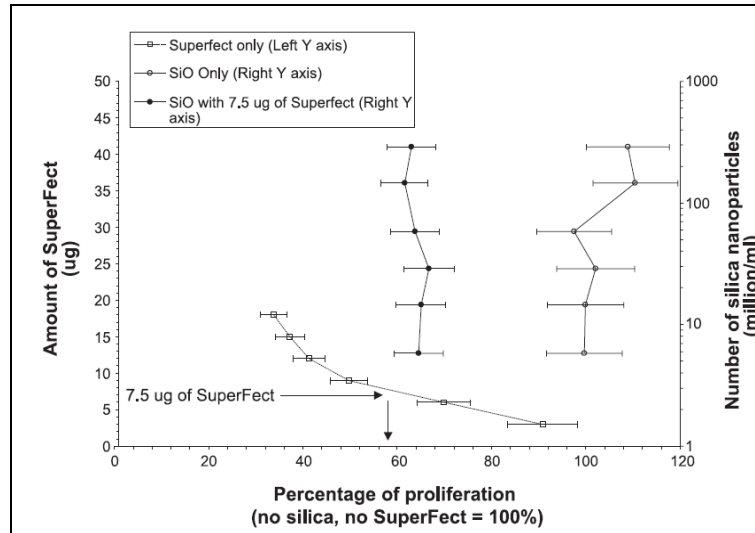
Figure 8. Cytotoxicity study (squares) of silica nanoparticles, Superfect (solid circles) transfection reagent, and silica nanoparticles (empty circles) in combination with the transfection reagent [36] (reprinted with permission from Elsevier).

Furthermore, Choi et al. [37] introduced fluorescent silica nanoparticles in mice

via tail-vein injection. They studied the cytotoxic effects of the particles and monitored

the location of the particles within the mice. For these studies, the fluorescent dye

tetramethylrhodamine isothiocyanate (TRITC) was incorporated within the silica core;

the dye functioned as an imaging probe. Necropsy fluorescence images (Figure 9(b,c))

revealed that the core-shell silica nanoparticles were found mostly in the spleen, lungs,

and liver; no abnormal clinical signs were detected in the mice. Not only did the

researchers find an absence of cytotoxicity at higher concentrations of the silica

nanoparticles, but sixty days after the injection, the particles were almost cleared from the body, as shown by the graph in Figure 9(a) [37].
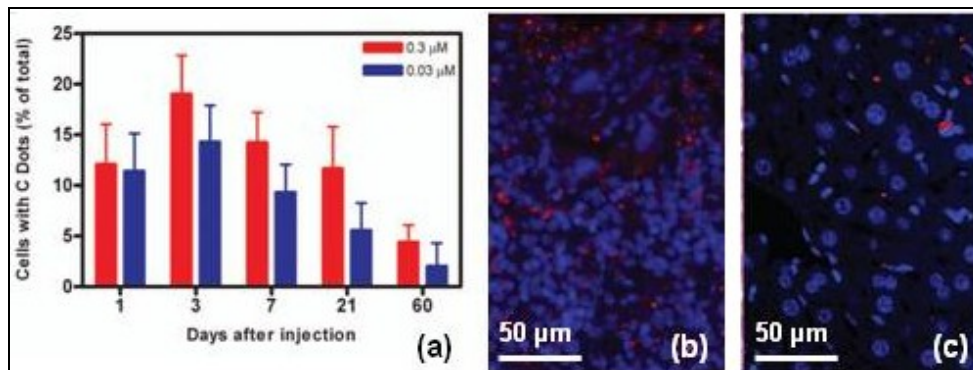
Figure 9. TRITC embedded silica nanoparticles biodistribution in mice. The fluorescent particles (a) began to clear after 60 days without any significant signs of cytotoxicity. The silica nanoparticles (b) were mostly found in the spleen, liver (c), and lungs, as shown by the fluorescence microscopy images [37] (reprinted with permission from SPIE).

The US Food and Drug Administration has recognized silica as a safe biocompatible material [2]. The synthetic generation of biocompatible complex silica nanoparticles has increased the number of medical applications. In the field of biotechnology, these complex particles function as probes for different applications, such as cell imaging and drug delivery [34-38].

1.3   Significance

Constructing and optimizing of ultrasensitive biosensors is very important in chemistry and in the biomedical field. One of the most important issues in modern medicine is the rapid and accurate *ex vivo* diagnosis of diseases. SPR biosensors offer an alternative method to diagnose diseases by accurately detecting disease-causing agents at low concentrations, resulting in earlier treatment of patients [13]. Furthermore, these

sensors can be used to detect low traces of harmful pollutants and pathogens [6, 38]. SPR biosensors are needed to detect and analyze different molecules in the areas of medicine, biotechnology, food science, and drug development; these biosensors are also used for military and civilian airborne biological and chemical testing [13].

Silica nanoparticles offer similar functionality, but an *in vivo* approach is employed. SNPs can be doped and internally functionalized with organic and inorganic materials. The surface of the SNPs can be modified to attach biomolecules or can be coated with metals such as gold to add different functions [2, 34]. Modified porous SNPs can be employed for targeted delivery of drugs that can kill cancer cells within minutes [39]. SNPs can also be combined with gold for cancer-targeted imaging and therapy using near-infrared (NIR) photothermal treatments. Alternatively, SNPs can be used as magnetic resonance imaging (MRI) contrast agents and as delivery and cell tracking probes to facilitate gene delivery and cell tracking. Modified SNPs in combination with other agents can be used in biosystems for medical diagnosis [2, 34-36].

CHAPTER TWO
LITERATURE REVIEW

SPR biosensors have been widely used as external detectors in many areas from drug discovery to gas detection. SNPs have been used as internal probes in nanotechnology and medical therapy as sensory elements, drug carriers, and imaging contrast agents [1, 2, 40]. Still, there remains a need to improve the sensitivity of the SPR biosensors. In the medical field, it is very important to detect disease-causing agents or metabolic molecules such as glucose at very low concentrations so that early treatment can be administered [38]. Three strategies show promise for improving the sensitivity and selectivity of the biosensors: the construction of SPR biosensor substrates, integration of a nonfouling and porous surface, and installation of specific biorecognition elements.

In the case of the SNPs, pure SNPs tens of nanometers in size can be synthesized by the Stöber process. However, constructing SNPs below 100 nanometers is difficult. A viable solution to this problem is to use organic or inorganic templates to generate small SNPs with multiple functionalities, featuring one kind of material inside and a different material outside [24]. The experimental conditions for making SNPs and the various templates are reviewed in this report. Important parameters such as cargo load and release, size control, and surface functionality are also investigated.

2.1   SPR Biosensors

2.1.1   Multilayer Substrate Assembly for SPR Uses

A key requirement for the construction of SPR biosensors is a well-engineered multilayer substrate. The noble metal, a source of the free oscillating electrons for SPR

18

measurements, must be chosen based on the nature of the experiment and on its metallic properties. Noble metals such as gold and silver are utilized to produce plasmons [12]. These metals are useful in SPR studies because they exhibit strong angular signals when wavelength numbers are within the range of the visible spectrum [40]. In these sensory studies, it is important to select the appropriate metal and technique to apply a thin layer of the metal, as the morphology of the thin film influences the optical properties of the SPR substrate [15]. There are several techniques to apply a thin layer of metal on the substrate, including vapor deposition, electroless deposition, and chemical sputtering. Physical vapor deposition is more expensive than electroless deposition, but is smoother than electroless by a factor of four [15]. Electroless deposition is less costly, since it requires only mixing of salts to produce the thin film, does not require a vacuum process, and can be used on nonconductive substrates [41]. On the other hand, physical vapor deposition generates smoother surfaces, produces chemical stability of the metal, and provides excellent SPR profiles [15, 41]. Figure 10 shows atomic force microscopy (AFM) images of thin films by physical vapor deposition and electroless metal deposition.
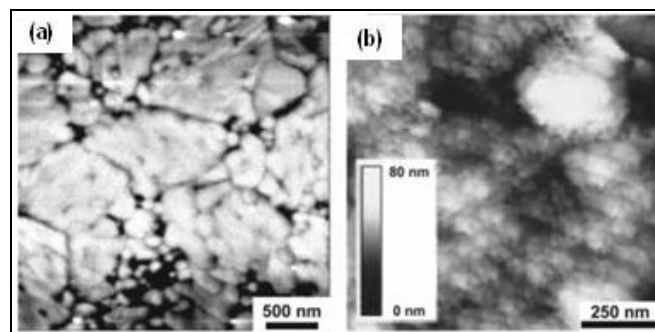
Figure 10. AFM images of gold deposition by thermal evaporation (a) and electroless deposition (b). Typically, electroless deposition is 4 times rougher than thermal evaporation [15] (reprinted with permission from American Chemistry Society).

Gold is the most studied and stable metal for general SPR studies because it is easy to use when creating thin films by physical vapor deposition, electroless deposition, or chemical sputtering. Most importantly, gold is an inert metal and does not oxidize or react with most chemicals [15]. Another notable property of gold is its strong affinity to thiolated compounds; as a result, thin films of gold are commonly used to generate self-assembled monolayers (SAMs) using thiolated compounds. This method of generating monolayers is commonly used in SPR studies. However, a different platform, such as a silica-based material on gold, offers an alternative that could elicit interesting physical and chemical approaches in SPR studies.

Szunerits *et al*. [42] used a multilayer approach to build SPR sensors; in addition, the researchers applied an extra layer of SiO_2 on top of the metal. The authors employed vapor deposition to deposit a 5 nm adhesion layer of titanium, a 50 nm layer of gold, and a 7-100 nm layer of SiO_2. The thickness of the layers was in agreement with that obtained in a study by Manera *et al*. [43]; however, the Manera group used chromium instead of titanium for the adhesive layer. Szunerits *et al*. observed that when more than 44 nm of SiO_2 was deposited, the SPR signal was lost, indicating the upper practical threshold of layer thickness. Another significant observation was that when the SiO_2 layer was only 7 nm thick, the plasmon intensity was the same as that obtained using naked gold [42]. Thus, the lower threshold of SiO_2 layer thickness of 7 nm maintained the original SPR intensity signal. The thickness of the SiO_2 layers was measured by SPR and ellipsometry, and characterization of the surface was performed by atomic force microscopy (AFM). Figure 11 shows the light intensity *vs*. incident angle as the layer of

20

SiO$_2$ was increased. As more material was applied, the resonance curves were shifted to the right, illustrating the sensory effect of this technique.
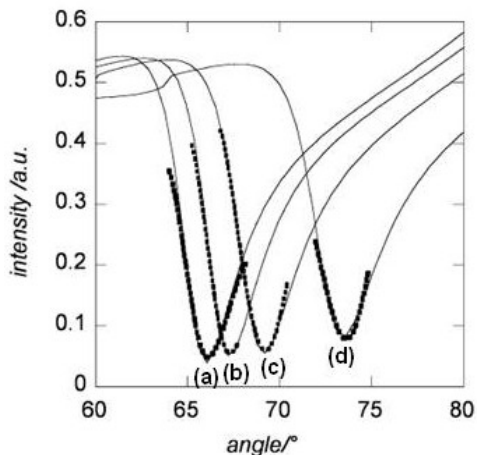
Figure 11. SPR of SiO$_2$ thickness study on a 50 nm gold and 5 nm Ti adhesion layer. SiO$_2$ thickness of zero nm (a), 20 nm (b), and 44.2 nm (c), and (d) is the fitting parameter curve [42] (reprinted with permission from American Chemistry Society).

The authors functionalized the surface with a piranha solution to expose reactive silanol groups; the surface became hydrophilic and more reactive. The researchers incubated the substrate in perfluoroalkylsilane at room temperature for 2 h to perform a silane coupling reaction. Contact angle measurements were taken before and after the silane coupling reaction, and the angles increased from 15º to 114º, confirming the successful functionalization of the silica surface [42].

2.1.2 Physical Nanostructuring of the Films

A porous surface can be applied onto SPR substrates to account for changes in physical parameters. These porous surfaces can be applied to the SPR substrate by spin coating or electrostatic self-assembly (ESA). Porous surfaces increase the surface area, providing the ability to incorporate receptor sites for biochemical reactions with their

21

corresponding analytes [44]. Porous surfaces have been applied to silica-based films, but often these films are thicker than the SPR evanescence wave and cannot be used for SPR sensory studies. Stephano *et al.* [45] used a porous silicon matrix 5000 nm thick to study interaction of L-glutamine to the binding protein. Wright *et al.* [46] mixed a phenol receptor into a porous 1000 nm thick silicate sol-gel film for detection of phenol *via* SPR analysis. The SPR evanescent wave can only penetrate a distance of 100 nm or 25-50% of the wavelength of the incident light; some of these studies used films that went beyond the size of the evanescent wave [46, 47].

Few researchers have explored functionalized porous nanostructured thin films for SPR sensory studies in the range of 20-100 nm film thickness. Researchers who have used ultra-thin porous films have done so primarily for adsorption studies; only a few researchers have combined physical nanostructuring of the surface with chemical functionality. For instance, Evans and colleagues [48] constructed porous ultra-thin multilayer substrates between 25 and 30 nm by ESA with charged poly(lysine) and silica nanoparticles. They measured acetone vapor absorption and obtained excellent signal to noise SPR data. They indicated that this technique could be applied to solutions that have weaker absorption spectra or solutions with low analyte concentration [48]. Furthermore, Wang *et al.* [49] constructed multilayer films by ESA with positively charged poly(styrene) (PS) latex particles and negatively charged gold carboxylates (Au-COO$^-$). The PS latex particles were removed by tetrahydrofuran (THF) extraction, forming a nanostructured porous surface. However, the pores on the surface had an average size of 2.2 μm; this surface was unsuitable for size selectivity of biomolecules. Figure 12 shows

the morphology of the films, illustrating the increased surface area that provided

sufficient space for catalytic activity applications [49].
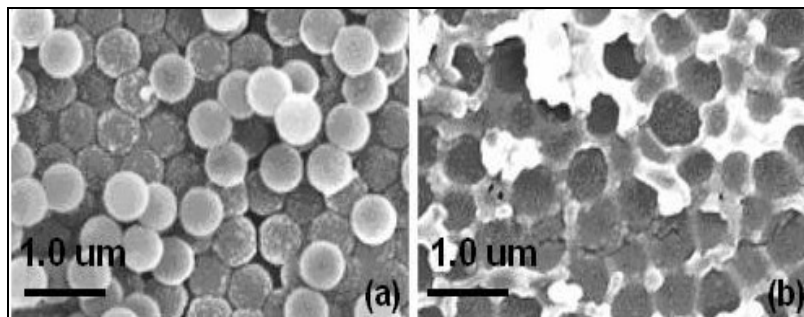
Figure 12. SEM images of polystyrene templates before (a) and after (b) THF extraction [49] (reprinted with permission from Springer).

As for the sensitivity of the porous surfaces, the work by Oh *et al*. [44] demonstrated an increase in sensitivity compared to nonporous surfaces. Oh and colleagues used an inorganic mesoporous silica (SBA-15) suspension treated with (3-mercaptopropyl) trimethoxysilane (MPTMS) to attach thiol groups. The authors attached the grafted mesoporous silica (MP-SBA) to a gold substrate using self-assembly of the gold-thiol interaction [44]. For comparison, another substrate was prepared using 1,6-hexanedithiol to generate a nonporous surface. The two substrates with distinct surface morphologies were used to detect Pt^{2+}. The angular shift on the nonporous substrate was only 0.25 degrees; meanwhile, there was an angular shift of 1.3 degrees on the porous surface (Figure 13). This experiment clearly shows the increase in sensitivity due to the porous surface. The pore size was 7.01 nm—suitable for size selectivity of small biomolecules.
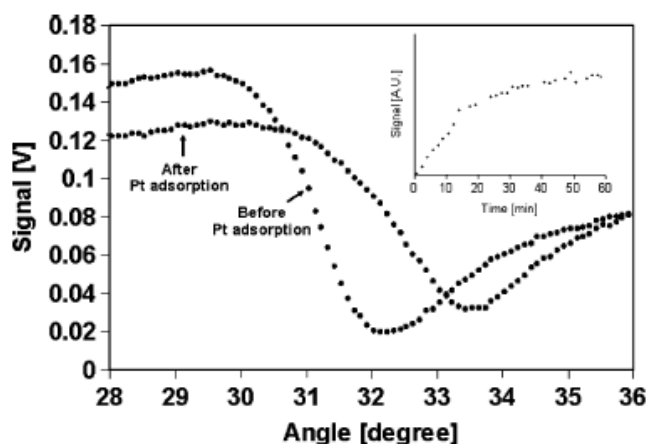
Figure 13. Before and after SPR angular shift during the detection of 10^{-3} M solution of Pt^{2+} using the MP-SBA porous surface. Nonporous surface angular shift was 0.25 degrees and porous was 1.3 degrees [44] (reprinted with permission from Springer).

2.1.3 Hyper-branched Polymeric Molecules and SPR

Studies on dendrimers, which historically have been better understood than star polymers, abounded in the late seventies. In the last decade, however, scientists began to use star polymers in their research more often. Both dendrimers and star polymers have three characteristic features (Figure 14). They both have a central core where polymeric arms branch off, interstitial regions where material can be occluded, and addressable periphery where functional groups can be attached [50, 51]. Multifunctional polymers such as star polymers or dendrimers can be exploited to add interesting features onto SPR substrates. For instance, star polymers can be used as templates for nanostructuring the substrate surface, and dendrimers can be used as monolayers on the SPR substrate to hold protein-ligand interactions [50, 51].
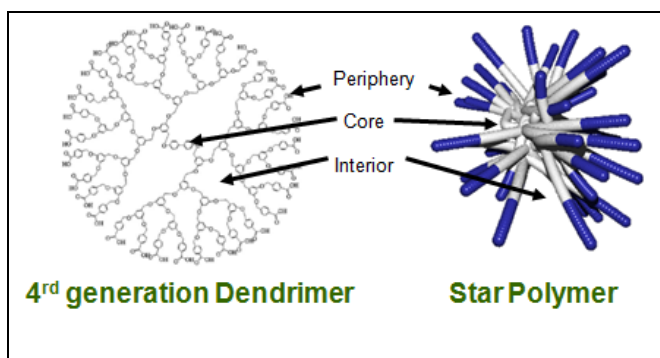
Figure 14. Topological features of dendrimers and star polymers: the core, the interstitial spaces, and the periphery [50] (reprinted with permission from Joseph Sly *et. al.*).

Hong and colleagues used monolayers of fourth-generation dendrimers on a SPR substrate to study the protein-ligand interaction of avidin and biotin [52]. The researchers attached an SAM of 11-mercaptoundecanoic acid (MUA) onto the gold substrate by chemisorption. After activation of MUA, a monolayer of poly(amidoamine) (PAMAM) dendrimer was layered and functionalized with sulfo-NHS-biotin. An angular shift of 0.34 degrees was obtained when PAMAM was layered on the substrate. When the authors measured the interaction of avidin in the biotinated PAMAM dendrimer, the shift was 0.50 degrees; the addition of biological material was successfully measured by SPR analysis [52]. Alternatively, only a few researchers have shown interest in the use of star polymers as templates for nanostructuring the substrates owing to the difficulties in star polymer synthesis [50]. Therefore, star polymers were evaluated as templates in this thesis project, providing critical data unavailable in existing literature.

2.1.4   Nonspecific Protein Adsorption & Nonfouling Surfaces

An inert SPR substrate surface is an important characteristic that must be implemented in biosensors to avoid nonspecific protein binding. This surface condition

prevents unwanted proteins from attaching to the sensor surface, which could potentially

distort the SPR measurements. A protein-repellent material attached on the surface of the

sensor is necessary for an inert surface. The most popular antifouling agent is

poly(ethylene glycol) (PEG) or one of its derivatives [53]. Selective adsorption of

proteins of interest and rejection of undesired proteins contained in biological samples is

required for effective SPR biosensing applications. Clare *et al.* [54] used monolayers of

short chain oligo(ethylene glycol) units (EGs) to study the effects of protein adsorption.

The authors analyzed protein binding with two different sizes of EG chains, one with

three EG units and the other with six units. In addition, they studied the effects of

polarity on protein adsorption by attaching hydrophobic alkyl groups or hydrophilic

hydroxyl groups to the end of EG chains. When the authors measured the fluorescence of

the adsorbed labeled proteins, nonspecific binding of unwanted proteins decreased by

70% when EGs were installed on the surface. The authors concluded that long chains

resist protein adsorption better than short chain EGs, and that hydroxyl-terminated chains

have a higher degree of protein repulsion than methyl-terminated chains [54].

Dalsin and colleagues presented another effective method for investigating

nonfouling properties on surfaces [55]. They mimicked the physical properties of an

adhesive mollusk protein and installed the synthesized analogs onto biomaterial surfaces.

The mussel adhesive proteins have the component 3-4-dihydroxypehenyl alanine

(DOPA), which promotes the anchoring of PEG molecules onto surfaces. Mussels use

this PEGylation mechanism to prevent the attachment of microorganisms. Based on

these observations, Dalsin *et al*. conjugated a PEG molecule to the DOPA residue to

generate PEGylated material of the form mPEG-DOPA. Since the adhesive protein DOPA is linked to a series of amino acids, the authors designed an amino-PEG-DOPA derivative of the form Ala-Lys-Pro-Ser-Tyr-DHP-Hyp-Thr-DOPA-Lys (mPEG-MAPD) [55]. They studied the antifouling properties of these two PEG derivatives, which were synthesized in two sizes, 2 kDa and 5 kDa. Nonfouling properties were measured using 3T3 fibroblast cells after the surfaces were modified with synthetic PEGylated analogs.

Figure 15(a) shows a fluorescence microscopy image of the cell growth after a gold surface was partially treated with mPEG-MAPD 5 kDa. After culturing the cells for 4 h, the cells in the untreated section of the gold substrate displayed healthy growth of fibroblasts, while the treated section showed dramatic nonfouling properties toward cell adhesion of approximately 98% effectiveness [55]. The first four sets of bars (left to right) in the graph in Figure 15(b) compare the controls that did not contain the adhesive protein or the two five kDa PEG analogs. The left black bar is the total projected area, and the gray bar is the density of cells. Greater cell adhesion was observed on the control surfaces that did not contain the PEG layer compared to the minimal cell adhesion on surfaces treated with either 5 kDa mPEG-MAPD or 5 kDa mPEG-DOPA (two set of bars to the right). This study successfully demonstrated that the antifouling properties of PEG were sufficient to prevent protein absorption on the substrate surface.
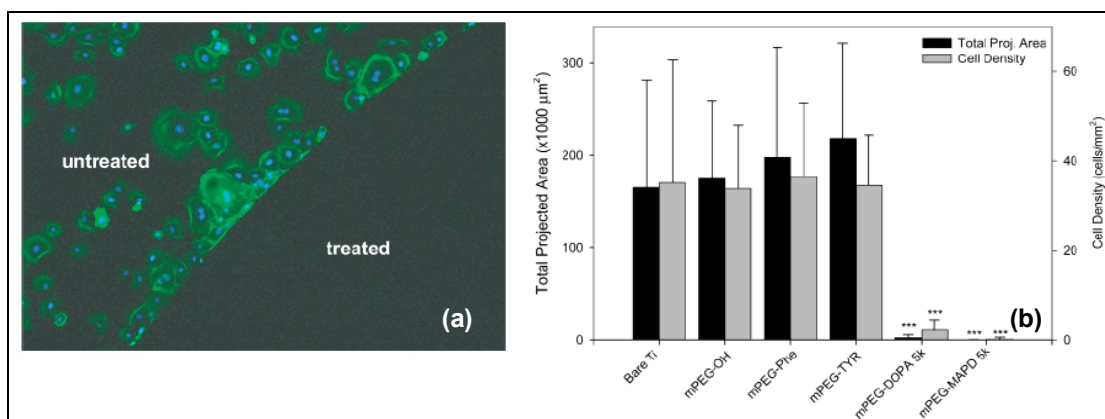
Figure 15. Fluorescent microscopy image of a gold substrate (a) partially treated with 5 kDa MPEG-MAP surface. Graphical analysis (b) on a titanium modified surface showing total projected area (black bars) and cell density (gray bars) *vs.* mPEG-DOPA and mPEG-MAPD [55] (reprinted with permission from American Chemistry Society).

2.1.5   SPR Biorecognition Elements

A well-layered SPR substrate with a nonfouling surface is necessary to investigate the properties of an engineered SPR biosensor. However, a pair of molecules is required to generate data, which indicates the overall sensor effectiveness. One of these molecules must be attached to the nonfouling surface, and the other must be flowing freely in the solution, exposing itself to its recognition pair. As discussed in Section 2.1.4, only the target molecule must bind to the sensor surface, and the nonfouling background must ensure that undesired proteins are not adsorbed onto the surface. The analyst must choose the proper pair of interacting molecules for these experiments. Some of the most common molecules for sensory studies are antibodies, which are expensive but provide excellent specificity and affinity. Alternatively, peptides are inexpensive, but lack high specificity and affinity. Other choices include organic molecules, such as avidin-biotin pairs, or aptamers, such as RNA or DNA about 20 nucleic bases long [1]. In SPR

sensory studies, peptides are widely used for the detection of antibodies against viruses

such as the herpes simplex virus or hepatitis G. Furthermore, protein-DNA pairs are used

as biorecognition elements because DNA has a specific molecular sequence and can

create physical conformational changes for specific proteins or nucleic acids [1, 55].

The biorecognition elements (BRE) must be ligated to the attached antifouling

polymeric chains, which contain three distinct chemical features: a hydrophobic organic

region that anchors to the substrate, a protein-resisting region for antifouling properties,

and a functional group for BRE attachment [15]. Figure 16 shows the components of the

polymeric chains on the substrate that are necessary to generate SPR substrates for

sensory studies. In this case, the BRE was insulin, which was attached to the gold

monolayer of heterobifunctional oligo(ethylene glycol)-dithiocarboxylic acid derivative

(OEG-DCA). The anti-insulin antibody Ins-mAb was the free flowing analyte [1, 56].
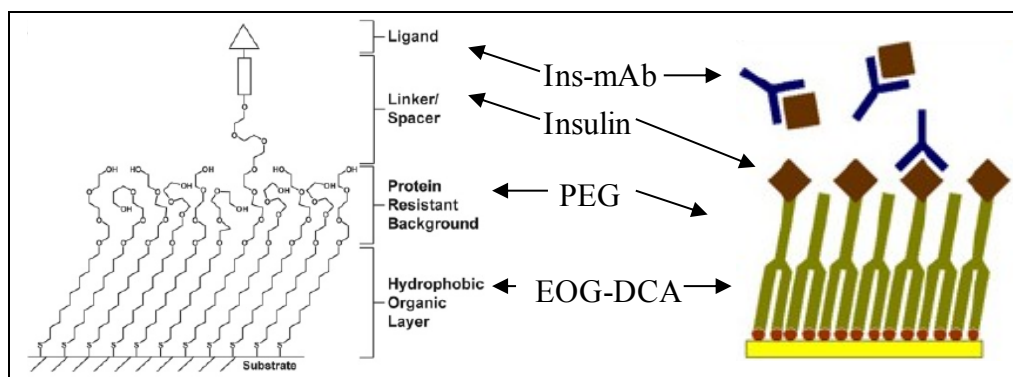
Figure 16. The four main components of the hydrophobic coating: the hydrophobic
layer, protein resistant PEG layer, the BRE or linker region, and the free flowing analyte
[1, 56] (reprinted with permission from Elsevier).

Taylor *et al.* [57] used molecules that contained antifouling properties and

biorecognition elements. They used monolayers of biotin derived poly(L-Lysine)-grafted

polyethylene glycol (PLL-g-PEG-biotin$_x$), where *x* represents the biotin content of 0, 1,

10, 20, 30, 40, and 50%. They also used radiolabeled streptavidin to study the

biorecognition capacity of the designed block copolymer. Two essential features of these

block copolymers are desirable: a biorecognition site where biotin binds, and an

antifouling region to prevent nonspecific absorption of proteins. The authors

demonstrated nonspecific adsorption on the substrate by only capturing streptavidin from

a mixture of proteins [57]. Figure 17(a) shows a graph of the binding events between

radiolabeled streptavidin and mouse monoclonal antibodies (mAb) at different

concentrations. Figure 17(b) provides schematic representations of the (PEGm)$_{(1-x)}$(PEG-

biotin)$_x$ as an individual polymer and as part of an integrated polymer network (c). As

shown in Figure 17(a), when the researchers exposed the bare TiO$_2$ surface to mouse

mAb, the calculated concentration was less than 0.5 pmol/cm^2.
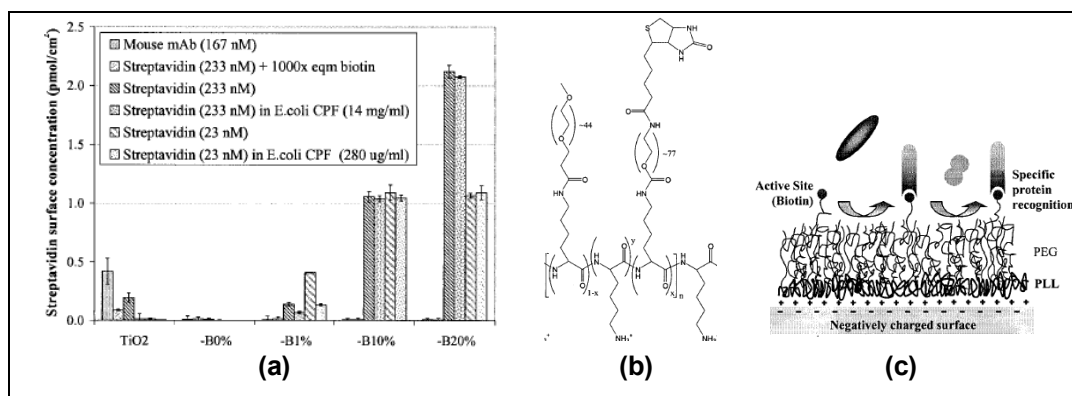
Figure 17. Histogram (a) showing the concentrations of streptavidin and mouse mAb against the bare TiO$_2$ and PLL-g-PEG-(biotin) modified monolayers. The chemical structure (c) shows the BRE biotin and the antifouling properties (d) of the layer [57] (reprinted with permission from PNAS).

However, when the surface was modified with PLL-g-PEG-(biotin) at various

biotin concentrations from 0 to 20% (x-axis), the mouse mAb was not detected. On the

contrary, more streptavidin was detected by increasing biotin content, as shown by the y-axis in Figure 17(a). This study confirms the antifouling properties of the PEG background, as well as the specificity of the biosensor to a target analyte [57].

2.2 Multifunctional Silica Nanoparticles

2.2.1 Review of Existing Core-Shell Silica Nanoparticle Procedures

Core-shell architectures have enabled researchers to generate nanoparticles with multiple functions. In order to synthesize core-shell composite nanoparticles, researchers must rely on templates such as quantum dots, colloidal gold seeds, organic polymers, or microemulsions [58, 59]. Kumar *et al.* [59] used organic microemulsions as templates to develop organically modified silica nanoparticles (ORMOSIL) and covalently attached fluoroprobes inside the SNPs. These silica nanoparticles were effectively surface functionalized with specific functional groups for further chemical reactions. The researchers synthesized the fluoroprobe precursor rhodamine B-silane (RS) by coupling the commercially available carboxyl-X-rhodamine N-succinimidyl ester with aminopropyltriethoxysilane (APTES). A microemulsion was prepared by mixing the surfactant Tween-80 with the cosurfactant 1-butanol in DMSO and water. The RS complex was added to the microemulsion, and the reaction was catalyzed by aqueous ammonia. Kumar and colleagues grew a silica coating around this complex by reacting either APTES or mercaptopropyltrimethoxysilane silica precursor. Although this process was difficult and time-consuming, it generated amino functionalized nanoparticles (Figure 18). These templated SNPs were monodispersed with an average diameter of 20 nm [59].
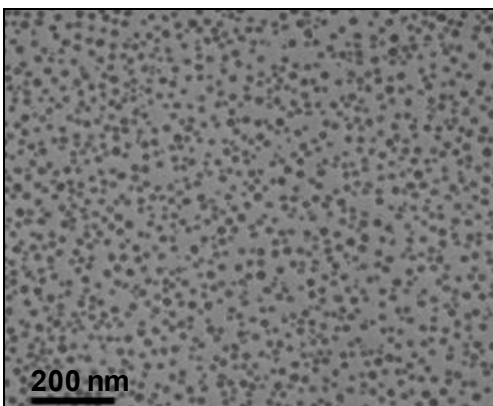
Figure 18. TEM image of the ORMOSIL coated with amino functional groups [59] (reprinted with permission from American Chemistry Society).

Graf *et al.* [58] developed an alternative way to coat different types of templates, such as colloidal silver and gold particles, or positive and negative charged polystyrene particles. Instead of using microemulsions, Graf *et al*. used amphiphilic nonionic polymers poly(vinylpyrrolidone) (PVP) as adsorbent seeds and used the Stöber method to grow silica shells around the templates. The templates used by Graf and colleagues did not contain silica nucleation sites, but the PVP polymers functioned as nucleation sites for silica to grow. The PVP polymers were attached to the gold particles and were isolated by centrifugation. The PVP-treated gold particles were resuspended in an ethanol solution of ammonia (4.2% v/v) and coated with silica using TEOS (10% v/v) [58]. Figure 19 shows gold templated silica nanoparticles measuring 15 nm in diameter that were treated with different molecular weights of PVP. The TEM micrographs in Figure 19 show the relationship between the molecular weights of the PVP and the degree of the aggregation of the gold templated silica nanoparticles. Selecting 10 kg/mol PVP (b) resulted in non-aggregated gold templated SNPs, as shown in Figure 19. In addition to coating gold with silica using the modified Stöber method [58], the size of the

SNPs was increased by adding more TEOS with the seeded method, in agreement with

Bogush *et al*. [22].
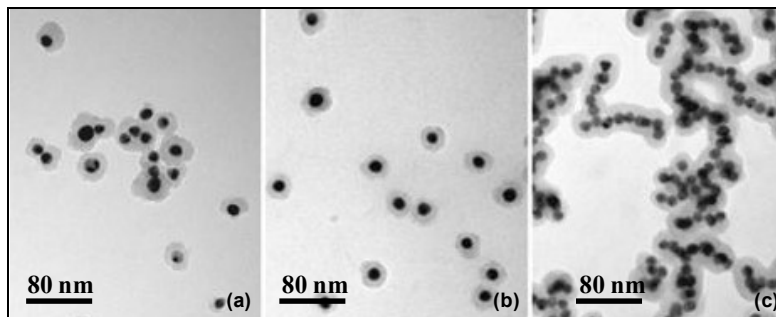
Figure 19. TEM micrographs of 15 nm gold seeds treated with PVP-40 kg/mol (a), PVP-10 kg/mol (b), and PVP-3.5 kg/mol (c). The degree of aggregation depended on the size of the PVP [58] (reprinted with permission from American Chemistry Society).

Quantum dots can be templates for silica encapsulation and can be coated with

specific tags for biolabeling purposes. However, as mentioned by Barkalova *et al*. [60],

quantum dots (QD) are only luminescent and photostable in nonpolar solvents. The QDs

need to be protected with a silica coating in compliance with biosystems [24]. Nann *et*

al. [61] used CdSe QDs that were passivated with a thin layer of zinc sulfide (ZnS) to

generate templated SNPs. However, these particles were further surface-modified to be

compatible with polar solvents and coated with silica using the Stöber synthesis. The

work by Nann *et al*. [61] and Graf *et al*. [58] demonstrated that inorganic templates can

be coated with silica after installation of organic nucleation sites.

2.2.2   Varying the Size of Silica Nanoparticles

Silica particles of different sizes can be generated by the seeded method, as

mentioned in Section 1.2.2. In this method, the silica precursor is added to preformed

SNPs to obtain larger SNPs. Liz-Marzan and colleagues [62] used this method to

increase the size of gold templated SNPs. The main parameters that dictated successful coating of the templates were the TEOS concentration and the pH of the reaction. Maintaining the pH between 8 and 10 reduced the solubility of the formed templated SNPs. This caused the polymerization of the silica precursor to occur at a rate adequate to coat the particles homogeneously, but sufficiently slow to prevent the formation of additional silica nuclei. Liz-Marzan and colleagues concluded that a ratio of 2:1 ethanol/water was needed to favor the nucleation of one gold seed per particle, hence eliminating secondary nucleation of silica. They recommended adding a small amount of TEOS to the pre-existing templated SNPs to increase their size. In this case, the hydrolyzed TEOS would preferably polymerize the pre-existing templated SNPs. As shown in Figure 20, using the seeded method, the shell thickness was subsequently grown on 15 nm gold particles from a 10 nm shell (a), to a 60 nm shell (b), and, finally, to an 80 nm shell (c) [62].
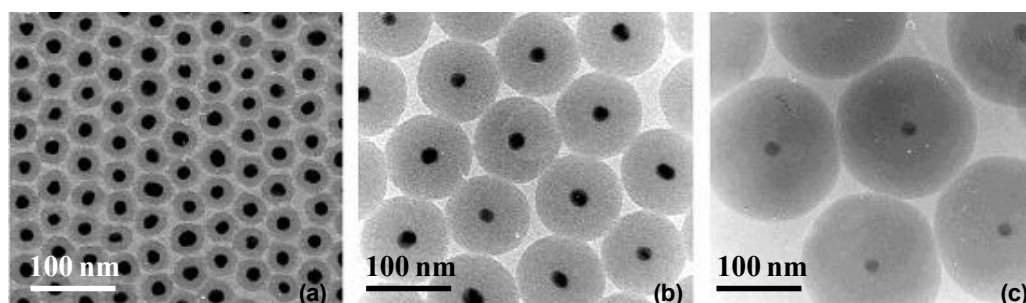
Figure 20. TEM micrographs of gold templated SNPs with different sizes obtained by the seeded method. Shell thicknesses are 10 nm (a), 60 nm (b), and 80 nm (c) [62] (reprinted with permission from American Chemistry Society).

Nakamura and co-workers [63] agreed with Liz-Marzan *et al.* [62] when both groups demonstrated the size increase of SNPs by the seeded method. However, Nakamura *et al.* [63] utilized the more reactive silica precursor, tetramethoxy silane

(TMOS), to generate templated SNPs. Their study indicated that the final sizes of the SNPs were achieved after 10 min. The diameter of the particles was increased by adding equimolar amounts of TMOS at 2-h intervals; the diameter increased from 0.61 µm to 0.80 µm, and finally to 1.21 µm [63].

Nozawa and co-workers [64] controlled the size of the templated SNPs by adjusting the addition rate of TEOS. This rate-controlled addition of TEOS prevented the generation of non-templated secondary nucleation of silica particles, an advantage over the seeded method. This process was modeled as a semi-batch reactor; TEOS was added at a constant rate to the reactor containing an ethanol solution of ammonia. This method gave the researchers greater control over particle size, shape, and distribution. When the addition rate of TEOS was increased, the size of the generated SNPs decreased. As shown in Figure 21, the addition rates 0.005 (a), 0.05 (b), and 0.5 mL/min (c) TEOS/EtOH generated particles 1820 nm, 1330 nm, and 635 nm in diameter [64].
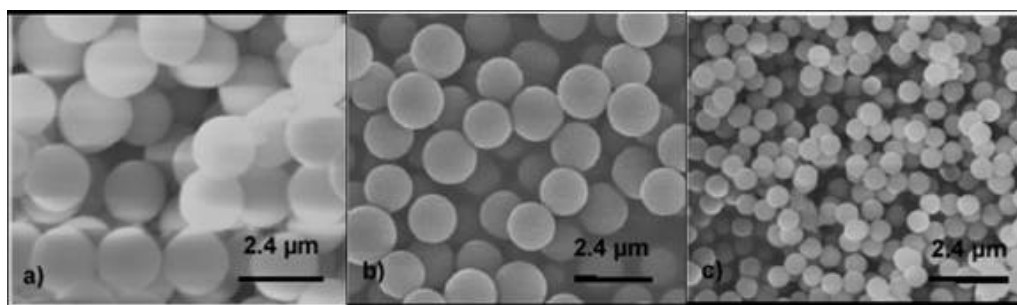
Figure 21. TEM images showing the effects of TEOS/EtOH addition on particle size using 0.005 mL/min (a), 0.05 mL/min (b), and 0.5 mL/min (c). The size of the silica particles was inversely proportional to the TEOS addition rate [64] (reprinted with permission from American Chemical Society).

Reduction of the concentration of the template is another method of generating larger SNPs; the SiO_2/template ratio allows more silica to be deposited per particle.

Nann *et al*. [61] investigated this relationship and noticed that when they decreased the concentration of the template, the silica shell thickness of the templated SNPs increased.

2.2.3   Surface Functionality

A common method of adding functionality to silica nanoparticles is by installing amino groups onto the surface, as demonstrated by Zhang *et al.* [65] and Wang *et al*. [66]. Amination is an ideal method to install functionality because amino groups react specifically and spontaneously with other functional groups. Installing amino groups on the surface of the particles, followed by conjugation of water-soluble molecules, increases biocompatibility. Silica nanoparticles themselves are biocompatible, but certain molecules such as PEG can enhance biocompatibility, stability, cell penetration, and water solubility [65]. Blaaderen *et al.* [67] studied the amino coating of silica nanoparticles in a one-pot procedure by adding the amino precursor APTES to the reaction mixture. Wang *et al*. [66] demonstrated in a simple experimental procedure that amination was achieved by simply reacting the preformed SNPs with APTES under agitation in a water bath at 50°C.

Lin *et al*. [68] and Bakalova *et al*. [60] agreed with Zhang *et al.* [65] concerning use of *N*-hydroxysuccimidyl ester (NHS) to conjugate the surface amino groups with PEG. NHS specifically reacts with primary amines at high rates. Zhang and colleagues used *N*-hydroxysuccinimidyl ester of methoxy PEG carboxylic acid (NHS-PEG) to PEGylate the amino-coated SNPs. The authors indicated that the aminated SNPs needed to be completely cleaned to remove traces of ammonia prior to PEGylation. This step was essential because ammonia deactivates the NHS-PEG material [60, 64-67].

36

Ammonia was removed by repeated centrifugation and resuspension of the aminated

particles in methanol buffer (0.1 mM NaHCO$_3$). Figure 22 shows a scheme of the

reaction between the aminated SNPs and the NHS-(PEG)$_m$; this reaction generated

surface functionalized particles, as shown in the TEM micrographs. The fuzzy

appearance surrounding the particles in the TEM micrograph (bottom right) indicated that

a PEG layer was installed as claimed by the authors [65]. Water solubility tests

confirmed that the PEGylated particles were stable in a 5% NaCl aqueous solution. The

use of NHS functionalized PEG material ensured the complete surface transformation of

amino-coated SNPs to generate biocompatible and water-soluble PEGylated silica

nanoparticles [65].
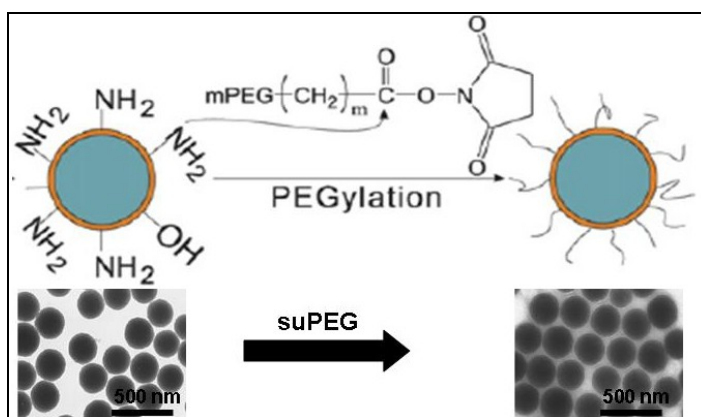
Figure 22. Reaction scheme of the PEGylation reaction on aminated SNPs with
N-hydroxysuccinimidyl-ester of methoxy PEG carboxylic acid. TEM micrographs
(bottom) of the functionalized SNPs show the fuzzy appearance surrounding the SNPs
and thus indicate the installation of PEG on the surface [65] (reprinted with permission
from Elsevier).

2.3   Summary

        This literature investigation described important parameters for adding specificity

and selectivity to SPR-based biosensors. When 50 nm of gold was deposited by physical

vapor deposition, uniform plasmonic responses were obtained. An additional thin layer of SiO_2 was applied on top of the gold layer. If the SiO_2 layer was less than 44 nm thick, the SPR signal was maintained. This layer allowed porous surfaces to develop by using templates such as star polymers. This nanostructured layer also provided greater sensitivity and selectivity in comparison to planar surfaces. AFM and TEM were excellent techniques to characterize these nanostructured surfaces. Installation of an antifouling surface integrated with biorecognition elements resulted in a specific surface chemistry necessary for efficient SPR biosensors.

This review provided information on the experimental conditions necessary to generate templated SNPs using a modified Stöber process. Size variation of the templated SNPs was achieved by using the seeded method or by varying the addition rates of the silica precursor. Using the organosilane APTES as the amino precursor allowed activation of particles by installing amino groups on the surface of the SNPs. NHS-PEG specifically reacted with surface primary amino groups, generating PEGylated SNPs. PEGylation of the SNPs enhanced biocompatibility, cell penetration, and stability of the particles in biological media.

CHAPTER THREE
HYPOTHESIS AND OBJECTIVES

3.1   Hypothesis

The hypothesis for the 2D sensors was that increased selectivity and sensitivity of SPR-based biosensors would result from functionalizing the porous surfaces. To test this hypothesis, an organosilicate solution mixed with star polymers was spin cast on SPR substrates. The porosity was obtained after curing the SPR substrates at high temperatures. Porosity can be random if star polymers are used or ordered if block copolymers are used. Installation of an antifouling PEG background on the porous substrates prevents nonspecific binding of unwanted proteins that could potentially distort SPR data.

For 3D silica nanoparticles, the hypothesis was that star polymers would be suitable templates for silica deposition. To test this hypothesis, star polymers were engineered to have a hydrophilic shell and a hydrophobic core. The shell was composed of poly-amine arms that functioned as sites for silica deposition and provided water solubility. The hydrophobic core accommodated hydrophobic material inside; the Stöber process encapsulated these complexes with silica. To confirm this hypothesis, scanning electron microscopy (SEM) and TEM were used to image the SNPs. The star polymer templated SNPs were further surface functionalized with PEG for biocompatibility.

3.2   Objectives

The main objectives for the 2D biosensor were to produce multiple SPR substrates by PVD; to nanostructure the surface of the SPR substrates with different

porosity; and to install an antifouling background. The surface at each different step was characterized by AFM, TEM, SPR, and SEM. The functionalized biosensors were characterized using contact angle measurements, and the antifouling properties of the transformed surface were tested using bovine serum albumin.

The main objectives for the 3D silica nanoparticles were to occlude hydrophobic dyes inside the star polymers; to coat the dye-occluded star polymer with silica; to control the size and the cargo release; and to functionalize the surface of the SNPs with biocompatible material. The dye-occluded particles were characterized by UV-vis and fluorescence spectroscopy, and the morphology of the templated SNPs was characterized by TEM, AFM, and SEM. The water-soluble particles were measured using dynamic light scattering (DLS).

3.3   Justification

A porous surface on the SPR biosensor increases the surface area. This physical parameter can increase the probability of chemical reaction between the receptor molecules installed on the porous surface and the target analyte. These physical features, in combination with chemoselectivity, can increase the sensitivity and selectivity of the SPR biosensor. Disease markers in the blood could then be detected at the earliest stages of illness, allowing early diagnosis and treatment. Oh *et al*. [44] used porous surfaces and noticed an increase in sensitivity by an order of five compared to nonporous surfaces. Most researchers have not explored the use of "ultra-thin" porous films as biosensors because of the difficulty of maintaining the thickness of the layers within SPR evanescent electromagnetic wave limits. Most uses of ultra-thin films involve absorption studies;

few researchers have incorporated receptors and physical features to explore ultra-thin porous films as a means of detecting biomolecules. Alternative tools for biosensing are silica nanoparticles, which are used as internal cellular probes.

Multifunctional water-soluble silica nanoparticles that can incorporate dyes, drugs, or other biomarkers within the particles are very useful for biomedical applications. Larson *et al.* [69] used core-shell SNPs that had been synthetically adapted to the dye TRITC so that the dye could be incorporated within the silica particles. The star polymer, which was used in this thesis project, has a hydrophobic pocket and hydrophilic polyamine shell. The installation of silica nucleation sites on the periphery of the star polymers (polyamine shell) makes the use of toxic surfactants and nucleation site enhancers unnecessary. The engineered hydrophobic core is a "universal carrier," allowing any dye or drug to be incorporated within a star polymer's hydrophobic pocket *via* molecular self-assembly. This method avoids the use of complex dye-polymer adaptations. Therefore, the encapsulation of silica and the inclusion of any drug or dye can be facilitated with only one type of star polymer. This is very important in the medical field, where alternative versatile methods for drug delivery or cell imaging are always in demand. The star polymer approach meets these demands.

CHAPTER FOUR
MATERIALS AND METHODS

A typical SPR setup utilizes a high refractive index prism, a flow cell, a thin film of gold fused to a glass (with the same refractive index as the prism), a light source, and a light detector. The SPR biosensor or substrate is the thin film of gold fused to the glass. The reflected light passes through a set of optical devices to the detector, which sends the collected data to a PC. Figure 23 shows the construction of the SPR biosensor employed in this study. It consists of a SF-11 glass, a thin adhesion layer of chromium (Cr), a 50 nm gold layer, a thin film of SiO_2, and an organosilicate layer.
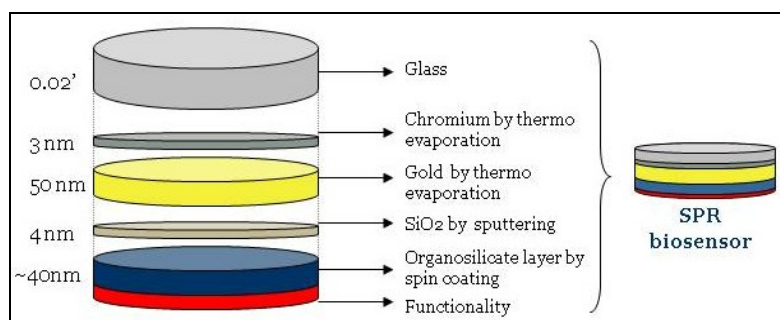
Figure 23. Detailed construction of the SPR biosensor. A thin layer of chromium is deposited by vapor deposition, followed by 50 nm of gold and four nm of SiO_2. A thin 40 nm organosilicate layer is deposited by spin coating.

The optimum thickness of the gold (Au) layer used in this study was 50 nm; this value is in agreement with Szuneritz et al. and Manera et al. [42, 43]. The uniformity of the gold deposition was analyzed by SPR, and resonance angles originating between substrates from the same batch were compared. Star polymers or block copolymers were dissolved in an organosilicate solution, spin coated onto the substrates, and cured at high temperatures to obtain the porous surfaces. The thickness of the organosilicate layer was determined by ellipsometry, TEM, and SEM. AFM was used to characterize the

morphology of the substrates, and SPR or contact angle measurements were used to

monitor the physical and chemical changes. Surface functionality was achieved with

3-aminopropyltrimethoxy silane (APTMS) followed by PEGylation. Antifouling

properties of the PEGylated surface were tested using a solution of bovine serum albumin

(BSA). Table 1 summarizes the physical experiments employed in the construction of

the biosensor, and the table includes all the surface transformations.

Table 1. Experimental matrix for the construction, analysis, and characterization of the
SPR biosensor.

Surface	Type of experiment	No. of Runs	Experimental goals
Glass	● Physical vapor deposition of Au and Cr	3	● To deposit the metal thin film
Gold	● SiO_2 sputtering	3	● To provide gold stability against high temperature
SiO_2	● SPR on SiO_2	3	● To acquire the SPR baseline
Organosilicate	● SPR on dense surface with/without PEG	3	● To investigate the PEGylation reaction
Organosilicate	● SPR on porous surface with/without PEG	3	● To investigate the PEGylation reaction
Organosilicate	● SPR on ordered porous surface with/without PEG	3	● To investigate the PEGylation reaction

The template employed to generate the 3D silica nanoparticles was synthesized

and engineered with a hydrophobic core made of polystyrene and a hydrophilic shell

made of poly (*N,N*-dimethylaminoethylmethacrylate). An occlusion complex was

formed using the star polymer and a hydrophobic dye by molecular self-assembly

(explained further below). This complex was used as a template for silica formation.

The first method involved the synthesis of the templated silica nanoparticles using the

standard two-step Stöber procedure known as the "two-pot" method. This method was

simplified, and the overall procedure was reduced to a single step or "one-pot" synthesis. Once the particles were synthesized, different organosilicate agents were used to transform the surface of the nanoparticles. According to Iler *et al.* [17], the silanol groups on the surface of the nanoparticles are very reactive. Therefore, in this thesis project the particles were coupled with a passivating agent to prevent cross-linking and aggregation. The surface of the particles was transformed into an aminated surface for further chemical reactions. In some cases, the surface amino groups were coupled with a dye to test for reactivity; in other cases, the amino groups were coupled with PEG to generate water-soluble nanoparticles. Furthermore, the size of the particles was varied by changing the reaction time, concentration of the silica precursor, and size of template. Table 2 shows the steps for the production of star polymer templated SNPs and the surface transformations.

Table 2. Experimental matrix to generate water-soluble templated silica nanoparticles.

Particle surface	Type of experiment	No. of Runs	Experimental goals
Star polymer	● Encapsulation with silica	3	● To make templated silica nanoparticles
Silanol	● Passivation with diphenyl-dimethoxysylane ● Passivation with hexamethyldisilazane	3	● To passivate the silanol silica nanoparticles
Silanol	● Activation with 3-amino propyldimethylethoxysilane ● Activation with 3-amino propyltrimethoxysilane	3	● To activate the silanol silica nanoparticles
Aminated surface	● PEGylation and dansylation of the surface	3	● To add water solubility
Silanol	● Investigation of reaction time, size of template, and silica precursor	3	● To vary the size of the silica nanoparticles

4.1.1   Materials: SPR Biosensors

Since the prism used in the SPR studies was made of SF-11 glass material, the substrates used were also made of SF-11 to maintain the refractive index of the light path. The SF11 substrates, commercially available from Stefan Sydor Optics (Rochester, NY), were 1.0 inch in diameter and 0.02 inch thick with surface roughness less than 10 Å. Some of the initial studies were performed on one-inch diameter, 0.020-inch thick, single-sided polished silicon wafers doped with phosphorus from Virginia Semiconductor (Fredericksburg, VA). The SF11 wafers were made of a dense silicate glass of less than 47% lead oxide, with a refraction index (n) of 1.778 at a wavelength of 635 nm at 25 ^{0}C [70]. An adhesion layer of chromium 3.0 nm thick was applied to the SF11 glass wafers, sandwiched between the glass substrate and 50 nm gold films by PVD using in-house procedures. A layer of silicon dioxide (SiO_2) was applied on top of the gold either by sputtering using an AJA SiO_2 tool or by physical vapor deposition using an in-house evaporator. Methyl silsesquioxane (MSSQ) in LKD-2015 was purchased from Japan Synthetic Rubber (Sunnyvale, CA), and propylene glycol monomethyl ether acetate (PM-acetate) and propylene glycol n-propyl ether (PGPE) were purchased from Sigma-Aldrich (St. Louis, MO). The porogen star polymer had a 600 kDa core made of individual 15 kDa polystyrene arms; coupled to these arms were additional 5 kDa PEG arms (SP-PS-*b*-PEO) [71]. This polymer was used to nanostructure the SPR substrates with random porosity. A polystyrene-polyethylene oxide block copolymer (PS-*b*-PEO) synthesized in-house by Victor Lee at IBM (San Jose, CA) was used to nanostructure the SPR substrates with ordered porosity. Figure 24 shows the two types of polymers used to

nanostructure the surface of the SPR biosensors. For the antifouling studies, the PEG

polymer N-hydroxysuccinimidyl (polyethylene glycol)$_7$-OMe (NHS-(PEG)$_7$-OMe)

purchased from IRIS Biotech GmbH (Marktredwitz. MR, Germany) was used to

PEGylate the surface of the SPR substrates.
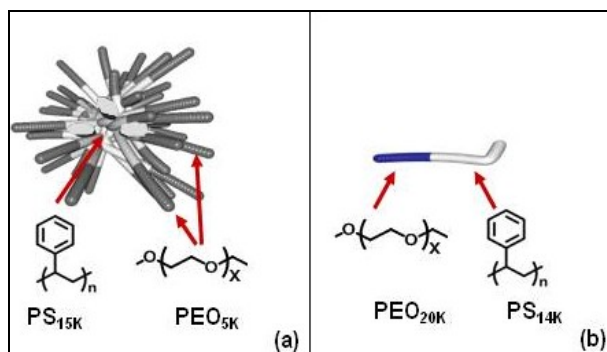
Figure 24. Star polymer (a) containing a polystyrene core and a polyethylene oxide shell
used to nanostructure the SPR substrates with random porosity, and the block copolymer
(b) made of polystyrene and polyethylene oxide blocks used to nanostructure the SPR
substrates with ordered porosity.

4.1.2 Materials: Templated Silica Nanoparticles

Ethanol (200 proof) was purchased from Gold Shield Chemical Company

(Hayward, CA), and 30% ammonium hydroxide was purchased from J.T. Baker

(Phillipsburg, NJ). TEOS, TMOS, 3-aminopropyl-trimethoxy silane (APTMS), 3-

aminoproplyldimethylethoxysilane (APDMES), hexamethyldisilazane (HMDS), dansyl

chloride, and tetrahydrofuran (THF) were purchased from Sigma-Aldrich (St. Louis,

MO); diphenyldimethyxysilane (DPDMS) was purchased from Gelest (Morrisville, PA).

All chemicals were used as received without any further purification. Older reagents of

TEOS, TMOS, and APTMS were purified by distillation to remove hydrolyzed

polymeric and monomeric chemical species. The different PEG polymers

N-hydroxysuccinimidyl-(polyethyleneglycol)-methoxy terminated (NHS-(PEG)$_n$-OMe)

with sizes 750 Da, 2 kDa, 5 kDa, and 10 kDa were purchased from IRIS biotech GmbH (Marktredwitz. MR, Germany). Regenerated cellulose dialysis membranes of molecular weight cutoff (MWCO) 3.5-25 kDa were purchased from Spectrum Labs (Greensboro, NC). The synthesis of the star polymer poly(*N,N*-dimethylaminoethylmethacrylate) (SP-PS-b-DMAEMA) was previously reported [72, 73]. This specific star polymer was engineered to have a polystyrene core, which generated a hydrophobic pocket accessible to hydrophobic cargo occluded by molecular self-assembly. This polymer was also engineered to have a poly amino shell, which had two important functions. First, the hydrophilic shell provided water solubility, which permitted the occlusion of hydrophobic dyes into the core. Second, the amino groups contained in the shell were excellent nucleation sites for silica deposition. The synthesis of the solvatochromic dye 5,10,15,20-(3,5-ditertbutylphenyl)porphyrin was conducted by Joseph Sly at IBM Almaden Research Center (San Jose, CA) according to literature procedures [74]. Figure 25 illustrates the PS-*b*-DMAEMA/Porphyrin occlusion complex depicting the chemical composition of the star polymer and the occluded porphyrin dye.
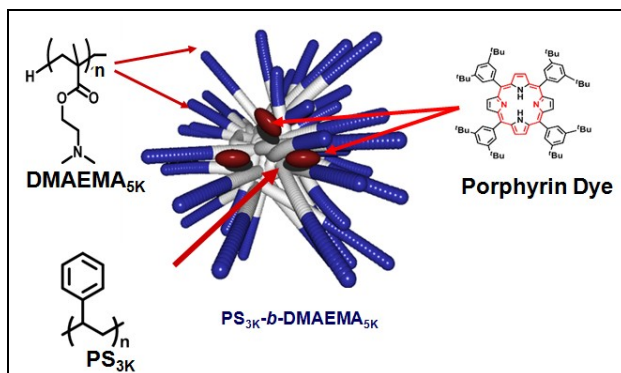
Figure 25. Porphyrin occluded star polymer used for silica encapsulation. Polystyrene hydrophobic core and polyamine hydrophilic shell permitted the encapsulation of hydrophobic dyes and provided water solubility to this occlusion complex [72-74].

4.2   Methods

4.2.1   SPR Gold Substrates Preparation

The thermo evaporator, which was assembled at IBM Almaden Research Center, was carefully vacuumed to remove metal fragments from previous experiments. The internal components of the evaporator were cleaned with isopropanol soaked Kim wipes to remove small particulates. The SF-11 glass wafers were cleaned by flowing nitrogen gas to remove dust from the surface. In both instances, cleaning removed particulates that could potentially interfere with metal deposition. The automatic shutter was used to obtain a desired film thickness and to ensure reproducibility. A 3 nm adhesion layer of chromium, followed by 50 nm of gold and 4 nm of SiO_2, were deposited sequentially. The chromium adhesion layer was necessary to ensure a compact binding of the gold to the SF11 glass wafer. After gold deposition, the freshly-prepared substrates were sputtered with 4 nm of SiO_2 using an AJA sputtering tool. Alternatively, physical vapor deposition (PVD) was adequate to deposit the SiO_2 layer, which functioned as a protective film against heat exposure during the curing process.

4.2.2   Nanostructuring Thin Silicate Films on SPR Substrates

The SPR substrates were exposed to UV-ozonolysis for 5 min in a Senlights photo processor. This was performed to obtain a clean surface and to expose silanol groups before spin coating the organosilicate layer onto the SPR substrates. "Dense," *i.e.* nonporous thin films, were prepared by spin coating a solution of the organosilicate precursor MSSQ in LKD-2015 with propylene PM-acetate. The LKD-2015 organosilicate solution contained 21.5% of MSSQ; PM-acetate was used to dilute the

original solution to a final concentration of 2.5% MSSQ weight/weight (w/w). The organosilicate solution was applied onto the SPR substrates by spin coating, and the substrates were thermally cured to obtain featureless dense films.

To construct the random porosity silicate films, porogen (SP-PS-*b*-PEO) was dissolved in PM-acetate to obtain a 2.5% w/w porogen solution. This solution was gently heated and sonicated for 30 min; this process ensured complete mixing of the contents. Then, 0.4 parts of the 2.5% porogen solution were mixed with 0.6 parts of a 2.5% MSSQ solution. This specific porogen/MSSQ ratio is known as the "40% porous" film ratio. This final mixture was well mixed and spun onto the SPR substrates through filtration, and the substrates were thermally cured to generate random porosity.

To generate the substrates with ordered porosity, 0.3 parts of 1% PS-*b*-PEO block copolymer in PM-acetate were dissolved in 0.7 parts of 1% MSSQ in PGPE. This organosilicate mixture was placed on a shaker for 1 h and heated up to 100 °C until the solution became clear. The solution was applied onto the SPR substrate by spin coating; the substrates were then thermally cured to generate ordered porosity.

4.2.3 Spin Coating and Curing the Silicate SPR Substrates

After the 40% porogen organosilicate solution was prepared, the SPR substrates were cleaned with nitrogen gas to remove dust particles. A 2.0 μm Teflon filter was attached to a 1.0 mL syringe, and 4-5 drops of the 40% solution were placed onto the substrate; the solution covered the whole surface, and there were no air bubbles. The substrates were placed on a Headway Research thin film spin coater that was set to 3000 RPM for 30 s. Then, the substrates were placed in a VWR 355 programmable hot plate

under nitrogen. The program started at 50 ºC and the temperature increased 5 ºC per minute until it reached 450 ºC. The substrates were maintained at this temperature for 1 h to completely cross-link the organosilicate layer. Curing the substrates at this high temperature burned out the star polymer on the 40% organosilicate solution and generated randomly distributed porosity, while the dense organosilicate solution generated a featureless surface.

In the case of the ordered porosity SPR substrates, the 7:3 ratio block copolymer/ organosilicate solution was heated to fully dissolve the solution prior to spin coating. The SPR substrates were UV-ozone treated for 5 min to expose a clean surface, and nitrogen gas was blown directly onto the surface of the SPR substrates to remove dust. The cleaned substrates were placed on a Cost Effective Equipment spin-coater. A 1.0 mL syringe with a 2.0 μm Teflon filter was assembled, and 5-6 drops of the block copolymer containing silicate solution were placed onto the substrate. Under a chloroform-vapor atmosphere, the substrates were spin-coated at 500 rpm for 3 s and 1000 rpm for 90 s. After that, the SPR substrates were cured on a programmable hot plate that increased the temperature from 50 ºC to 450 ºC at 5 ºC/min; the substrates were maintained at 450 ºC for 2 h to generate the ordered porosity. Figure 26 is a schematic representation of the nanostructured films obtained after curing the three different organosilicate solutions at 450 ºC. Figure 26 shows the dense featureless film (a) obtained from the organosilicate solution alone, the random pores (b) from the porogen mixed with organosilicate solution, and the block copolymer (c) mixed with the organosilicate solution.
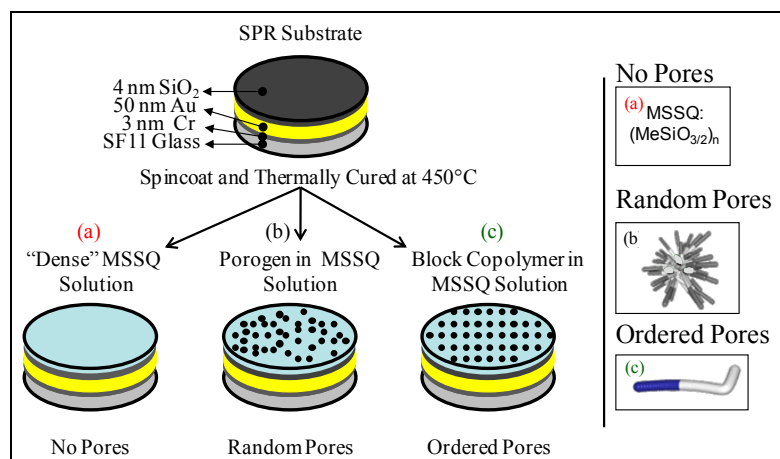
Figure 26. Nanostructuring the SPR substrates to generate three surface morphologies: dense featureless surface (a) from organosilicate alone, random porosity (b) from porogens, and ordered porosity from block copolymers (c).

4.2.4 Organosilicate Layer Thickness Measurements

A Gaertner ellipsometer was used to measure the thickness of the organosilicate layers. To determine the height of the thin layers, ellipsometer data were fitted to a model requiring two unknowns: the refractive index and the thickness of the film. Therefore, the refractive index of the organosilicate layer was obtained with a Filmetrics F20 thin film analyzer; these values were used to obtain the thicknesses of the films using the ellipsometer. Since the organosilicate layer of the ordered porosity substrate was too thin to obtain refractive index measurements by filmetrics, the thickness of this layer was determined using transmission electron microscopy.

4.2.5 Surface Functionalization of the SPR Substrates

Substrates were UV-ozoned for 15 min in a Sen-Lights photo surface processor before submitting the samples for APTMS vapor deposition or solution-based deposition. Contact angle measurements were obtained before and after surface transformations with

51

a Dataphysics instrument analyzer. APTMS vapor deposition was performed using in-house synthetic procedures. Solution-based APTMS deposition was performed by immersing the SPR substrates in 0.175 mL of distilled APTMS and 4.0 mL methanol for 3 h while stirring gently. The substrates were washed with distilled water and air dried with nitrogen gas. PEGylation of the substrates was performed by immersing the substrates in 100 mg of NHS-(PEG)$_7$-OMe in 5.0 mL dichloromethane with 0.5 mL triethylamine (TEA) for 24 h while stirring. Substrates were washed and dried with ethanol and nitrogen.

4.2.6   Protein Bovine Serum Albumin Preparation

The protein bovine serum albumin (PBS) was dissolved in a phosphate buffer saline (PBS) solution. PBS was prepared by dissolving 107 mg of disodium phosphate (Na$_2$HPO$_4$) and 13 mg of monosodium phosphate (NaH$_2$PO$_4$) in 50 mL of millipore water. A solution of BSA in PBS was prepared by dissolving 1.5 mg of BSA in 1.5 mL of PBS and then mixed for 24 h at room temperature on a Labquake shaker from Labindustries, Inc. (Arlington, TX).

4.2.7   Star Polymer Occlusion Complex as Template for Silica Deposition

The star polymer PS-b-DMAEMA was used as a template to prepare a dye-occluded star polymer colloidal solution. The hydrophobic polystyrene core produced a hydrophobic pocket to occlude hydrophobic material, and the polyamino periphery provided water solubility. A solution of 10 mg of the star polymer in 0.4 mL of THF was prepared. To ensure that the star polymer was fully dissolved, the solution

was gently heated with a heat gun and sonicated for 10 min. After that, this solution was added into a separate 4 mL vial containing 2-3 mg of porphyrin dye; this mixture was sonicated for another 10 min to ensure the dye and the star polymer were fully dissolved in THF. Then, 5.0 mL of 200-proof ethanol was poured into a separate 20 mL vial. While the solution was vigorously stirred, the star polymer/dye mixture was added drop by drop. After a few minutes, the transparent solution became opaque due to the precipitation of the excess dye. This hazy solution was passed through a 0.45 μm Teflon filter to remove the large dye aggregates. The filtrate contained the dye-occluded star polymer, which was purple in color and transparent in appearance. The dye and the star polymer were both soluble in THF (nonpolar solvent). When they were poured into ethanol (polar solvent) through molecular self-assembly, the solvaphobic forces drove hydrophobic material into the core, generating the occlusion complex. Figure 27 shows a schematic representation of the occlusion complex obtained *via* self-assembly.
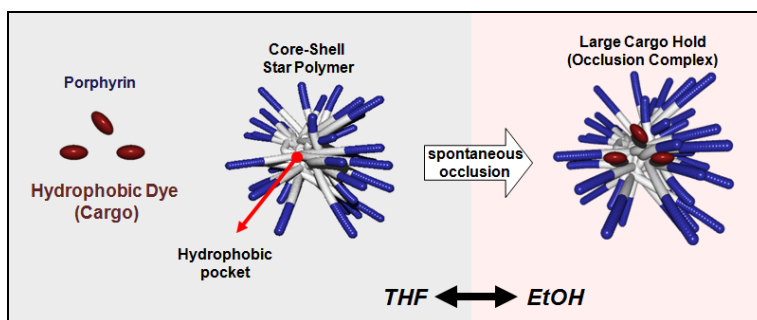
Figure 27. Dye-star polymer "occlusion complex" formed by molecular self-assembly when the hydrophobic dye and star polymer were exposed to water or ethanol.

4.2.8   Templated Silica Nanoparticles: "Two-Pot" and "One-Pot" Methods

Templated silica nanoparticles were generated using the modified Stöber method by means of two different experimental procedures. In the "two-pot" method, the

template silica nanoparticles were generated using two distinct steps; the other method was the "one-pot" method in which the particles were generated and functionalized in one general step. An occlusion complex was prepared by dissolving 25 mg of the star polymer and 4 mg of porphyrin dye in 0.20 mL THF. The mixture was added drop wise to 3.75 mL 200-proof ethanol with agitation and stirred for 10 min. In a separate vial, 0.85 mL of 30% w/v NH_3OH was added to 16 mL 200-proof ethanol while stirring. A 2.0 mL aliquot of the occlusion complex was added to this basic ethanol solution and was aged for 20 min. Then, 150 μL of TEOS was added sequentially during three 10-min intervals, adding 50 μL of TEOS each time. This reaction continued for 2 h at room temperature until the Stöber solution was poured into 300 mL of toluene. The solvent volume was reduced under vacuum at 60 °C in a Büchi Rotavapor R-200. This step was repeated two more times to ensure that ethanol, water, and ammonium hydroxide were completely removed from the solution. Caution is advised when removing the solvent in this step because at low pressure and high temperature, gases can be released from the solution, causing sudden bursts. Boiling of the solvent indicates an impending burst. To prevent this, the exhaust valve must be opened to control the pressure and release the liberated gases.

The final volume was approximately 10 ml; the solution was transferred to a 20 ml vial, and the silica nanoparticles were passivated by adding 1.5 ml of HMDS. The reaction was stirred for 16 h at room temperature. The generated functionalized SNPs were characterized by transmission electron microscopy.

To synthesize the star polymer templated silica nanoparticles using the Stöber procedure in a "one-pot" method, 5 mL of the occlusion complex was prepared as mentioned in Section 4.2.7. The occlusion complex was poured into 12.5 mL of 200-proof ethanol containing 0.85 mL of 30% w/v ammonia while the mixture was stirred at room temperature. The reaction was aged for 20 min, and 8 µL of TMOS were added each time in three sequential 7-min time intervals. The reaction vessel was stirred at room temperature, and after 3 h, the silica nanoparticles were passivated by adding 24 µL of diphenyldimethoxysilane (DPDMS). The passivated star polymer- templated silica nanoparticles were stirred at room temperature for 16 h; the particles were characterized by scanning or transmission electron microscopy.

4.2.9   Particle Surface Functionalization

The "one-pot" method, which comparatively reduced sample handling and solvent wastes, was used to generate particles for surface functionalization. The star polymer-templated dye-occluded silica nanoparticles generated in the "one-pot" method were either passivated with DPDMS or activated with APTMS. The nanoparticles were activated by adding 8 µL of APTMS each time in three sequential 7-min time intervals. Further modifications were added by coupling specific dyes or polymers to the amino groups depending on the specific experiment being performed. For instance, to test the reactivity of the amino groups on the surface, the particles were dialyzed against methanol to remove excess APTMS. The solvent was changed to toluene, and the amine reactivity was tested by adding 100 mg of dansyl chloride and 0.3 mL triethyl amine (TEA). After 16 h, the reaction was dialyzed against methanol to remove excess dansyl

chloride, and the reactivity of the amino groups on the surface was characterized by UV-vis spectroscopy.

The surface amino groups were coupled with different-sized PEG molecules to add water solubility. The amino-activated silica nanoparticles were dialyzed overnight against dichloromethane (DCM) to remove excess APTMS. The particles were removed from the dialysis bag, and the volume of the particles was adjusted to 10 mL with DCM. To drive the reaction, 0.3 mL of TEA were added; while the mixture was stirred, 100 mg of NHS-(PEG)$_n$-OMe (750 Da, 2 kDa, 5 kDa or 10 kDa) were added, and heat was applied to completely dissolve the PEG material. The PEGylated particles were dialyzed against methanol to remove DCM and dialyzed against water to study water solubility. The particles were characterized by dynamic light scattering (DLS) and imaged by either SEM or TEM.

4.3   Instrumentation

4.3.1   Surface Plasmon Resonance

SPR measurements were obtained to analyze physical and chemical changes in the substrate that resulted from layer addition or from chemical functionalization of the surface. The two modes of SPR analysis utilized in this study were the kinetic mode and the angular scan mode. The kinetic mode measures light intensity *vs.* time and is used to see how fast a surface change has occurred, whereas the angular scan mode measures the light intensity *vs.* SPR angular shift and is used to determine angular shifts due to any surface deposition. These two operating modes were employed in SPR analysis to indicate that layers of material had been added on the surface or chemical modification

had occurred. Analyses of the substrates were performed with a variable angle SPR apparatus from IBM Almaden Research Center that contained a laser diode with an 854 nm wavelength. This variable angle SPR setup had two arms that were located radially to the prism and moved in a synchronized manner at a resolution of 0.001 degrees with a scan range of 15 to 90 degrees. As seen in Figure 28, the light source was mounted on one arm and the light detector was mounted on the other arm. The reflected light from the SPR substrates was collected by the light detector and transferred to the computer, providing a graphical curve of the light intensity *vs.* angle [70].
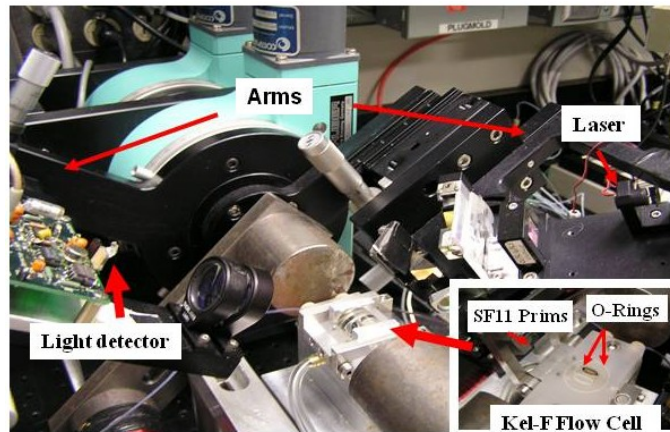
Figure 28. SPR apparatus displaying the main optical components: arms, laser, light detector, SF-11 prims, and Kel-F flow cell.

The SPR substrate was placed with the metal coating side face down onto a designed Kel-F flow cell, which contained a pair of elliptical Perlast® o-rings made of a highly resistant perfluoroelastomer material; the o-rings enclosed inlet and outlet flow cell ports. Outside these smaller o-rings, a larger circular o-ring made of the same material enclosed the vacuum port used to hold the substrate in place by suctioning the substrate against the o-rings (Figure 28). Once the substrate was placed onto the Kel-F

flow cell under vacuum, 2-3 drops of RIMF (Cargille Labs, Cedar Grove, NJ) of the same

refractive index (1.7650) as the SF11 glass substrates and the SF11 hemi-cylindrical

prism were placed on the glass substrate; the prism was slowly lowered to avoid the

formation of air bubbles [75]. The RIMF was added to expel any air between the glass

substrate and the prism so that a consistent refractive index between the SF-11 prism and

the SF-11 glass substrate could exist.

An automatic fluidic system containing a 6-port valve was used for the protein

binding studies. Figure 29 shows the schematic representation of the flow cell and the

fluidic components. The Upchurch 6-port valve made of ceramic was designed to avoid

accumulation or dead volume, which prevented mixing of the different fluids. The fluid

was directed to the flow cell from a port valve that contained different switches. The

switches alternated manually between a nitrogen gas line, the buffer PBS, the solution

containing the BSA in PBS, and the ethanol line (Figure 29).
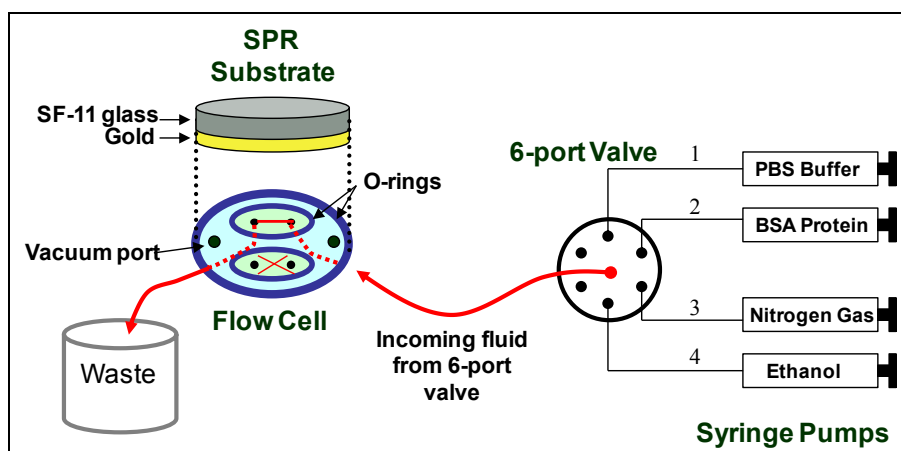
Figure 29. Scheme of the automatic fluidic system and the flow cell. Syringe pumps provide the pressure; the 6-port valve allows the analyst to interchange to a desired solution.

The flow rate was set to 1 mL/min in the programmable syringe pump for both the protein solution and the buffer solution. The syringe pumps provided the pressure to drive the fluid into the 6-port valve. Once the substrate was placed on the flow cells, a SPR air base line was obtained, and the buffer flowed through the cell to generate a buffer baseline SPR curve. Any extra buffer was removed by flowing N_2 from the gas line. The switch was turned to the protein solution line, and 2 mL of the solution flowed through the cell at 1.0 mL/min. The flow cell was washed with PBS buffer to remove unbound protein, and the SPR curve was recorded. Finally, ethanol was used to wash the tubing and the flow cell, and the components were dried with flowing nitrogen gas. The tubing used in the fluidic system was made of Tefzel, a fluorinated copolymer material highly resistant to a wide range of solvents; the tubing had an inside diameter of 0.03 inches. This material was chosen because of its inert properties in the presence of biomolecules and its high resistance to many organic and inorganic solvents.

While pumping the solutions, an analyst must pay attention to the flow cell assembly for leaks. If the system leaks, this can produce false data. Leaks are an indication of one of two things: either the o-rings are torn, or there is low suction pressure between the SPR substrate and the o-rings. Visual inspection of the o-rings can fix the problem, and checking the vacuum valve and cleaning up the vacuum ports can eliminate future leaking problems.

4.3.2   Atomic Force Microscopy

Atomic force microscopy was used to characterize the surface of the substrates with a Digital Instruments Dimension 3100 atomic force microscope. The micrographs

were obtained at a resolution of 10 nm in tapping mode with 1.0 Hz scan rate with tips

made of silicon nitride of spring constant 1 N/m. Figure 30 shows the tapping mode

AFM setup, where topography changes on the SPR substrates were detected by the

reflected laser spot on top of the cantilever; data were collected and analyzed by the

photo detector. This method provided information on the uniformity of the porous and

dense substrates by obtaining the root mean square (RMS) roughness values for 1 μm and

5 μm magnified images. The RMS values indicated the smoothness and uniformity of

the coverage of the organosilicate films on the SPR substrates. Furthermore, the stability

of the porous and dense surfaces was analyzed by AFM when the surfaces of the SPR

substrates were transformed by chemical functionalization with APTMS or PEG. In

addition, AFM was used to visualize some of the silica nanoparticles in the early studies.
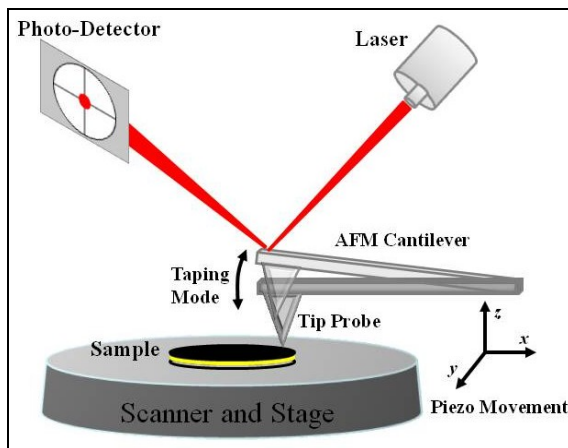
Figure 30. AFM setup in tapping mode displaying the main components: the tip, the
laser beam, the photo detector, and the sample.

4.3.3   Scanning and Transmission Electron Microscopy

Topcon 002B transmission electron microscope running at 200 kV was used to

image the silica nanoparticles and the ordered porosity SPR substrates. The ordered

porosity SPR substrate was prepared into cross-sections by Leslie Krupp at IBM using in-

house procedures. The silica nanoparticles were deposited on copper grids and dried

under vacuum before imaging in the TEM. For the silica formation on star polymer

studies, the particles were imaged with a Hitachi S-4700 cold field emission scanning

electron microscope at 3.0 to 9.0 kV electron charge. To prepare the samples for SEM

imaging, the templated silica nanoparticles were spun coated on a silicon wafer at 3000

rpm for 30 s. Then the silicon wafers were cured at 110 °C for 1 min to completely dry

the surface of the wafers prior to SEM characterization. Figure 31 shows the main

components of a SEM and a TEM microscope.
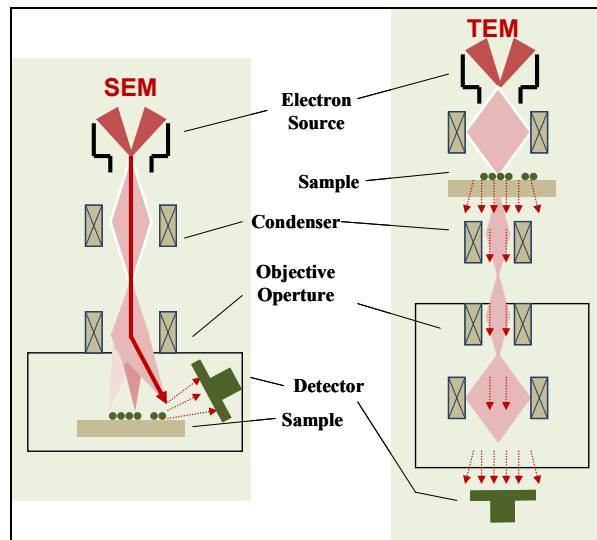
Figure 31. SEM and TEM microscope setup. The electrons pass through the sample in
the TEM configuration, while the electrons are reflected on the SEM configuration
(Adapted from the Opensource Handbook of Nanoscience and Nanotechnology).

One of the most important parameters of the electronic configuration of the setups

in Figure 31 is the way in which the electrons traveled through the sample. In the SEM

configuration, the electrons were reflected from the sample surface; these electrons were

analyzed and collected by the detector. The SEM images generated by these reflected

electrons revealed topological features on the surface of the particles. In the TEM

configuration, the electrons passed through the sample, and the electrons were collected

by a detector located downstream. The TEM images generated by these penetrating

electrons revealed structural features of the inside and the outside of the silica

nanoparticles.

4.3.4   Spectroscopy

For the absorption studies, an 8453 Agilent UV-visible spectrophotometer

containing a photodiode array was used to simultaneously measure the complete UV-vis

spectrum within seconds. When the solution was organic, 1.0 cm wide glass cuvettes

were used; when the solution was aqueous, plastic cuvettes of the same size were used.

Porphyrins strongly absorb light in the visible region of the spectrum. Therefore, UV-vis

spectroscopy, which absorbs at 419 nm, was used to monitor the relative concentration of

the occluded porphyrins within the silica particles. UV-vis spectroscopy was a crucial

tool to determine the porphyrin flux rate through the porous silica shell relative to the

shell thickness of the silica nanoparticles. Dansyl alkyl amides, which strongly absorb at

334 nm, were used to determine the relative amounts of the dansyl groups on the surface

relative to the porphyrin amounts inside the silica nanoparticles. Therefore, UV-vis

spectroscopy was used to determine the accessibility of the amino groups on the surface

of the activated silica nanoparticles. Dansylated amino groups generated a distinct

absorbance peak at 334 nm, indicating that the amino groups were suitable to undergo

further chemical reactions.

Fluorescent spectroscopy using a Fluorolog® Jobin Ivon-SPex spectrophotometer from Instruments S.A. (Edison, NJ), armed with a laser lamp with pulse duration less than 200 ps and peak wavelength of 399 nm, was used to construct a standardized set of curves using dansyl butanol ester. This dansylated compound was exposed to different solvents. The resulting set of fluorescent curves was used to determine the location of the solvatochromic dansyl compound when it was occluded inside the core of the star polymer (see further below) or when it was coupled to the external amino groups.

CHAPTER FIVE
RESULTS AND DISCUSSION

This chapter discusses two different manufacturing techniques that employ silica-based materials and have biotechnological applications. A short section of this chapter is dedicated to a 2D technique to build plasmonic silica-based biosensor substrates. The construction of the SPR substrates is briefly discussed; the nanostructuring of the organosilicate layer and the surface transformations are discussed in detail. The majority of this chapter is dedicated to a 3D technique to generate dye-occluded star polymers as templates for silica deposition. The synthesis, size control, cargo release, and surface transformations are discussed in detail in this chapter. As illustrated in Figure 32, the development of the 2D and 3D techniques is also discussed.
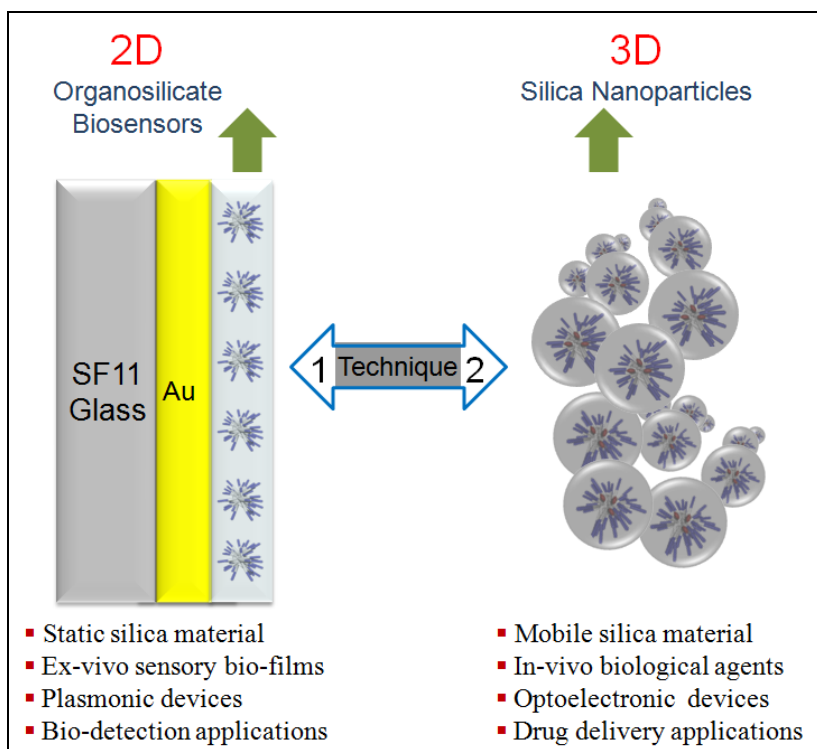
Figure 32. Organosilicate-based plasmonic biosensors (2D) and star polymer templated silica nanoparticles (3D) as powerful tools in nanobiotechnology.

5.1   Organosilicate-Based Plasmonic Biosensors

5.1.1   Characterization of the SPR Substrates

The SPR substrates were constructed as mentioned in Section 4.2.1. The
substrate holder on the evaporator accommodated 9 glass substrates. It was necessary to
determine the uniformity of the gold vapor deposition by examining the plasmonic
responses of a set of SPR substrates. Figure 33 shows the uniformity of the plasmonic
responses of SPR substrates that were deposited by physical thermal evaporation. The
box located in the lower right corner shows the position of the substrates with respect to
the substrate holder. The plasmon minimum was $35.66 \pm 0.012°$ of the set of SPR
substrates, suggesting that each SPR substrate had similar physical properties
independent of the location on the holder. The SPR substrates were UV-ozoned to
remove contaminants from the surface and to improve the uniformity of the subsequent
organosilicate deposition.
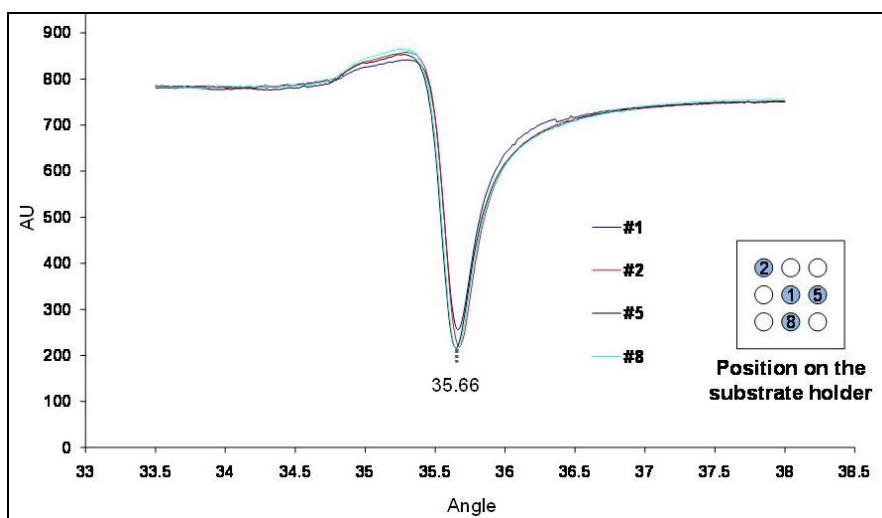
Figure 33. Plasmonic responses of a set of SiO_2 SPR substrates originated from the same
production batch. The position of the substrates inside the substrate holder is shown in
the box at right.

5.1.2   SPR Characterization of the Organosilicate Layer

Current sensory studies use planar surfaces to detect different biomaterials. We

used an organosilicate-based layer to construct a chemically functionalized surface with

physical features (Figure 34). The planar SPR biosensor (a) can be used to analyze

biomolecules with different sizes. The added porosity (b) on the SPR biosensors

increases the surface area and accommodates more receptor molecules to increase the

binding events with the target analyte. Furthermore, the added porosity provides greater

selectivity that can be used to screen out larger unwanted proteins (Figure 34(b)).
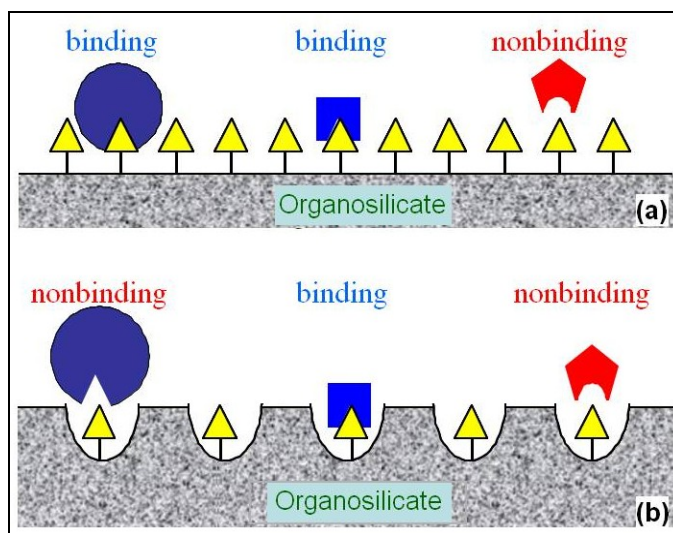
Figure 34. Conceptual scheme of the porous surface-modified biosensor. A featureless
planar sensor (a) and a porous sensor (b) have the selectivity capabilities to screen out
larger biomolecules by the physical features on the porous sensor.

The organosilicate (OS) SPR substrates were prepared as mentioned in Section

4.2.2-3. In order to determine the uniformity of the OS deposition, the plasmon

responses of a set of OS-SPR substrates were analyzed by SPR. Figure 35 shows the

plasmon responses of a set of OS-SPR substrates and displayed common resonance

angles at 36.92 ± 0.017º. The resonance angles of the OS-SPR substrates were shifted to

the right with respect to the empty SiO$_2$ (dashed blue curve); the refractive index of the

SPR substrate changed due to the OS deposition. This study demonstrated that the OS

deposition was uniform.
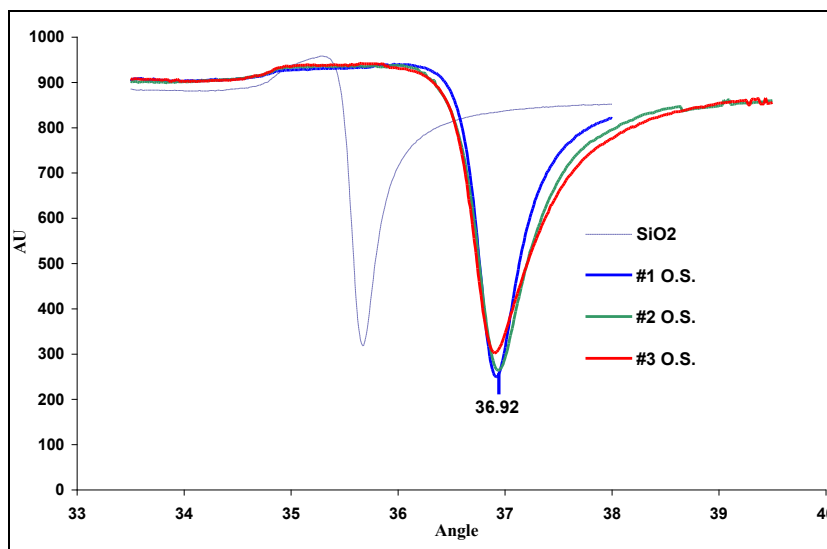
Figure 35. Uniformity of the organosilicate deposition analyzed by SPR. Angular minimum shifted to the right compared to the empty gold substrates (dashed blue curve) because the OS deposition changed the refractive index of the layer.

Even though uniform organosilicate SPR substrates were obtained with similar

physical properties, comparisons were made using batch-to-batch SPR substrates in each

experiment. This ensured accurate information regarding the physical and chemical

changes occurring at the surface of individual SPR substrates.

5.1.3   Porosity of the Organosilicate Layer

Previous studies on organosilicate SPR substrates indicated that the optimum

concentrations for the organosilicate precursor (MSSQ) and the porogen solution were

2.5% w/w [70]. Therefore, SPR substrates with these concentrations were prepared with

67

different porosity values using star polymers (porogens) mixed with the organosilicate solution. The porosity was expressed in percentage values; these values related to the loading of the organosilicate solution (Section 4.2.2). For 20% porous films, the porogen/MSSQ ratio was 1:4 w/w; for the 40%, 2:3 w/w; and for the 60%, 3:2. This indicated that when the ratio increased, the amount of porogen and the porosity increased as well. Porous SPR substrates with these values were prepared, and the substrates were spin coated and cured at 450 ºC.

In theory, the resonance angles from substrates with more pores would shift to the left because less material would be deposited. Figure 36 shows SPR curves that resulted from different porosity values.
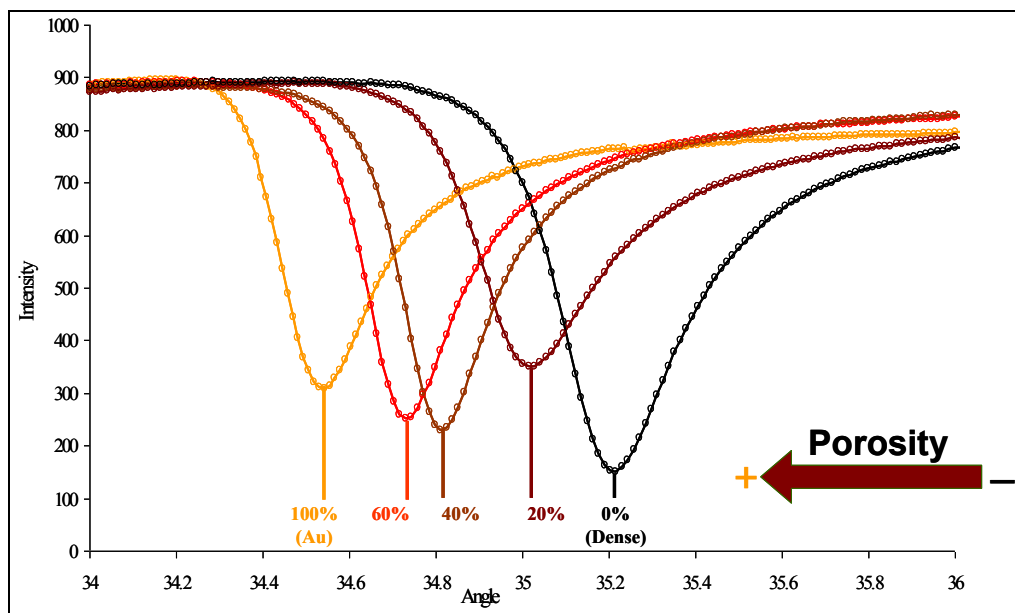
Figure 36. Angular shifts from porous SPR substrates with respect to porogen loading. The 100% porous curve is the SPR substrate without organosilicate layer. The 0% curve is the 2.5% MSSQ solution without porogen, and the 60, 40, and 20% curves are the organosilicate solutions with the specified porogen loading.

When loaded onto the substrates, the porogens produced more pores after the curing process. As the number of porogens increased, the density of the porous organosilicate layer decreased; the empty spaces lowered the refractive index and shifted the resonance angle to the left. When the solution did not contain porogens (0%), a nonporous film was generated upon curing; this dense layer had the highest refractive index. This unique SPR substrate generated a maximum resonance angle as shown by the black curve in Figure 36 (0%). The resonance angles of the porosity results were compared with theoretical values [70] and similar results were obtained (Table 3).

Table 3. Resonance angles of various porosities compared to theoretical values [70].

Porosity (% loading)	Value (degree)	Theoretical (degree)
0 %	36.98	NA
20%	36.64	36.52
40%	36.26	36.28
60%	36.11	36.04
80%	NA	NA
100%	35.57	NA

The porosity values were plotted against the resonance angles and a linear relationship was obtained with an excellent R^2 value (Figure 37). This linear relationship helped to determine the optimum porosity loading of 40% for the subsequent construction of SPR substrates. Therefore, the optimum concentration of the MSSQ was 2.5% by weight, and the optimum loading to generate the porous SPR substrates was 40%.
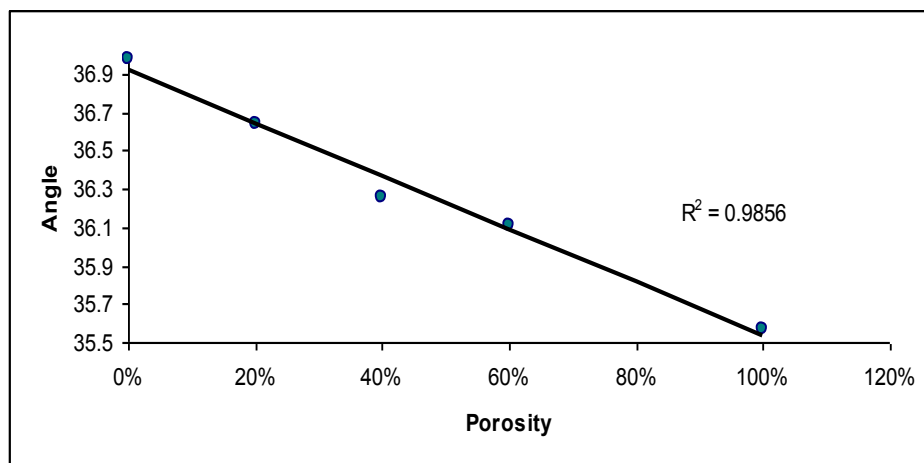
Figure 37. Porosity *vs*. resonance angle. A linear relationship with a R^2 value of 0.9856 was obtained.

5.1.4 Nanostructuring the Organosilicate Layer

The SPR substrates were nanostructured using different methods to generate three distinct morphologies (Section 4.2.3). Figure 38(a) shows a featureless SPR substrate obtained from a dense 2.5% MSSQ w/w organosilicate solution. When the 40% porogen solution was mixed with MSSQ solution, a random porosity surface (b) was obtained after curing the SPR substrates. Ordered porosity (c) was generated when the block copolymers self-assembled onto the surface (*via* phase separation) and the organosilicate associated with only one part of the block copolymer. When thermally cured, the polymer was removed and the organosilicate fused in an ordered porous array on the surface of the SPR substrate. SEM and TEM were used to characterize the pore size of the SPR substrates.

70
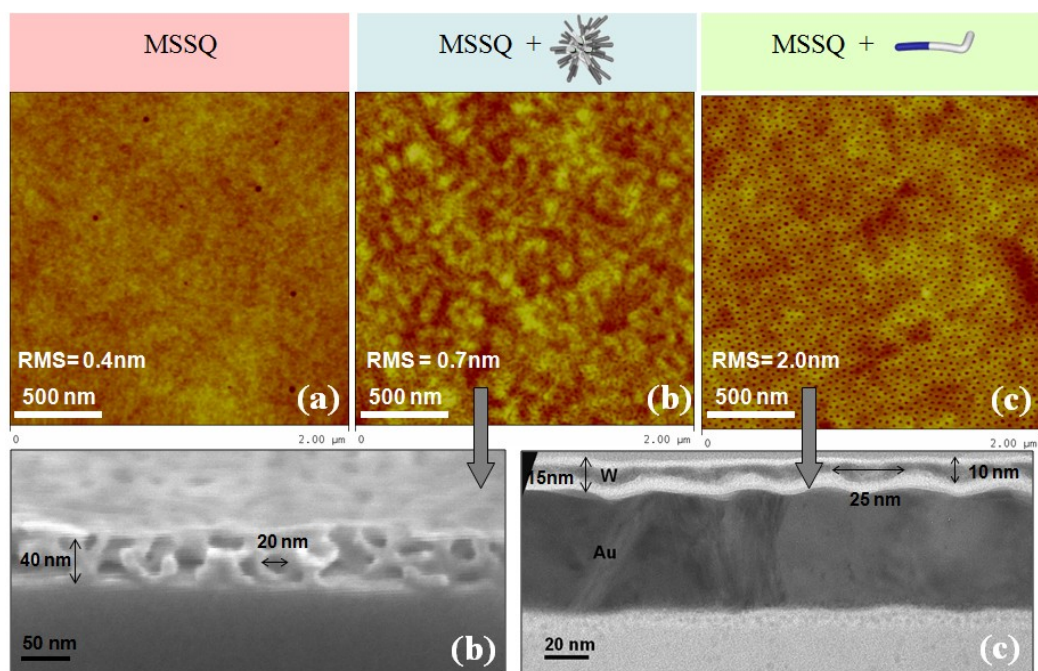
Figure 38. AFM micrographs showing three different surface morphologies on the SPR substrates: featureless surface from dense films (a), random porosity from porogen (b), and ordered porosity from block copolymers (c). SEM image bottom (b) and TEM image bottom (c) provided information on pore sizes.

The thickness of the organosilicate/porogen layer was about 40 nm; the diameter of the pores was approximately 20 nm as depicted in the SEM micrograph in Figure 38(b-bottom). However, the organosilicate/block copolymer layer was only 15 nm thick, with pores that averaged 25 nm in diameter (Figure 38(c-bottom)). The organic polymers thermally decomposed to generate the desired morphologies during the curing process. However, the organosilicate surface contained cross-linked silanols that needed to be liberated for further chemical reactions. Therefore, the organosilicate layer was exposed to UV-ozone treatment [76] to activate the surface for further chemical functionalization.

5.1.5   Surface Activation of the SPR Substrates

In order to liberate the cross-linked silanol groups on the surface of the substrates, UV-ozonolysis was performed. An optimal treatment time was found by subjecting the SPR substrates to different exposure times. Shorter times generated partially activated surfaces, and longer times damaged the organosilicate surface. Therefore, the optimum time was determined to be 5 min. The activation of the surface was monitored by contact angle measurements; the angle of the water droplet provided information on the chemistry of the surface. Figure 39 shows the UV-ozone analysis on a block copolymer ordered porosity substrate. The scheme (a) shows a representation of the silanol groups liberated due to UV-ozone exposure. AFM micrographs (b) show the porous morphology after the surface was UV-ozone exposed for 5 min; the porous surface was not altered by the UV-ozone exposure. Contact angle measurements (c) demonstrated that the organosilicate layer was nonpolar; thus, the silanol groups were cross-linked. After 5 min of UV-ozone exposure, the contact angle decreased from 83° to 39°; this indicated that the silanol groups were liberated, providing stronger attraction to the water droplet. The UV-ozone treated porous substrates were analyzed by SPR; ozonolysis data were collected before and after analysis. As shown in Figure 39(d), the resonance angle of the UV-ozone treated SPR substrate shifted 0.20° to the left, indicating that material was removed from the organosilicate surface. This was expected because UV-ozone is typically used to clean devices by removing surface materials; in this case, the material that was removed did not alter the morphology of the surface.
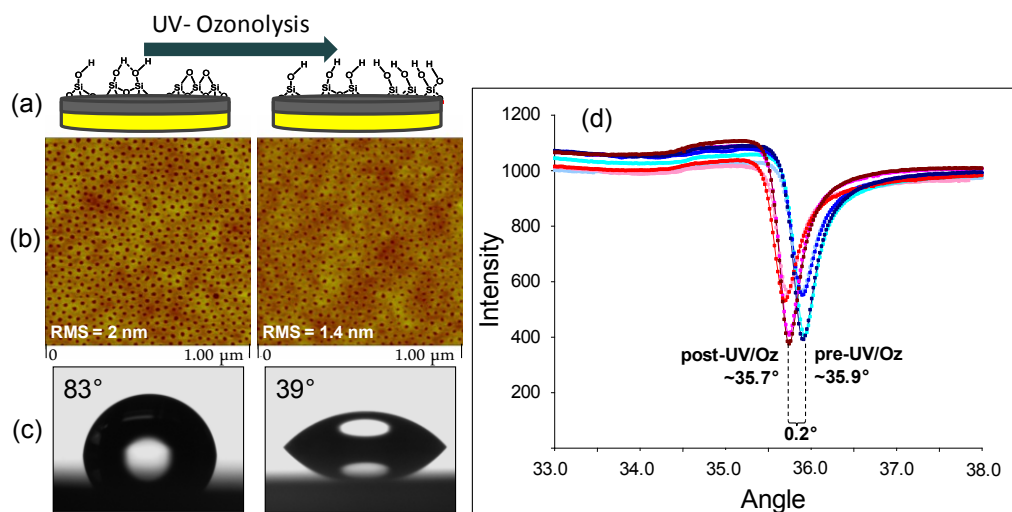
Figure 39. Surface activation of an ordered porosity SPR substrate by UV-ozonolysis. Scheme (a) shows the liberated silanol groups. This ozonolysis process did not affect surface morphology shown by the AFM images (b). Contact angles (c) decreased as the surface became hydrophilic. Resonance angles (d) had the same intensity but shifted to the left due to removal of materials from the surface.

An important observation was that the plasmon intensities did not decrease after the UV-ozone treatment. Therefore, 5 min of UV-ozone exposure was adequate to liberate the silanol groups without damaging the surface morphology and maintaining the same intensity of the resonance angles.

5.1.6   Surface Transformation of the Organosilicate SPR Substrates: Amination

Surface functionality of the SPR substrates was accomplished by vapor depositing APTMS to generate an aminated surface. This process was later modified into a more reliable procedure where APTMS was deposited using a solution-based method. The aminated surfaces were compared with the vapor deposition method, and similar results were obtained. When the substrates were aminated by vapor deposition or by solution-based deposition, contact angles were measured to determine the surface properties of the

substrates. SPR data ensured that deposition of APTMS occurred in all cases. As shown in the AFM micrographs (Figure 40), the morphology of the organosilicate layer was not altered by the surface transformation; more importantly, the RMS values (0.6 nm) did not change. The SPR measurements confirmed the successful deposition of APTMS when the resonance angle shifted from 36.6° to 36.7°. However, contact angle measurements were needed to confirm that the surface was chemically transformed from a silanol surface into an aminated surface.
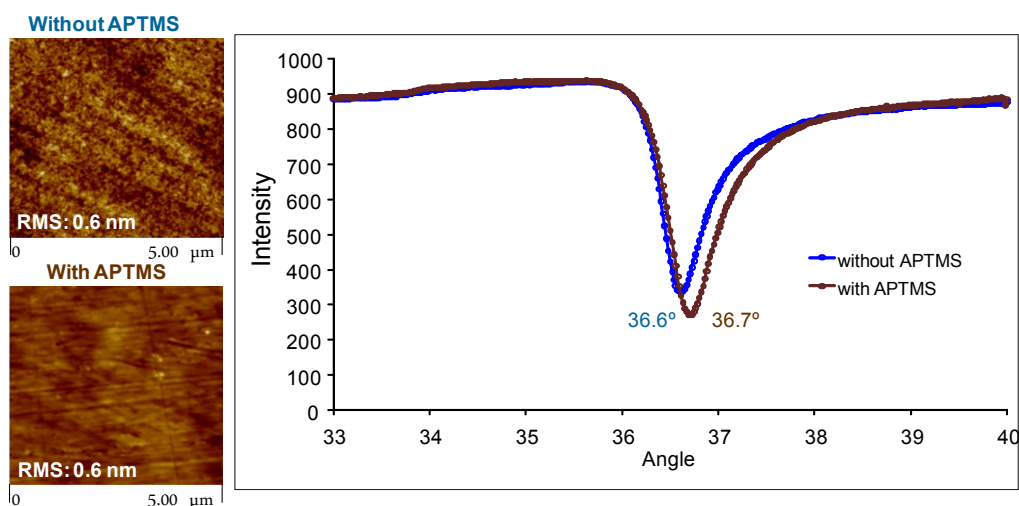
Figure 40. Solution-based APTMS deposition on dense films. AFM micrographs showed the unaltered surface by APTMS deposition The RMS value did not change. SPR data showed an angular shift of 0.10° due to APTMS deposition.

5.1.7   Surface Transformation of the Organosilicate SPR Substrates: PEGylation

Proteins are biologically synthesized in different shapes and sizes, and some proteins contain reactive groups that confer "stickiness" properties. A process of avoiding non-specific absorption was developed to prevent unwanted proteins from attaching to the SPR substrates. PEG is a well-known commercially available antifouling agent that can be obtained in different lengths [56]. Furthermore, PEG

polymers can be custom-synthesized to contain specific functional groups, antibodies, or

receptors for desired binding experiments. In the initial experiments, PEGylation of the

aminated SPR substrate was attempted using dicyclohexylcarbodiimide with carboxylic

acid terminated PEG polymers, but the reaction failed. The contact angle of the

aminated substrate was 63°, and that of the PEGylated substrate was 64°. Since PEG

polymers are more hydrophilic than amino groups, the results were inconsistent with the

physical properties of the surface. The PEGylation reaction was ineffective because the

contact angle did not decrease compared to the aminated surface. Therefore, NHS-

$(PEG)_7$-OMe, a more selective and reactive PEG polymer, was substituted in the

PEGylation reaction. A methoxy group protected the PEG polymer at one end; this

group forced the PEG material to react only with NHS located at the other end. The

NHS ester specifically reacted with primary amines ($-NH_2$) and provided efficient

PEGylation of amine-containing material as shown in Equation 7 [77].

$$\text{PEG}-\text{O}-\overset{\text{O}}{\overset{\|}{\text{C}}}-\text{CH}_2\text{CH}_2-\overset{\text{O}}{\overset{\|}{\text{C}}}-\text{O}-\text{N} \xrightarrow{\text{R-NH}_2} \text{PEG}-\text{O}-\overset{\text{O}}{\overset{\|}{\text{C}}}-\text{CH}_2\text{CH}_2-\overset{\text{O}}{\overset{\|}{\text{C}}}-\text{NH-R} \qquad \text{Equation 7}$$
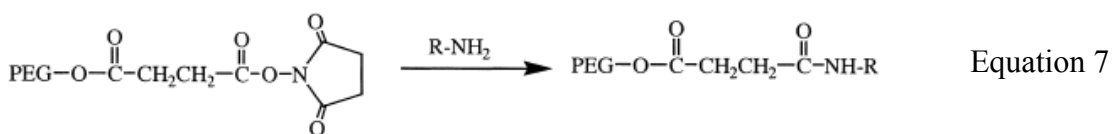
A reaction using 100 mg of NHS-$(PEG)_7$-OMe in DCM/TEA was performed at

room temperature for 24 h. Subsequently, contact angle measurements of the PEGylated

SPR surface were obtained. The measurements were compared to those of silanol and

aminated surfaces. Figure 41 shows the contact angles obtained after a complete surface

transformation of a 40% porous SPR substrate. In UV-ozone treatment (a), the

liberation of silanol groups increased hydrophilicity and reduced the contact angle from

97° to 20°. When the surface was treated with APTMS (b), the contact angle increased to 64°. PEGylation (c) reduced the contact angle to 55°.
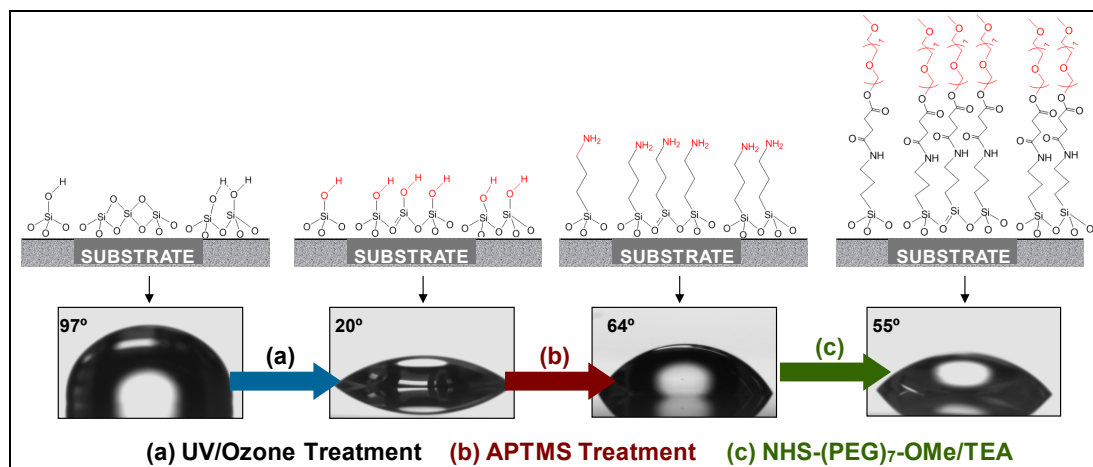
Figure 41. Contact angle measurements of a complete surface transformation of a 40% porous SPR substrate. UV-ozone treatment (a) lowered the contact angle from 97° down to 20°. Amination (b) increased it to 64°, and PEGylation (c) lowered it to 55°.

After treating the surface with NHS-(PEG)$_7$-OME, physical properties distinct from those of the aminated surface were discovered. The contact angle reduction was a key indication that the hydrophilic PEG polymers were successfully installed on the surface of the SPR substrate. PEGylation on the aminated surface was analyzed by SPR. Figure 42 shows the resonance angle of the aminated substrate that was shifted from 36.58° to 36.64° after PEGylation was achieved; this indicated that a PEG layer had been successfully deposited. The AFM micrographs in Figure 42 show that the surface morphology of the 40% porous SPR substrate was not altered by the deposition of PEG material.
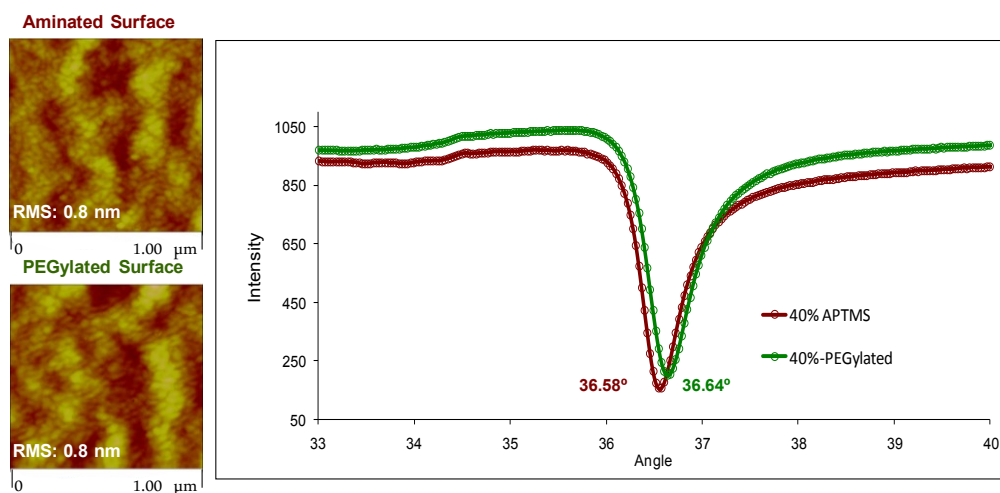
Figure 42. PEGylation of a 40% porous SPR substrate. Resonance angle was shifted 0.06° to the right, indicating a successful deposition of a PEG layer. The surface of the porous substrate was not affected, as depicted by the AFM micrographs.

5.1.8   Preventing Nonspecific Binding of Biomolecules

In order to determine if the PEGylated surface contained antifouling properties, the surface was exposed to a solution of proteins. By exposing the surface to a flow of proteins and measuring nonspecific binding, it was possible to determine the effectiveness of the reaction between NHS-$(PEG)_7$-OMe and the aminated surface. Additionally, the expected results promised to reveal whether excellent PEG coverage on the surface was accomplished. To determine whether a complete PEG coverage existed on the surface, a solution of protein bovine serum albumin (BSA) in phosphate buffered saline (PBS) was flowed over the aminated and PEGylated SPR substrates to investigate protein binding on the surfaces. The two curves at the left (green and purple) in Figure 43 are the plasmons of the amino and PEG coated surfaces in air. Once the buffer (without protein) was introduced into the flow cell, the curves shifted to the right because the buffer had a greater index of refraction than air. First, the 40% aminated SPR

substrate was exposed to the BSA solution, and an angular shift of 0.178° was generated.

As shown in the magnified square in Figure 43 (green curve), the 0.178° angular shift

was irreversible, even after the substrate was washed twice with 3 mL PBS (blue curve).

This suggests that the proteins permanently adsorbed to the aminated surface. When the

BSA solution was flowed over the PEGylated surface (red and black curves), an angular

shift was not observed. Thus, non-specific adsorption of protein was prevented by the

PEG layer.
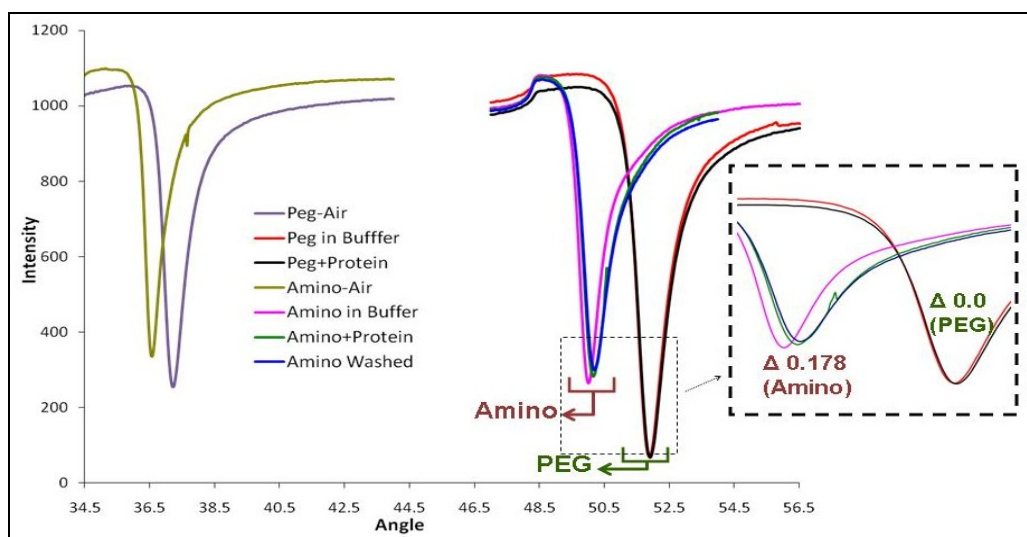
Figure 43. Adsorption studies of the protein BSA on aminated and PEGylated 40%
porous SPR substrates. The aminated (blue curve) did not have the PEG background and
generated an irreversible 0.178° angular shift. The substrate with the antifouling
background (red curve) did not have an angular shift.

When the same studies were performed on nonporous SPR substrates, similar

results were obtained. Figure 44 shows the SPR studies of an aminated and a PEGylated

nonporous substrate exposed to BSA. When PEG was present on the surface of the

nonporous substrate (b), a shift was not observed, but for the aminated substrate (a), an

irreversible 0.12° angular shift was produced. The kinetic data (a-bottom) indicated that

the protein adsorbed instantaneously onto the aminated surface; in the PEGylated

substrate, the protein did not bind.
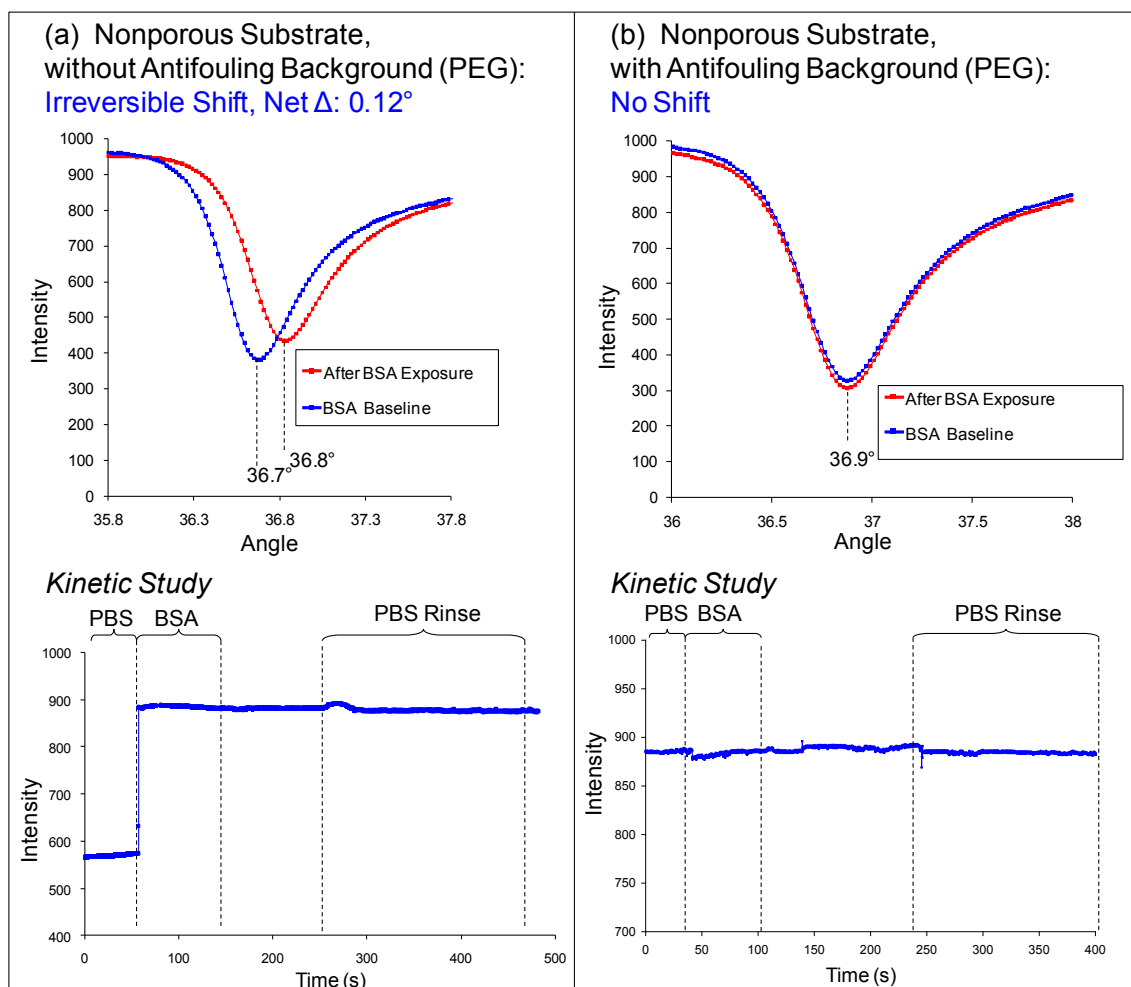
Figure 44. Absorption studies of the protein BSA on an aminated (a) and a PEGylated (b) non-porous substrate. The aminated surface without the PEG background generated an irreversible 0.12° angular shift, while the PEGylated surface showed no shift.

A methodology for constructing antifouling surfaces on SPR-based biosensor

with and without surface features was successfully developed and tested. Future studies

need to involve installation of specific biological receptors on the antifouling surface to

test for specificity of target analytes; these studies should be performed with different protein sizes to test for size selectivity.

5.2 Dye-Occluded Star Polymers as Templates for Silica Deposition

As shown in Figure 45(a), the overall concept of the 3D approach is to take the water-soluble core-shell star polymers, occlude the hydrophobic material inside, and form an occlusion complex. The shell of the star polymer is a poly(N,N-dimethylaminoethylmethacrylate) that contains a high density of amines; this allows the star polymer to be water-soluble. The shell provides amines, which are also excellent sites for silica deposition using the Stöber process (b).
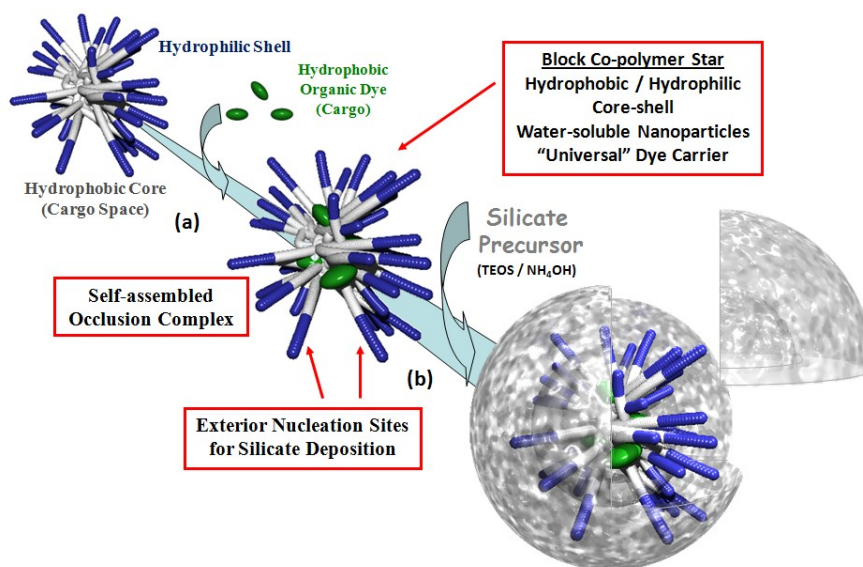
Figure 45. Scheme showing the development of 3D core-shell templated silica nanoparticles, from the occlusion complex (a) to silica deposition (b).

After the dye-occluded SNPs were generated, the particles were surface-transformed into passivated stable particles or into activated particles for further surface chemistry. Installation of hydrophilic material on the surface allowed the silica particles

80

to be biocompatible and water-soluble. In addition to allowing surface transformation of

the particles, varying the size of the particles allowed modifications of the shell

thickness in order to control the cargo release through the silica shell.

5.2.1   Making the Dye-Star Polymer Occlusion Complex

Star polymers have a polystyrene hydrophobic core and a polyamine hydrophilic

shell. This core-shell architecture creates a water-soluble nanoparticle with a

hydrophobic pocket inside [71, 72]. Porphyrin, a hydrophobic dye 2 nm in diameter, was

used to form an occlusion complex (Section 4.2.7). Figure 46 vial (a) shows a clear

solution of star polymer in water, and vial (b) shows the hydrophobic dye floating on the

water; the dye was not water-soluble. The hydrophobic dye was occluded into the core

using molecular self-assembly driven by the solvophobic forces provided by the solvents.

Figure 46 vial (c) shows the hydrophobic dye in water occluded inside the star polymers

after it passed through a 0.45 μm filter; the star polymer provided a space for the cargo

and water solubility.
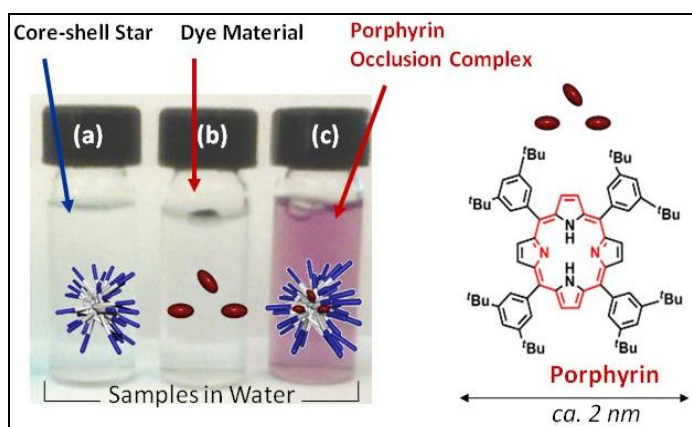
Figure 46. Water solubility of the star polymer, porphyrin, and the porphyrin occlusion
complex. The star polymer provided water solubility to the hydrophobic dye.

The solution in Figure 46(c) was uniformly reddish, and resuspension of this hydrophobic material in water was readily achievable. The porphyrin occlusion complex in water remained stable for weeks without any signs of the dye precipitating out of the solution. To prove that the dye was inside the star polymer, a set of fluorescent curves was constructed after exposing the dye dansyl butanol ester (DBE) to different solvents. The fluorescence emissions peaks provided information about the surrounding environment of the DBE fluorophore; this information was used to determine the location of the dye. DBE was occluded inside the polymer using ethanol, and the fluorescence of this dansyl occlusion complex (D-OC) was investigated. As shown in Figure 47, the D-OC fluorescent peak (orange curve) was not adjacent to the DBE peak in ethanol (blue curve), suggesting that the dansyl dye inside the star polymer was exposed to a different chemical environment.
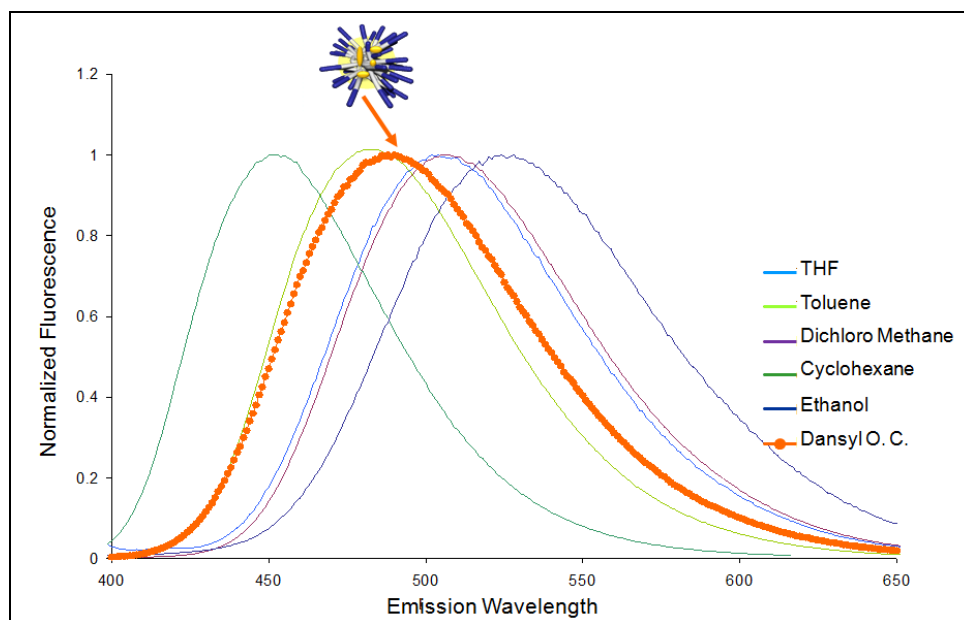
Figure 47. Dansyl butanol ester standardized fluorescent curves. The Dansylated compound was occluded inside the star polymer, as shown by the fluorescence curve in orange. Its fluorescence emission was close to the toluene fluorescence emission.

These results indicated that the dye was not in contact with the solvent. The emission signal of D-OC was instead similar to the toluene signal, which closely resembled the polystyrene core of the star polymer (Figure 47). Therefore, DBE was indeed inside the core of the star polymer. This unique method of occluding hydrophobic material into the core of the star polymer to make it water-soluble allows for a general "Trojan horse" approach, i.e., any dye/drug can be loaded inside the star polymer. The focus of this study was not to coat the star polymer with silica; rather, the embedding of the cargo into the star polymer and the encapsulating of this complex with silica give importance to this study. Therefore, rather than modifying each individual cargo to be encapsulated with silica, a single star polymer was engineered to execute two important roles. First, it would allow any type of drug/dye to be occluded into the core; second, it would function as a template for silica deposition. In other words, the complex with the material that was loaded *via* the "Trojan horse" approach could be encapsulated with silica.

5.2.2   Silica Deposition on Star Polymers

In the first experimental trials, the initial amounts of the reagents were similar to literature values, but aggregated particles were obtained with those literature values. The aggregated SNPs (Figure 48) were generated after a 24 h reaction time (T) using 10 mg of template, 250 μL of TEOS, and 1.0 mL of NH_4OH in 18 mL of ethanol. We postulated that the polyamines on the arms of the star polymers had a chemical effect on

83

the Stöber method. Therefore, the reaction was modified to improve the dispersity of the

particles and to minimize aggregation.
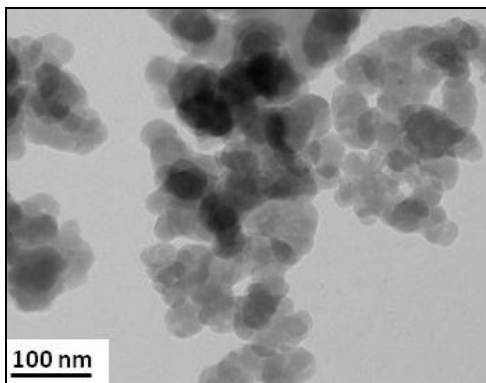
Figure 48. TEM micrographs of templated silica nanoparticles generated by the Stöber
method at room temperature for 24 h reaction time. These reaction conditions generated
aggregated silica nanoparticles.

Since the previous reaction conditions generated aggregated SNPs, modifications

of the current experimental conditions were necessary. The newly modified experimental

conditions consisted of four major steps: reducing reaction time to improve dispersion;

exchanging toluene solvents to remove ethanol; passivating with HMDS to reduce

aggregation; and centrifuging the SNPs to resuspend the particles in a suitable solvent.

The SNPs generated with the modified experimental conditions displayed improved

morphology. As shown in the TEM micrographs in Figure 49, the SNPs formed a

"necklace" configuration that still showed signs of aggregation, but the particles had an

overall spherical shape. When the centrifuged SNPs were resuspended in a combination

of toluene/THF, the suspension became clear (a), whereas the SNPs that were

resuspended in ethanol became cloudy (b). The particles aggregated to a greater or lesser

extent depending on the solvent used, but the solvent combination of toluene/THF

yielded a more desirable resuspension.
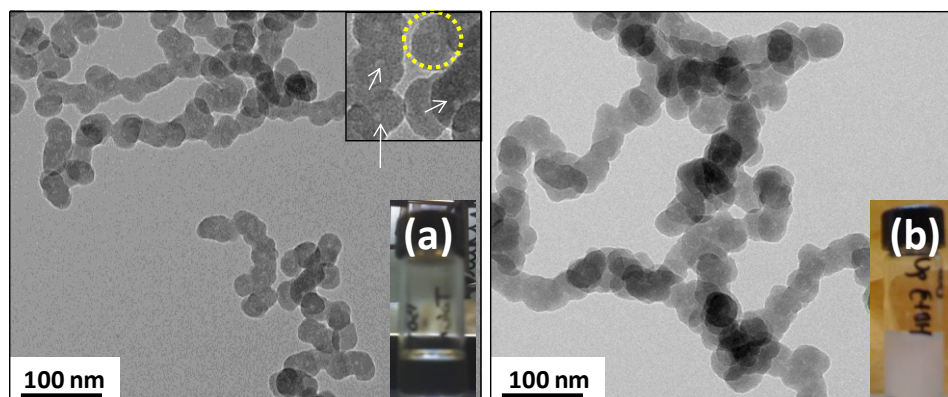
Figure 49. TEM images of templated SNPs generated by reducing the reaction time and by resuspending the isolated SNPs in toluene/THF (a) and in ethanol (b).

One unique aspect of these SNPs was the appearance of a white spot in the middle of the particles, as shown by the arrows in Figure 49. This indicated that the composition of the center of the particles was of a lighter material—in this case, the star polymer. The Stöber reaction was further modified to improve dispersity of the silica nanoparticles. The reaction time was reduced to 3 h, the volume of ammonia to 0.85 mL, and the volume of TEOS to 125 μL. The particles obtained in this trial provided a better perspective on the chemistry involved in this process. The TEM images in Figure 50 clearly indicate that once the particles formed, they began sticking to each other, forming the "necklace" configurations. The black arrows point to the nanosized junctions where aggregation originated. Reaction time and TEOS concentration were important factors in determining the overall growth of the SNPs. The size of the particles was similar when the reaction time was either 24 h or 3 h. This indicated that the Stöber deposition of silica occurred relatively quickly. For this reason, it was necessary to investigate the reaction time in detail to understand why aggregation occurred.
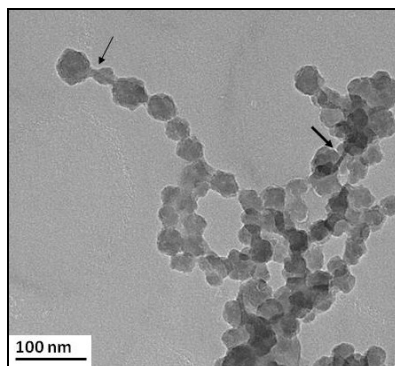
Figure 50. TEM micrographs depicting the particle formation when the reaction time was reduced to 3 h, and the volume of TEOS was reduced by 50%. The arrows point to the nanosize silica junctions that indicate the beginning of the aggregation problem.

5.2.3   Study of Reaction Time and Particle Growth

In order to determine when aggregation was occurring, particle growth with periods shorter than 3 h was investigated. To aid in isolating and characterizing the particles, the reaction was stopped at certain specific times to determine at what moment aggregation occurred. For the first experiments, AFM was used to characterize the SNPs because it provided quicker results, allowing for faster chemical modifications. The dye was not occluded inside the star polymer until the chemical reaction was controlled. After the particles were synthesized using the Stöber method, the reaction was stopped at 30-min and 60-min by pouring the reacting solution into 300 mL of toluene. The solvents were thermally removed under vacuum, and this cycle was repeated two more times to completely remove ethanol and ammonia. Exchanging the solvents created growing conditions inhospitable to silica; at the same time, the volume of the SNPs was reduced to 15 mL. The samples were spun coated on a silica wafer and imaged by AFM. As shown in Figure 51, the AFM analysis demonstrated that the particles obtained in this experiment were not aggregated, unlike those obtained in the 24-h reaction shown in

Figure 51(T=24 h). The particles obtained with the revised process were similar in size and were evenly dispersed. The average diameter (D_{ave}) of the particles obtained in the 30-min reaction (left panel) was 33 nm, and the D_{ave} obtained in the 60-min reaction was 38 nm (middle panel).

| T = 30 min (D_{ave} = 33 nm) | T = 60 min (D_{ave} = 33 nm) | T = 24 h (aggregates) |

200 nm   200 nm   2000 nm
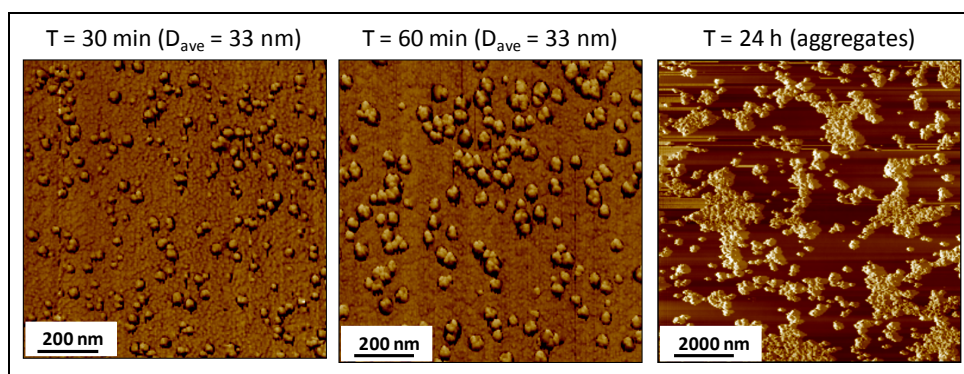
Figure 51. AFM images of the reaction-time study on particle growth with a 30-min reaction, a 60-min reaction, and a 24-h reaction. The particles generated in the 30-min and 60-min reactions showed excellent signs of monodispersion compared to those produced in the 24-h reaction.

This study clearly indicated that aggregation occurred after 60-min of reaction time. However, because it was necessary to determine the particle growth behavior of this system more precisely after the 60-min mark, a more detailed investigation of reaction time was required.

5.2.4 Particle Growth Using Step-Wise Addition of TEOS

The "seeded" method [22] for silica growth was used to generate the particles using three 10-min time intervals, adding 50 µL of TEOS at each time interval. Thirty minutes after the first stepwise addition, the particles were collected every 15 min and analyzed by TEM. As depicted in Figure 52, the particle growing behavior was captured by the TEM analysis, and the SNPs stopped growing at approximately 120-min.
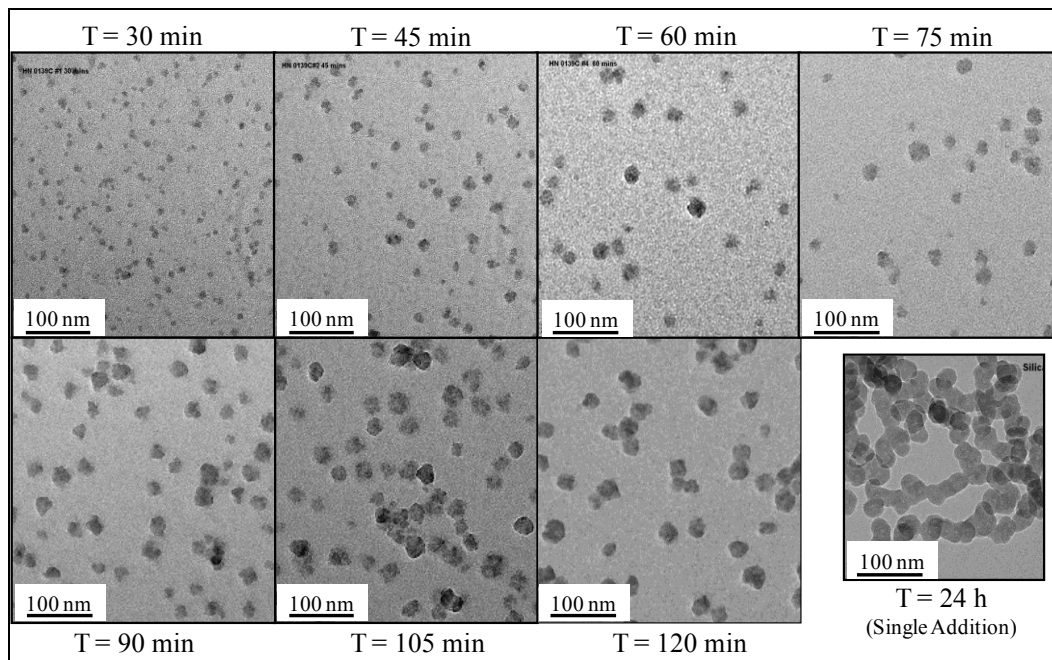
Figure 52. TEM images showing the growing behavior of the SNPs using stepwise addition of TEOS. After 30 min, the SNPs were characterized by TEM every 15 min; after 2 h the particles stuck together, forming small aggregates.

The particles began to grow early in the reaction and reached their peak size 120-min after the first addition of TEOS. After 120-min, the particles began to form small aggregates, as depicted in Figure 52 (T=120 min). Reaction schemes of lengths other than 120-min were necessary to completely investigate the specifics of the reaction over time, so SNPs were also synthesized and imaged at the 180-min mark.

Figure 53 shows TEM image of the SNPs generated during this 180-min trial. At 135-min, the particles started forming groups of 5-12 particles with plenty of individual SNPs; bigger aggregates appeared at 150-min with fewer individual particles. When the reaction continued to 165-min, large aggregates were formed and no individual SNPs were observed. When the reaction reached 180-min, the SNPs formed a huge network of aggregated particles. Based on these findings, 120-min was the optimum time for the

particles to reach their final size before aggregation began to occur; therefore, the 120-min reaction time was used for subsequent particle generation.

| T = 135 min | T = 150 min | T = 165 min | T = 180 min |
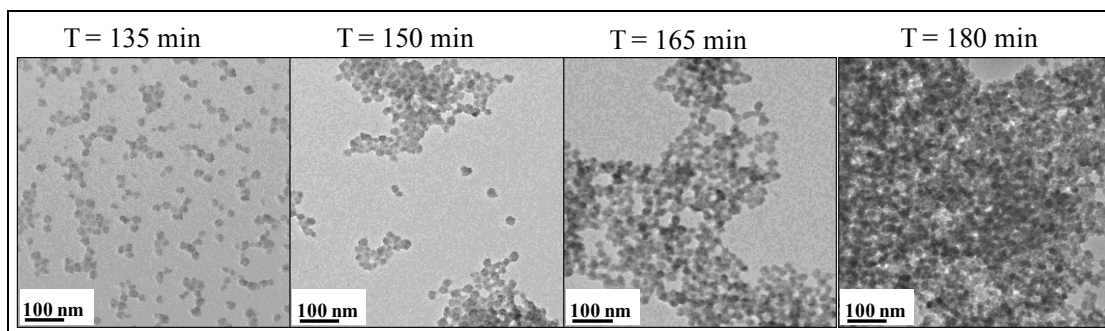
Figure 53. TEM images showing the reaction time study using stepwise addition of TEOS at the 180-min mark. The reaction was stopped at 135, 150, 165, and 180-min from the initial addition of TEOS, and the particles showed increased aggregation with increasing reaction time.

The stepwise reaction time study indicated that two hours was the optimum time to grow the SNPs; this reaction time provided non-aggregated SNPs. Therefore, with the optimized reaction time (120-min), SNPs were generated and the diameter and dispersity of the particles were measured. As shown in Figure 54(a), the upper histogram depicts the results of the size distribution of 100 particles. The majority of the particles were between 26 and 30 nm—a narrow size distribution. The lower histogram in Figure 54(b) shows the dispersity measurements of 100 particles; most of the particles were monodispersed, as shown by the left bar of histogram (b). Using the processes described above, ideal experimental conditions for generating monodispersed, star polymer-templated silica nanoparticles were determined. Once monodispersed SNPs were generated, the next step was to reproduce these results with the dye inside the star polymer. Therefore, silica encapsulation of a dye-occluded star polymer was investigated.
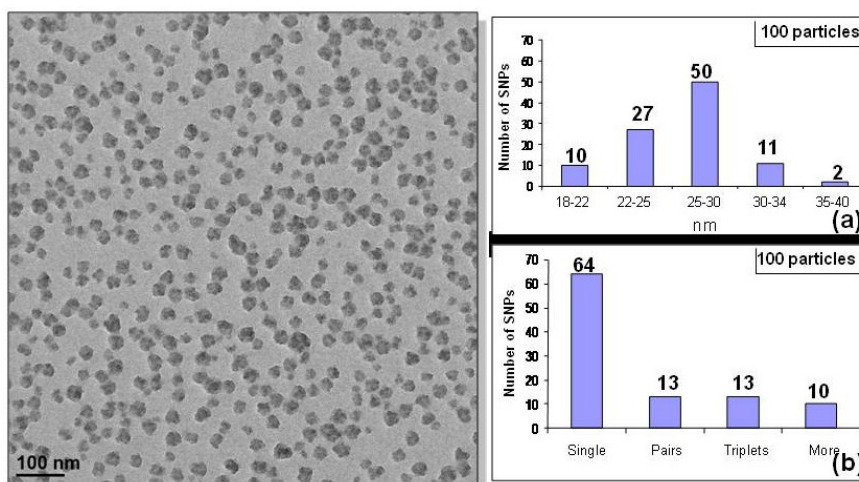
Figure 54. Particle size distribution and degree of aggregation for the 2-h reaction time. Most of the particles were monodispersed and between 26 and 30 nm in diameter, as shown by the TEM micrograph.

Silica encapsulation was performed on a porphyrin occlusion complex using the Stöber reaction, which was stopped at 120-min. The templated SNPs were isolated and characterized by TEM. As shown by the TEM image in Figure 55, the generated dye-occluded star polymer templated SNPs, showed excellent monodispersity and size uniformity. It was postulated that the occluded dye extended the arms of the star polymers. As a result, the deposition of silica was facilitated, generating more uniform silica nanoparticles compared to the particles without the occluded dye. Therefore, a method to encapsulate dye-occluded star polymers with silica was developed; this method was called the two-step method or "two-pot." The encapsulation of the dye-occluded star polymers with silica was the first step; passivation of the surface with nonreactive material was the second. In this "two-pot" method, the first general step (particle formation) generated reactive particles, which contained plenty of silanol groups on the surface.
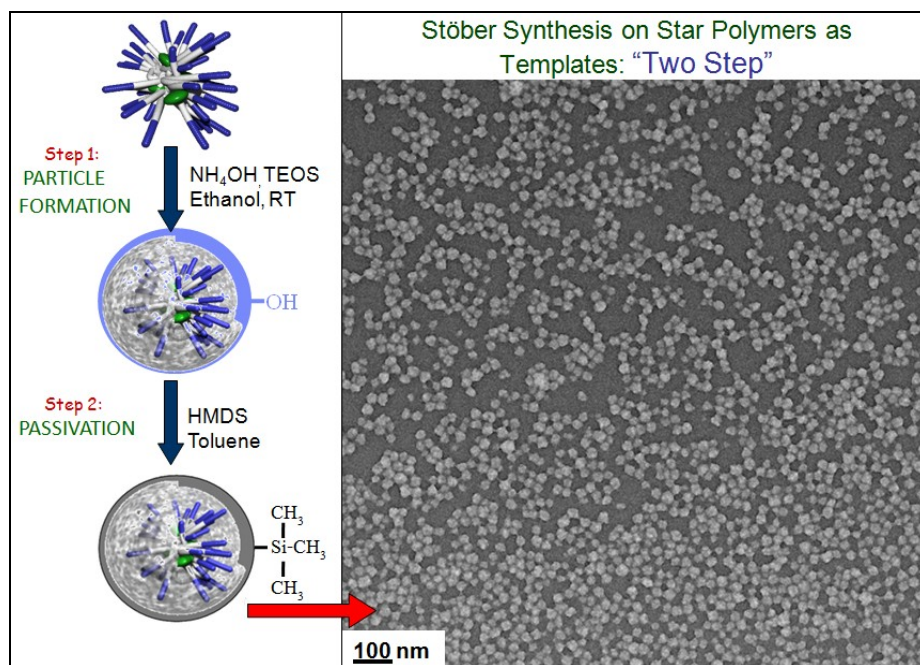
Figure 55. TEM image of monodispersed SNPs generated using a "two-pot" approach. The two steps are the 120-min Stöber particle formation of the porphyrin occlusion complex (1) and the HMDS passivation (2). The diameter of the generated SNPs was approximately 25 nm.

The reactive silanol groups (-Si-OH) depicted by the blue coating in the scheme in Figure 55 made the particles stick to each other, leading to aggregation. The second general step was the passivation of the particles with unreactive trimethyl groups from HMDS to prevent aggregation (shown by the gray coating in the scheme in Figure 55). The "two-pot" method, which worked perfectly, generated uniform monodispersed SNPs (Figure 55).

5.2.5 Synthesis of Templated SNPs Using a "One-Pot" Approach

The challenges involved in synthesizing nanosized SNPs can be overcome by using small templates such as star polymers. A method to put material within the star polymers and coat these dye-occluded templates with silica allows scientists to obtain

very small and uniform silica nanoparticles using a "two-pot" approach. This process

generates excellent SNPs, but it requires extensive solvent and sample handling.

The possibility of making this method simpler with the one-step or "one-pot"

approach was investigated. This method would reduce the handling time of the particles

and reduce solvent use. However, some experimental changes were made to the SNP

generation process to make the method simpler and more successful, especially in the

passivating agent, since HMDS reacts with ethanol. Trimethylethoxysilane (TMES) was

chosen as a replacement for HMDS because it reacts with surface silanols in the presence

of ethanol, coating the surface with non-reactive methyl groups. All of the reagents were

added to a single reaction vessel in a sequential manner to generate and passivate the

particles. Other than the change in the passivating agent, this new approach used the

same reaction conditions as the "two-pot" method. After 120-min of reaction time,

excess amounts of the new passivating agent were added. As seen in TEM micrographs

in Figure 56, the particles obtained by this method were approximately 30 nm in

diameter, but showed significant signs of aggregation.
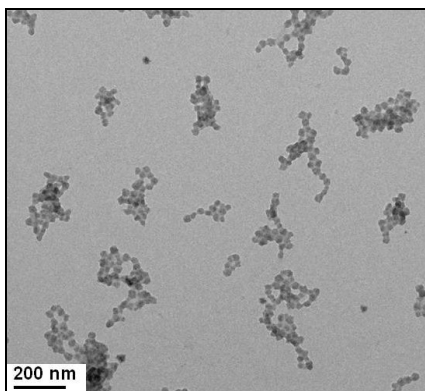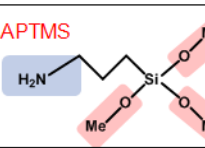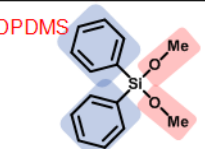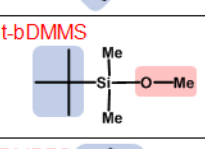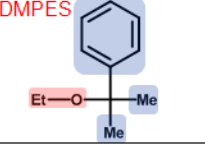
Figure 56. TEM micrograph of templated SNPs synthesis using the "one-pot" approach
at 120-min reaction time. The passivating agent TMES was added in excess, but particles
still showed aggregation.

These results were promising, however, because the particles, although aggregated, were at least generated with the simpler "one-pot" method. Since TMES did not prevent aggregation, various silylation (surface-passivating) agents were investigated to passivate the "one-pot" SNPs. In a separate trial, a passivating agent was added at 90-min instead of 120-min from the beginning of the synthesis to ensure that aggregation was not occurring as a result of the Stöber synthesis; based on the results from Section 5.2.4, aggregation occurred after 120-min. Four silylation agents were tested as possible alternatives to TMES: APTMS, DPDMS, t-bDMMS, and DMPES. After the addition of each silylation agent, the reaction was allowed to proceed for a few hours. The SNPs were then visually investigated for signs of flocculation (i.e., white flakes indicative of aggregation). Table 4 shows the four different silylation agents with optical images of the reaction that took place in each case after a few hours.

Table 4. Different silylation agents and their ability to passivate the "one-pot" SNPs.

Agent	Image	Comments
APTMS		No visible aggregation after 24 h
DPDMS		No visible aggregation after 24 h
t-bDMMS		Aggregation after 2.5 h
DMPES		Aggregation after 2.5 h

The number and length of the alkoxysilanes R-O-Si- groups (shaded in red) in each silylation agent were more important than the bulkiness or the R-Si- groups (shaded in blue) in terms of preventing aggregation. When two or more alkoxysilanes were found in the specific silylation agent, such as APTMS and DPDMS, the SNPs did not show any flocculation—not even after 24 h of continuous reaction (Table 4). SNPs treated with bulky agents such as t-bDMMS and DMPES, which each had one alkoxysilane, showed flocculation after 2.5 h reaction time. Thus, the number and the length of the alkoxysilanes in the passivating agent played an essential role in the surface reactivity of the SNPs and, therefore, determined whether or not the particles aggregated.

Since the passivating agent DPDMS did not cause flocculation, it was employed to passivate the "one-pot" SNPs. As expected, the particles generated by this method showed complete monodispersity, indicating the absence of aggregation. The size of these "one-pot" particles was between 25 and 30 nm in diameter, as shown in the TEM micrographs in Figure 57.
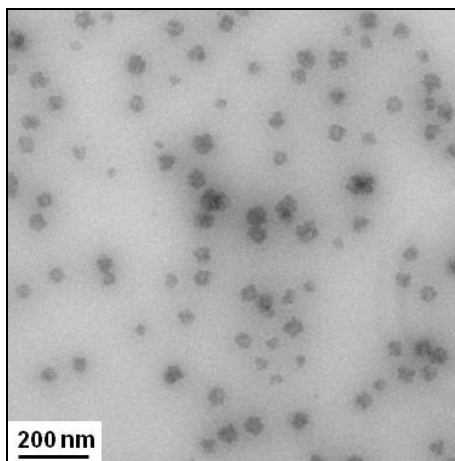
Figure 57. "One-pot" synthesis and passivation of the SNPs with DPDMS. The TEM image shows the efficient passivation of the SNPs with DPDMS, which generated monodispersed SNPs.

The SNPs displayed distinct white centers (indicative of star polymers) as previously demonstrated using the "two-pot" method. Choosing the right silylation agent, then, is important in achieving passivating or activating surface modifications. At the same time, however, the SNPs generated with this method had unusual gray zones surrounding the particles, possibly comprised of unreactive material (see Figure 57). Therefore, cleaning the SNPs was necessary because this material could potentially interfere with chemical reactions on the surface of the particles. The particles were cleaned using the typical method of dialysis with 7 kDa MWCO dialysis bags. Methanol, the first dialysis solvent, did not clean the particles (Figure 58(b)). When the solvent was changed to THF, however, clean particles suitable for further chemical reactions were obtained; the gray zones surrounding the particles were removed, as shown in Figure 58(c). Based on these results, the selection of a suitable dialysis solvent was more important for successfully cleaning the particles than was the size of the pores in the dialysis bags.
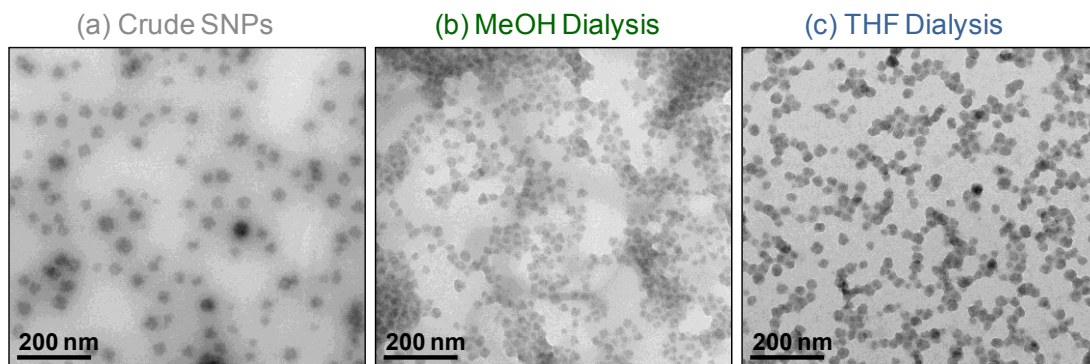
Figure 58. TEM images displaying the effect of dialysis in cleaning the one-pot SNPs. THF dialysis (c) produced cleaner particles compared to MeOH dialysis (b).

Reducing the quantity of reactants is another method of generating cleaner particles; it may be more efficient because typical dialysis procedures take more than 24 h and use large quantities of solvent. The aggregated particles that resulted when the Stöber reaction continued for more than 2 h suggested an excessive amount of TEOS. Ideally, if the optimum amount of the silica precursor were used, the precursor would react completely and silica encapsulation would occur without particle aggregation. Determining the optimum amount of TEOS, however, was time-consuming because of its relatively slow reactivity. TMOS, on the other hand, is a more reactive silica precursor that is quickly consumed; thus, it was easier to determine the optimum amount of reactant. As depicted in Table 5, when 50 µL of TMOS were added progressively to the particles in two 5-min intervals, flocculation was observed. Similar results were observed when TMOS was added in quantities of 20, 20, and 50 µL at three 5-min intervals. When TMOS was reduced to four additions of 10 µL at 5-min intervals, however, only slight cloudiness was observed. This indicated that limiting TMOS addition to 40 µL was an effective means of avoiding substantial aggregation.

Table 5. Progressive addition of TMOS and reactivity in silica encapsulation of star polymers.

	Addition Time				
	5min	5min	5min	5min	Results
Volume	50µL	50µL	-	-	Aggregation
	20µL	20µL	50µL	-	Aggregation
	10µL	10µL	10µL	10µL	Slightly Cloudy

Similar studies were performed when passivating the SNPs. Thirty μL of APDMS successfully passivated the SNPs; after a 24-h reaction period, particles treated with this agent did not show flocculation. Because of this finding, the amount of the silica precursor used was drastically reduced from 150 μL to 40 μL, a reduction of almost 75%; the amount of the passivating agent was reduced by 96% from 800 μL to 30 μL. The templated silica particles were then generated using the "one-pot" approach and applying the modified reagent amounts. Figure 59 illustrates the effectiveness of this strategy, which generated clean particles without adjacent gray zones. Furthermore, the particles were between 25 and 30 nm in diameter, similar to the particle size achieved in the "two-pot" approach, which required a greater amount of reagent.
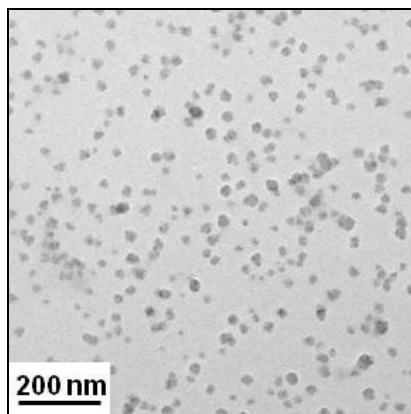
Figure 59. TEM micrograph of cleaner "one-pot" silica nanoparticles obtained by reducing the amounts of the silica precursor and the passivating agent. The monodispersed particles ranged in size between 25 and 30 nm.

These results demonstrated that 30 μL of the silica precursor was sufficient to completely encapsulate the templates with silica. Furthermore, the particles created using smaller quantities of reagents were monodispersed, indicating that the amount of the passivating agent was still enough to prevent the particles from aggregating.

5.2.6   Investigating the Silica Encapsulated Star Polymer

As demonstrated in Section 5.2.1, the location of the occluded dye inside the star polymer was investigated by fluorescence spectroscopy using a dansylated compound. Furthermore, white regions in the middle of the silica nanoparticles shown by the TEM images (Figure 49) indicated a less dense material, which most likely was the star polymer. To determine if the star polymer was enclosed in silica, it was necessary to isolate the templated SNPs into a solid form and take IR spectroscopic data. The spectroscopic results were compared with those of pure solid silica nanoparticles and with those of bare star polymers; elements of both the template and the silica nanoparticles were found. In Figure 60, the signals at 1715.16 cm^{-1} and at 2851.31 cm^{-1} (black and blue curves) indicate the successful formation of both the bare star polymer and the templated SNPs shown by the black and blue arrows. The stretch at 1036.75 cm^{-1} indicates the formation of silica coating on the star polymers.
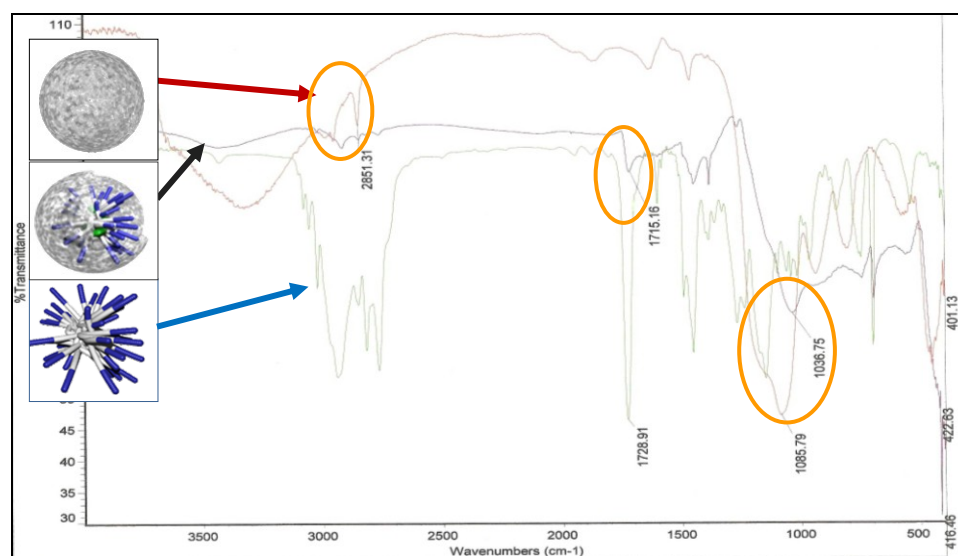
Figure 60. IR spectrum of the solid SNPs (red), templated SNPs (black), and bare star polymers (blue), confirming the existence of silica and template elements on the templated silica nanoparticles.

The IR analysis confirmed that the templated SNPs had elements of the star polymer and the silica particles. A set of controls was studied to determine the effect of the star polymer in the Stöber reaction. A reaction with both the "one-pot" and the "two-pot" methods was performed without the star polymers to investigate the effect of this change. As shown by the TEM image in Figure 61(a), the solid SNPs generated using the "two-pot" method ranged in size from 50-275 nm in diameter, while those generated using the "one-pot" method (c) measured 60-70 nm in diameter. The TEM images in Figure 61(b, d) show that the templated SNPs had a similar size and shape regardless of the method used; the generated templated SNPs displayed white regions in the center that were not present in the solid SNPs.
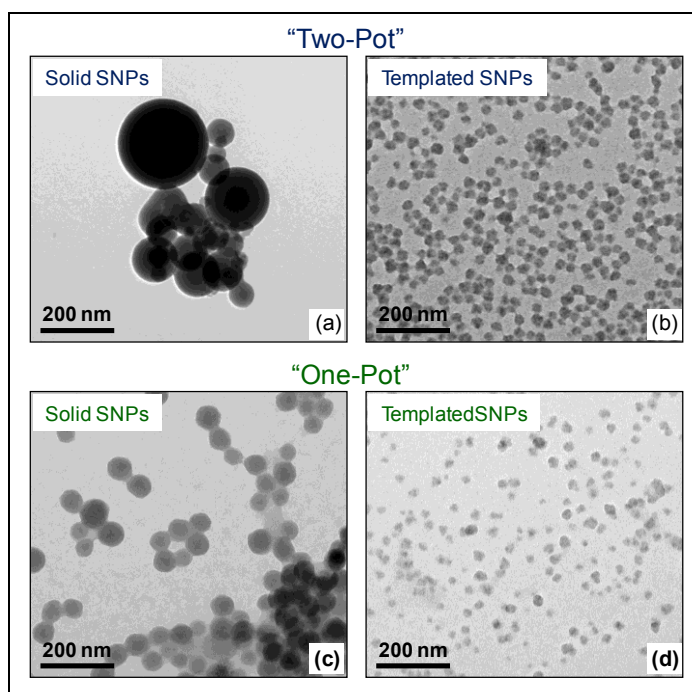
Figure 61. TEM micrographs of solid and templated silica nanoparticles generated using the "two-pot" and "one-pot" methods. Solid "two-pot" SNPs (a) measured between 50 and 275 nm in diameter, and solid "one-pot" SNPs (c) measured between 60 and 80 nm. The templated SNPs (b, d) had similar sizes, between 25 and 30 nm in diameter, regardless of the method used.

Bigger, solid SNPs were generated using the "two-pot" method, which required

more TEOS than did the "one-pot" method. The solid particles that did not contain the

templates were almost perfectly spherical with uniform color throughout the surface

(Figure 61 (a, c)). To verify the composition of the center of the templated SNPs,

elemental analysis of the particles was performed by electron energy loss spectroscopy

(EELS). The particles were first coated with an iron cap and milled with a focused ion

beam to expose the inside of the particles. The TEM micrograph in Figure 62 depicts

two milled particles that contained multiple star polymers.
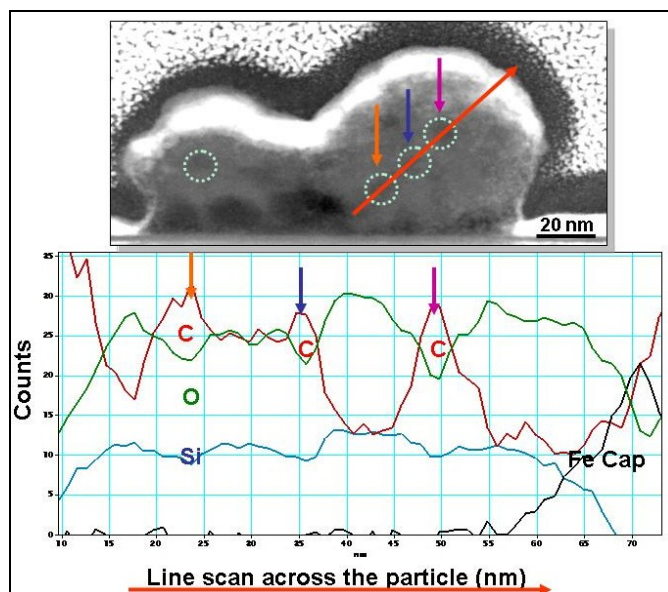
Figure 62. Elemental analysis of the templated SNPs by EELS. The center of the
particles contained carbon-based material.

The EELS graph and the TEM image in Figure 62 show the results of the line

scan through three star polymers inside a 70 nm SNP. The red curve shows the carbon

content; the green curve, the oxygen; and the blue curve, the silica content. As the beam

scanned through the star polymers (see arrows), the carbon counts increased, while the oxygen and the silica counts decreased. This analysis proved that the material inside the templated SNPs undoubtedly consisted of carbon-based star polymers. The results obtained by IR spectroscopy demonstrated the existence of star polymer elements and silica on the templated SNPs. The EELS analysis proved that the carbon-based star polymers were indeed encapsulated with silica.

5.2.7   Surface Transformations of Templated Silica Nanoparticles

It was previously demonstrated that the surface of the SNPs was transformed from reactive silanol to passivated diphenyl with the silylation agent DPDMS (Section 5.2.6). Controlling the reactivity of the peripheries was necessary to couple desired material onto the surface of the nanoparticles for specific applications. The silanol surface was accessible, but in order to make other types of chemical changes, an even more accessible surface was needed. An aminated surface, with its versatility and accessibility to different types of chemistry, was optimal. APTMS was used as the organosilane amino precursor. A batch of particles was produced using the "one-pot" process and split into two groups. Half of the particles were deactivated by the addition of DPDMS, and the other half were activated by the addition of APTMS. As shown in the TEM image in Figure 63(a), the deactivated particles coated with the bulky passivating diphenyls showed great dispersity. However, the surface amino-activated particles shown in Figure 63(b) stuck to each other. This study demonstrated that the surface of the SNPs was addressable with desired functional groups.
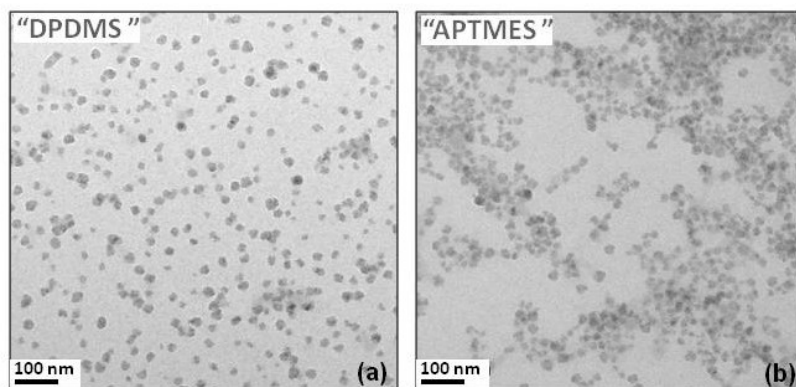
Figure 63. TEM micrographs depicting the silanol surface transformations. The particles were deactivated (passivation) with DPDMS (a) or amino-activated with APTMES (b). The surface-transformed SNPs were generated using the "one-pot" process.

In order to determine if the introduced functionality was addressable or if the amino groups were available for further chemical reactions, the reactivity of the surface amino groups was tested by examining their responsiveness to dansyl chloride. The particles generated by the "one-pot" method were treated with functional organosilanes, with APTMS to generate aminated SNPs and DPDMS to generate passivated SNPs prior to dansylation. Dansyl chloride reacts mainly with the amino groups; it should also react to some degree with external silanols, but it should not react with the passivated diphenyl SNPs. The crude silanol particles, the amino activated SNPs, and the passivated SNPs were treated with dansyl chloride. Any remaining unreacted dansyl chloride was removed by methanol dialysis. The UV-vis absorption spectrum generated by these dansylated SNPs was compared with those generated using a dansyl sulfonamide model and unreacted dansyl chloride. In Figure 64, the green curve represents the aminated SNPs prior to dansylation. The aminated SNPs reacted readily with dansyl chloride (orange curve); the signature absorbance peak is almost superimposed on that of the

sulfonamide model peak (orange dotted curve), showing compatible absorption curves.

The crude dansylated silanol sample, with a low dansyl absorbance peak at 325 nm (red

curve), displayed a lower reactivity to dansyl chloride. The absorbance values of the

mentioned particles were normalized to the constant porphyrin peak at 419 nm, showing

the relative reactivity of the surface functionality to dansyl chloride. The dansylated

passivated diphenyl SNPs (blue curve) did not react with dansyl chloride; therefore, the

dansyl signature peak is not seen in these specific SNPs, which did not contain porphyrin

(Figure 64).
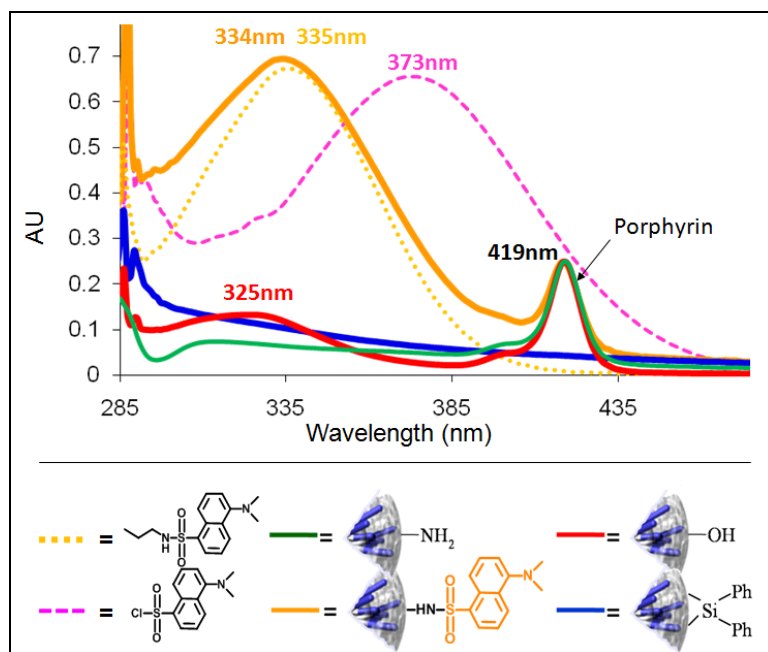
Figure 64. UV analysis of periphery functionalized "one-pot" SNPs with dansyl chloride.
The UV graph compares the dansylated amino SNPs with dansyl chloride and with the
sulfonamide model and reveals that amino addressability is possible.

This study was performed to confirm that amines, not just silanols, reacted with

dansyl chloride because amines were to be used for further chemical reactions.

Furthermore, the surface-modified particles were observed in the TEM and SEM

micrographs (Figure 65). When the SNPs were coated with the bulk passivating agent
DPDMS (a), the particles tended to disperse. When the particles were coated with amino
groups (b), the activated particles coagulated. Once the aminated particles were
dansylated, the particles redispersed evenly (c). These studies demonstrated that the
surface of silanol nanoparticles could be successfully transformed into addressable
aminated surfaces.
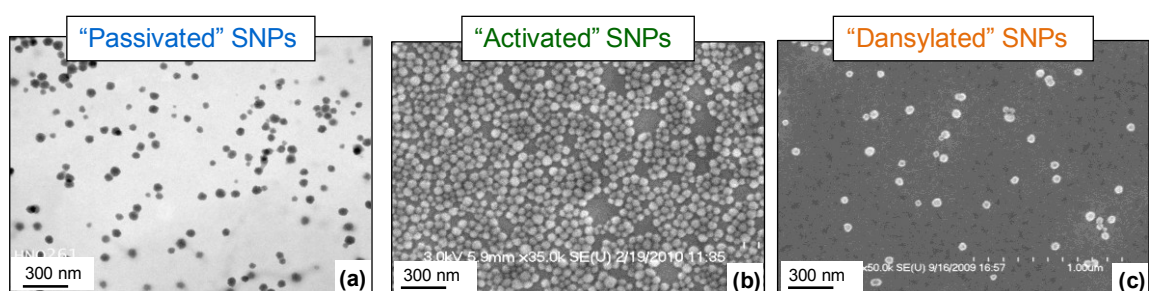
Figure 65. SEM and TEM images of the surface transformed "one-pot" SNPs. TEM
image (a) shows the passivated SNPs; the SEM image (b) shows the aminated SNPs; and
the SEM image (c) shows the dansylated SNPs.

5.2.8 Varying the Size of the Silica Nanoparticles

Having control over the size of silica particles in the nanoscale range increases
their potential applications, such as imaging or drug delivery [28]. It is very important to
develop the ability to generate particles of different sizes, as the size of the particles
affects cell penetration and particle excretion [37]. Experiments were conducted to
develop techniques for particle size control. The three major techniques that emerged
were fine-tuning the particle reaction time, varying the size of the template, and varying
the TMOS concentration. The first technique studied was reaction time; therefore, a
timeline displaying a range of different sizes of templated SNPs was produced (Figure
52). In the TEM images in Figure 66 (left panel top to bottom), two different reaction

times are depicted, 30 and 90-min, with particle diameters of 18 nm and 30 nm, respectively. With increasing reaction time, larger particles were obtained. The next set of studies in size control was performed by changing the size of the star polymer. Two different templates with arm sizes 9.0 and 11.0 kDa were used for this study. Both of the templates were exposed to the same reaction conditions. The particles produced had an average diameter of 20 nm and 35 nm respectively, as seen in the TEM micrographs in Figure 66 (middle panels). Changing the concentration of the silica precursor was also investigated as a method of particle size control. The SEM images in Figure 66 (right panel) reveal particles of 25 nm in size when 7 µL of TMOS were used and 40 nm in size when 30 µL of TMOS were used. When the concentration of the silica precursor increased, larger SNPs were obtained.
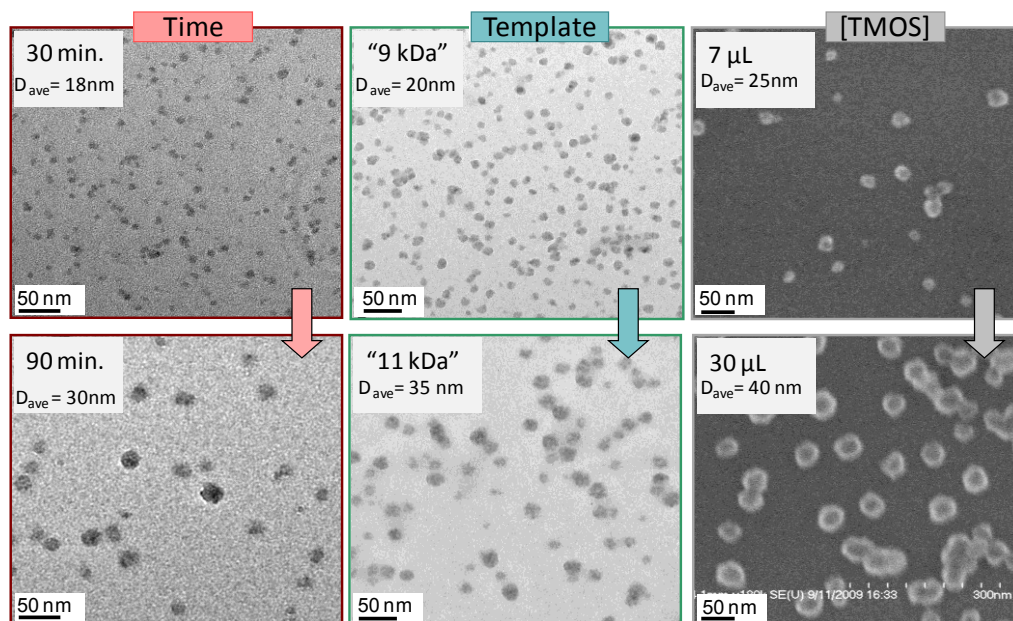
Figure 66. Size control of templated SNPs was achieved by changing three parameters: reaction time (left TEM images) using 30-min and 90-min intervals; template arm size (middle TEM images) using 9.0 kDa and 11 kDa; and TMOS loading (right SEM images) using 7 µl and 30 µl, respectively.

Based on the results, it is possible to reliably generate particles of different sizes. Larger particles were obtained with longer reaction times, bigger templates, and increased reagent concentration. The flexibility of generating nanoparticles at any requested size was tested using the above techniques. Particles were generated with targeted diameters of 25, 50, 75, and 100 nm to reproduce the viability of the methods. The modified experimental conditions were suitable for larger particle production and were modified for each target size. The results are shown in Figure 67. The ability to generate templated SNPs of different sizes was verified, demonstrating that the techniques used to control the size of the particles were viable.
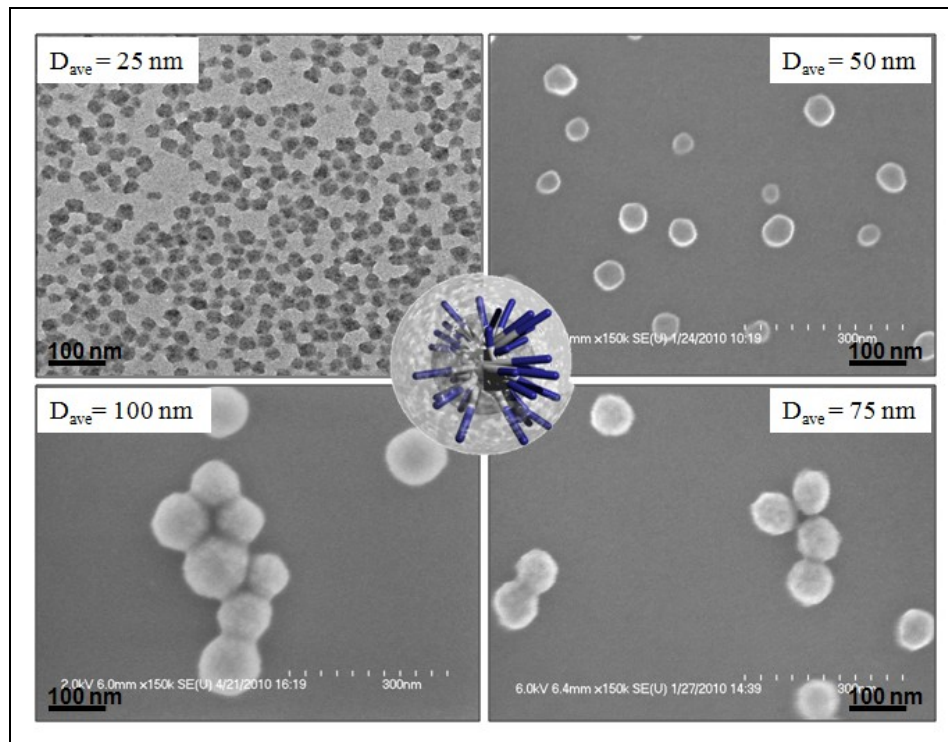
Figure 67. SEM and TEM images showing the ability of the size control method to generate size-targeted SNPs. TEM image shows the targeted 25 nm particle; the SEM images show the targeted 50, 75, and 100 nm SNPs.

5.2.9   Cargo Release and Shell Thickness

Being able to control the retention and release of the particle material is important for specific applications. If the particles are used as imaging agents, it is necessary to load as much dye as possible inside the particles without any bleeding occurring over time. If the particles are used as vehicles to release the material into a specific target tissue, a mechanism has to be developed to control the release of the material. In the interest of better understanding how to control cargo release, a dye-retention was performed to monitor how well the dye-occluded SNPs retained the dye during THF dialysis. Porphyrin-occluded SNPs measuring an average of 30 nm in diameter were generated using the "one-pot" method. Since the hydrophobic cargo is soluble in THF, the SNPs containing the hydrophobic cargo were exposed to THF dialysis. As a result, the forces that kept the cargo inside the particles were removed. If there were an opportunity for the dye to come through the silica shell, it would be able to diffuse out of the SNPs during THF dialysis. Consequently, the particles were dialyzed against THF, and the solvent was changed every 12-16 h. An aliquot of the particle solution was collected after 6 h to be analyzed by UV-vis spectroscopy; this sample was compared to an aliquot taken after 72 h. As shown in Figure 68, the silica shell was thick enough to effectively retain the dye inside the SNPs, even after 72 h (blue curve). This demonstrated that the silica shell could successfully retain the cargo inside the silica nanoparticles. However, because the silica matrix was porous and permeable to small molecules, it was necessary to find the minimum silica shell thickness that allowed the material to be released when exposed to an organic solvent.

107
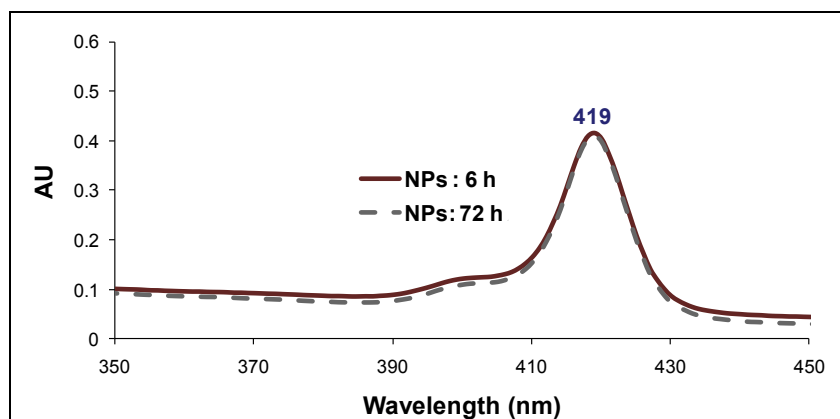
Figure 68. Absorption spectra of the retained porphyrin inside the occluded SNPs when exposed to THF dialysis for 72 h. Porphyrin was successfully retained inside the SNPs during prolonged THF dialysis.

Two sizes of porphyrin-occluded SNPs were synthesized to generate SNPs of different shell thickness. After the particles were aminated and dansylated, both particles were dialyzed against methanol for 24 h to remove all the unreacted material. Both of the particles were then exposed to THF dialysis for 24 h, and the solvent was changed every 8-12 h. The particles were removed from the dialysis bags and the UV absorbance of the dialyzed particles was measured. As shown in Figure 69, the TEM micrographs on the right show that the larger particles were about 30 nm in diameter (top) and the smaller particles were about 20 nm in diameter (bottom). The absorbance of both of these porphyrin-occluded SNPs was normalized to the constant dansyl absorption peak at 334 nm. The porphyrin peak at 419 nm (dashed red curve) in Figure 69 stayed constant for the bigger particles after 24 h of THF dialysis (blue curve); for the smaller particles with a thinner silica shell, the peak diminished after 24 h (green curve). The results in Figure 69 demonstrate that the thickness of the shell was the overriding factor in controlling the release of the cargo inside the porphyrin-occluded SNPs.
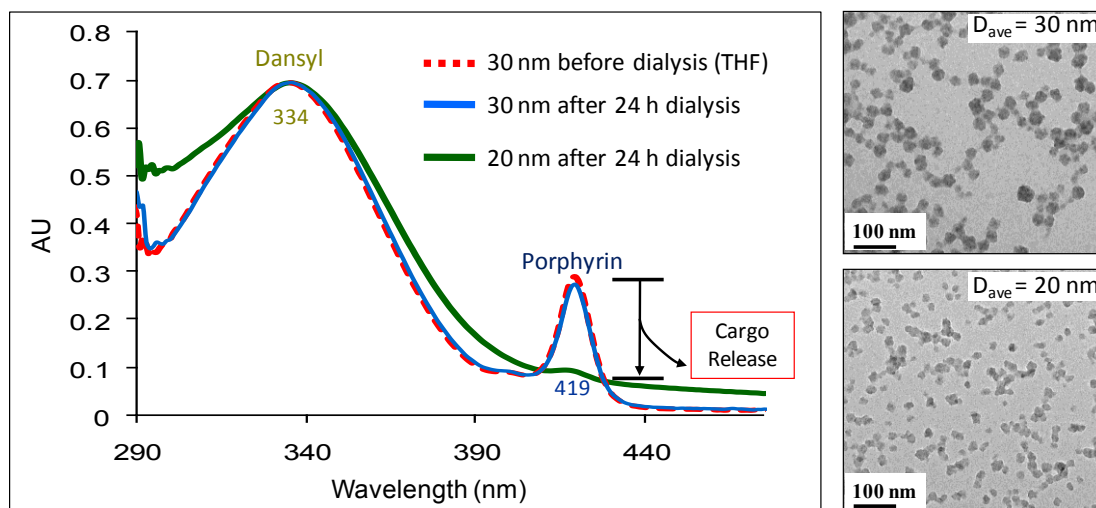
Figure 69. Cargo release in relationship to the silica shell thickness of the SNPs. TEM micrograph with the 20 nm diameter SNPs shows that the dye was released through the thin shell (green curve). The TEM micrograph with the 30 nm diameter SNPs reveals that the thicker shell prevented the dye from bleeding out (blue curve).

5.2.10 Biocompatibility of Silica Nanoparticles

The functionalized silica nanoparticles synthesized using the Stöber method were highly soluble in organic solvents. If the particles are to be used in drug delivery or cell targeting, they must be water-soluble. Previously, it was demonstrated that the amino groups of the APTMS-functionalized SNPs were addressable. Therefore, water solubility of the particles can be enhanced by introducing a PEG periphery; this is accomplished by coupling PEG molecules to the surface amino groups. PEG is a nontoxic, water-soluble material that, when added as a coating, is ideal for adding biocompatibility to the SNPs. The PEGylation reaction was performed after the solvent of the aminated SNPs was exchanged for toluene, and 100 mg of NHS-PEG (5 kDa) and 0.50 mL TEA were added. Figure 70 shows SEM micrographs of the 32 nm silanol SNPs (a), the 38 nm aminated SNPs (b), and the 45 nm PEGylated SNPs (c).
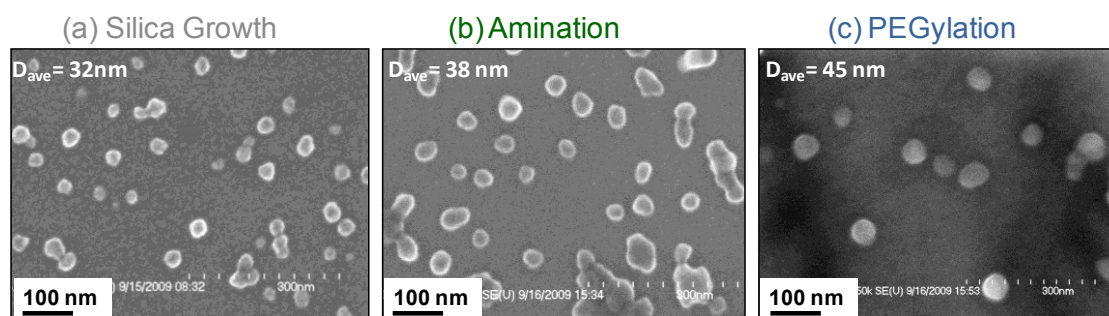
Figure 70. PEGylation of the aminated SNPs in toluene and TEA. The particles, as shown by the SEM micrographs, slightly increased in size with subsequent added functionality from silanol (a) SNPs to aminated (b) SNPs and to PEGylated (c) SNPs.

The SEM images of the crude PEGylated SNPs (c) revealed a fuzzy material surrounding the particles. Initially, this halo was thought to be related to unreacted material, so dialysis was performed with large 25 kDa MWCO dialysis bags; it was unsuccessful. Perhaps the fuzziness surrounding the particles was just an imaging effect generated from the moisture attracted by the highly hydrophilic PEG chains. Since the curing temperature for the non-PEGylated particles was 110 °C, for the PEGylated SNPs the temperature was increased to eliminate traces of moisture. A sample was spun coated on a silica wafer and broken into four pieces to be exposed to different temperatures. Each piece was cured for 1 min at a variety of temperatures in 20 °C increments, starting at 120 °C. As shown in Figure 71, the evident cloudiness shown in the 120 °C SEM micrograph vanished as the curing temperature increased. The cloudiness disappeared when the curing temperature reached 200 °C, confirming the prediction that the initial cloudiness was due to moisture.
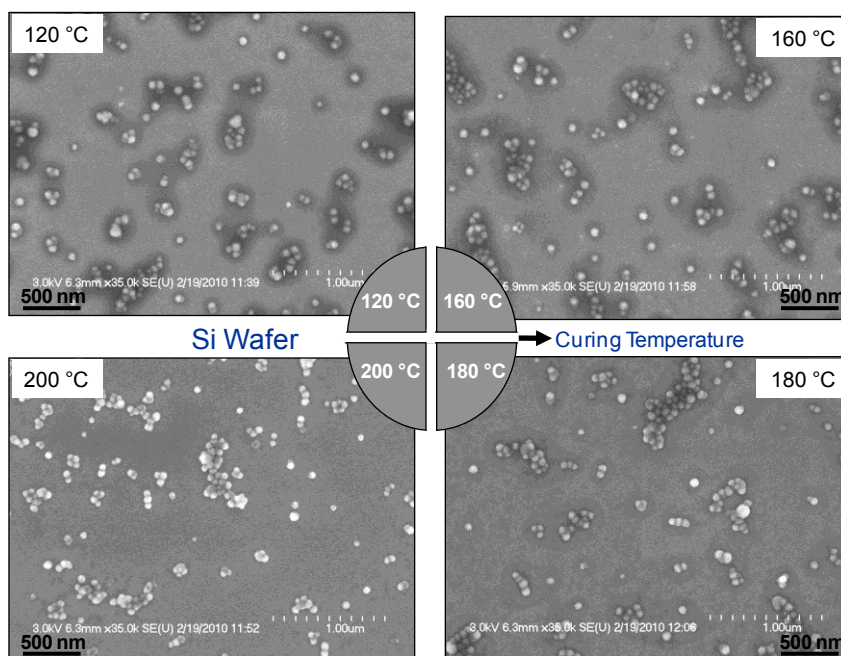
Figure 71. Scanning electron micrographs showing the effect of the curing temperature on the crude PEGylated SNPs. Higher temperatures provided clearer images due to the dryness of the samples.

The crude PEGylated SNPs were ready to be tested for water solubility. Initially, methanol dialysis was performed with 50 kDa MWCO dialysis bags to completely remove all the toluene and any unreacted materials. As seen in Figure 72 (b), the PEGylated particles were exceptionally water-soluble, producing a clear solution with a faint red color provided by the occluded dye. In contrast, the aminated particles (a) formed a whitish suspension, which was an indication of the instability of the amino functionalized particles in water. However, the SEM micrographs showed ambiguous material (c) containing apparent clumps of particles with large amounts of surrounding residual material. Since the crude PEGylated particles could be imaged and analyzed by SEM, it did not make sense for these cleaned water-soluble particles to contain unidentifiable material.

111
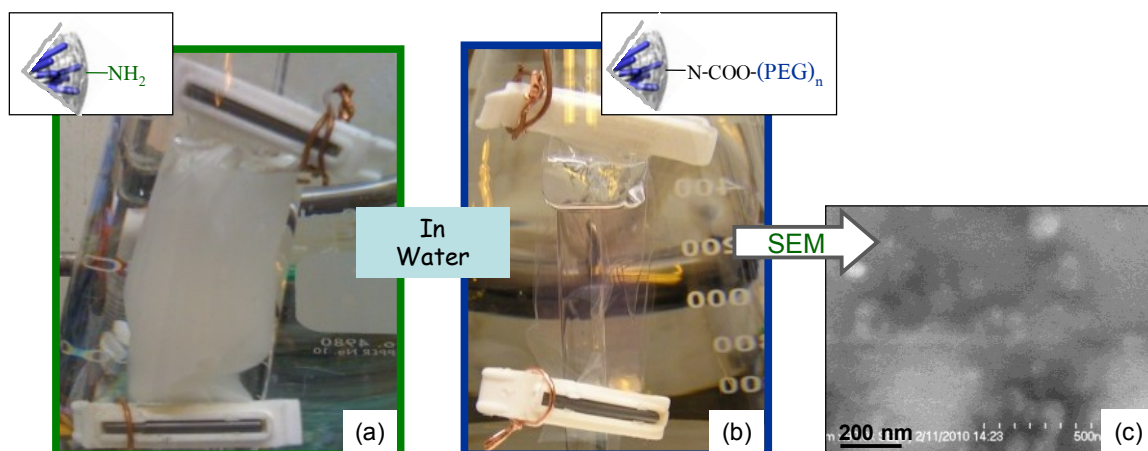
Figure 72. Particle stability in water of PEGylated SNPs. Aminated SNPs (a) formed a cloudy suspension in water; after PEGylation, a translucent solution (b) was obtained. SEM images (c) showed that characterization was inconclusive; PEGylated SNPs could not be imaged.

The amount of the starting material was first investigated to resolve the discrepancy. Molar amounts of APTMS and PEG were used to minimize unreactive material. The particles were aminated, PEGylated, cleaned by dialysis using methanol, and finally exposed to water. The particles were highly soluble in water, but the problem persisted; viewing the particle was still not possible. Increasing the size of the dialysis bags did not solve the problem.

The PEGylated particles were analyzed through the dialysis process at each step to obtain a better understanding of the problem and to ensure that the particles were present inside the dialysis bag. Another batch of PEGylated particles was generated and dialyzed against methanol to remove toluene. An aliquot of these particles in methanol prior to water dialysis was obtained and analyzed by SEM. The particles could not be found, but something unusual was observed: previously unseen micron size objects without a definite shape. In all likelihood, toluene had a detrimental effect on the dialysis

bags, and the unidentified material masked the particles. Therefore, a new approach to PEGylate the particles was employed.

Section 5.1.7 demonstrated that the aminated SPR substrates were successfully PEGylated when the PEGylation was done in DCM. This approach was an attractive alternative to attack the problem, and a new experimental method using DCM was implemented to PEGylate the particles and avoid the use of toluene. After the particles were synthesized and amino functionalized using the "one-pot" method, they were dialyzed in DCM. The solvent was exchanged every 8-12 h, and the particles were removed from the dialysis after 24 h. During DCM dialysis, ethanol, ammonia, and unreactive organosilanes were removed, and cleaned SNPs in DCM were obtained. NHS-PEG (750 Da) and TEA were added in the same amounts as in the previously described example, and the reaction continued for 24 h while the mixture was stirred. The particles were dialyzed against methanol to remove dichloromethane (DCM) and dialyzed against water to test for water solubility. The cleaned PEGylated particles were spin-coated on a UV-ozone treated silica wafer and viewed using SEM. The newly established experimental conditions eliminated the problem encountered when PEGylation was performed under toluene; no clumps of particles or extraneous matter were visible surrounding the particles. As shown in Figure 73, the silanol SNPs (a) were aminated and showed the usual stickiness due to the surface amino groups (b). Once PEGylation was performed in DCM, the particles redispersed evenly in water (Figure 73 (c)). The new experimental conditions allowed characterization of the PEGylated SNPs, and the SEM micrographs revealed uniform, monodispersed, and clean PEGylated SNPs.
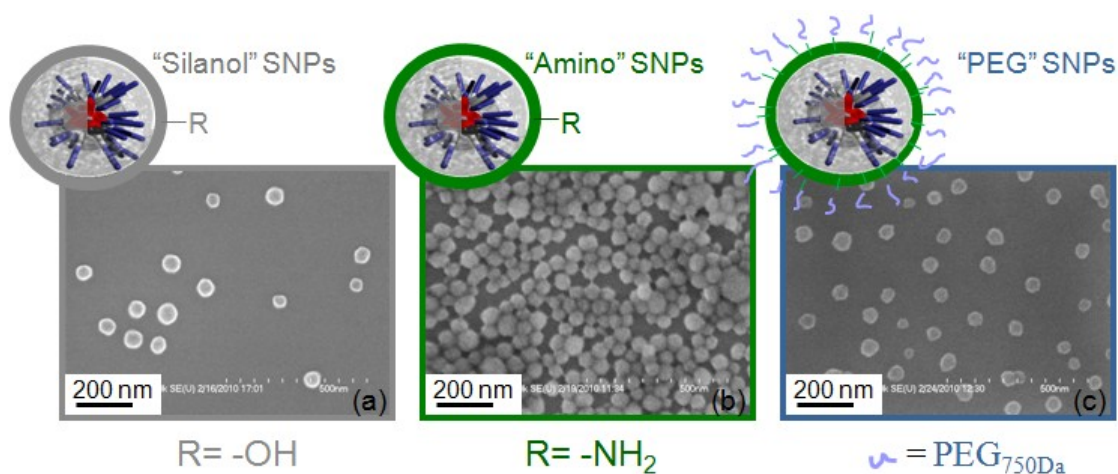
Figure 73. SEM images of the PEGylated SNPs using the modified reaction over DCM/TEA. The silanol SNPs (a) were aminated (b) and the PEGylation reaction in DCM/TEA generated PEGylated particles (c) with excellent monodispersity and water solubility.

The size of the PEGylated particles was obtained by DLS in water, and UV-vis spectroscopy was used to measure the absorbance of the hydrophobic dye in water. Figure 74 shows the scheme (a) of the alternative method to PEGylate the particles in DCM/TEA. Furthermore, the optical images of the PEGylated particles in water (b-middle vial) show the excellent water solubility of the PEGylated particles compared to the insoluble amino particles in water (b-left vial). Figure 74(b-middle vial) shows that the PEGylated particles had a faint color produced by the occluded dye. This allowed the recording of UV-vis absorbance measurements of the hydrophobic dye occluded inside the PEGylated particles in water; the measurements were compared to pure porphyrin in THF. Figure 74 (c) shows the absorbance of the solvatochromic dye when it was occluded inside the PEGylated SNPs (red curve) and when it was dissolved in THF (dotted purple curve). The absorbance peak shifted four nanometers to the right due to the solvent effects on the dye. DLS measurements were performed to find the

114

hydrodynamic radius of the PEGylated particles in water; in this case, the particles were 60 nm in diameter (d). PEGylation of the aminated SNPs was plausible, providing water-soluble dye-occluded SNPs with excellent monodispersity.
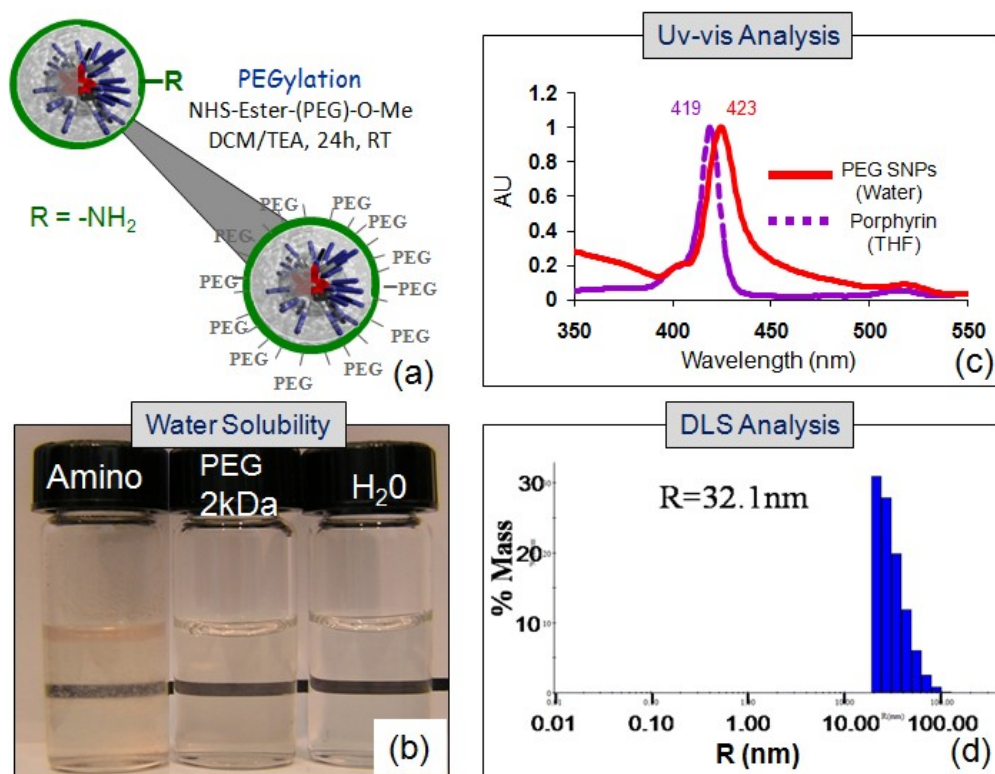
Figure 74. Water solubility, UV-vis analysis, and DLS analysis of the PEGylated SNPs in water. PEGylation scheme of amino coated SNPs in DCM (a) generated water-soluble porphyrin occluded SNPs (b), capable of producing a porphyrin absorbance signal (c) and DLS measurements in water (d).

In the previous PEGylation experiments, the amounts of PEG material were sufficient to solubilize the particles. However, it was necessary to investigate whether all the surface amino groups were completely reacted at the end of the PEGylation reaction. An experiment to synthesize PEGylated particles using different lengths of PEGs was conducted. The PEGylated particles were then exposed to dansyl chloride to determine any available addressable amino groups. Four different lengths of PEG were used: 750

Da, 2 kDa, 5 kDa, and 10 kDa. Once the particles were PEGylated by the DCM/TEA

approach, they were exposed to dansyl chloride. The particles were cleaned with

methanol dialysis, and the solvent was exchanged using water dialysis. The dansylated

PEGylated SNPs in water were analyzed by UV-vis spectroscopy. As shown in Figure

75, for the short 750 Da-PEG (red curve), there was no activity in the dansyl area after

exposure to dansyl chloride. When dansylation was performed on the 2 kDa-PEG

particles (green curve), a moderately strong dansyl signal appeared). As PEG length

increased, more dansyl material was installed on the surface of the 5 kDa (blue curve)

and 10 kDa-PEG (black curve), as depicted in Figure 75.
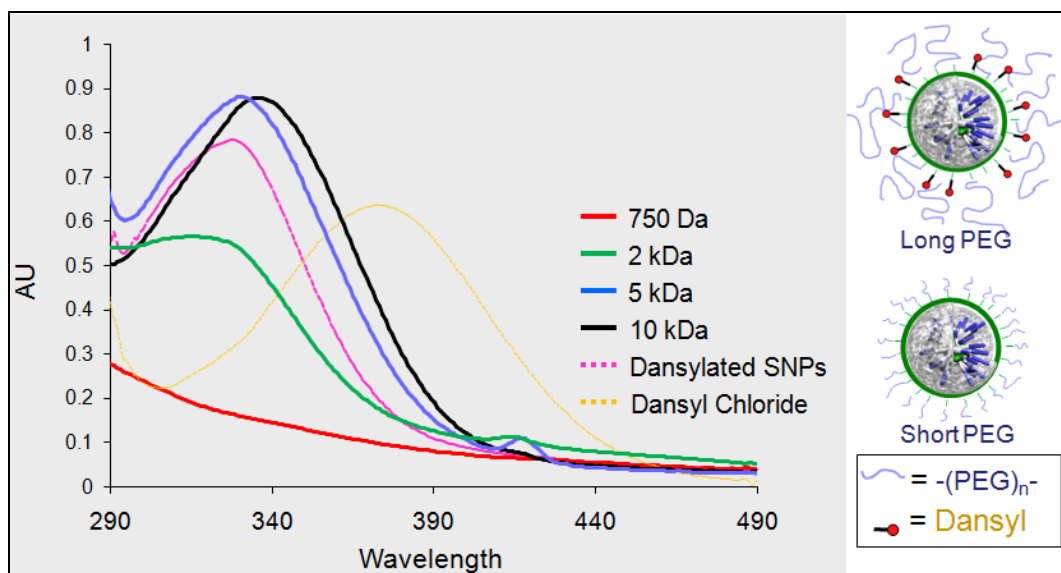
Figure 75. UV-vis analysis on the dansylated PEG-SNPs. The absorbance of the
particles in water demonstrates that amino groups were addressable after the particles
were treated with the long PEG, but were not addressable when treated with the short
PEG.

These observations indicated that dansylation of the PEGylated SNPs was

possible when the PEG was long. When a long PEG was used, it sterically blocked

residual amines from reacting with other larger PEG polymers, but left enough PEG

material to provide water solubility. When a small PEG was used, amines became

available for other small PEGs to react with all the available amines; as a result, there

was no potential reactant for dansyl chloride. The scheme in Figure 75 (right) shows how

the amines were sterically blocked when longer PEGs were used and how the amines

reacted when smaller PEGs were used. Thus, while PEG is good for biocompatibility, it

allows targeting agents to be included around the peripheries. These agents can be used

in cellular recognition studies.

CHAPTER SIX
CONCLUSIONS

Two different techniques applicable to biotechnology were developed employing silica-based materials, one using plasmonic 2D biosensors, and the other using discrete 3D templated silica nanoparticles.

The SPR substrates for the biosensor studies were constructed by PVD. Three nm of Cr was deposited onto SF-11 substrates as an adhesion layer, 50 nm of gold as the plasmonic source, and 4 nm of SiO_2 as a protective layer. The uniformity of the gold deposition was analyzed by SPR in prepared substrates; the plasmonic responses were uniform, indicative of a homogeneous deposition. The SPR substrates were successfully nanostructured using an organosilicate solution in combination with a polymer porogen. The organosilicate solution contained either a star polymer with a polystyrene core and a PEO periphery, or a diblock copolymer with a polystyrene end and a PEO end. Upon curing, the organosilicate cross-linked, and random porosity was generated when the star polymer was used. When the block copolymer was used, an ordered array of pores was generated through self-assembly. These two physical features on the SPR substrates were compared with a planar surface generated when the organosilicate solution without polymers was thermally cured.

Activation of the substrate surface was achieved by UV-ozone treatment to liberate cross-linked silanol groups. Previous studies to aminate the activated surface used vapor deposition of APTMS. In this study, a solution-based approach was used to successfully aminate the activated surface with APTMS. One of the main objectives of

this study was to generate a nonfouling surface. To this end, the surface of the particles was transformed with the antifouling agent PEG. The transformation was done over DCM/TEA with NHS-(PEG)$_7$-OMe, which specifically reacted with the primary amines on the SPR substrate. The antifouling properties of the PEGylated surface were successfully tested with a solution of the protein bovine serum albumin in phosphate-buffered saline and compared to an aminated surface that did not contain the antifouling background. The protein adsorbed irreversibly to the aminated surface but not to the PEGylated surface, indicating the successful construction of an antifouling surface that contained random or order porosity features.

In the case of the 3D nanoparticles, a star polymer occlusion complex was successfully prepared for use as a template for silica deposition. The dye was occluded inside the hydrophobic core of the star polymer by molecular self-assembly. The location of the dye was confirmed by fluorescence spectroscopy on the dansyl butanol ester located within the core. An experimental methodology was developed to coat the dye-occluded star polymer complex with silica by the "two-pot" method. The generated particles were characterized by AFM, TEM, and SEM. The "two-pot" method was effectively modified into a simpler method known as the "one-pot" method, which utilized less reagent and significantly reduced the handling time of the particles. Visually inspecting TEM images of the templated SNPs confirmed that the star polymers were coated with silica. These particles had a distinct white center in the middle, indicating a less dense material than that found in the solid untemplated particles. The existence of

the carbon-based star polymer inside the templated SNPs was confirmed by IR spectroscopy, by comparison to controls, and by EELS analysis.

The surface of the particles was successfully functionalized either in a passivated form with the bulk silylation agent DPDMS or in an activated form with the amino precursor APTMS. The surface functionality of the particles was tested using UV-vis spectroscopy by exposing dansyl chloride to the functionalized particles. The absorbance of the dansylated particles confirmed the existence of amino groups on the surface of the particles.

The size of the particles was controlled by changing the reaction time, the size of the template, and the concentration of reagents. Using these strategies, particle diameters could be varied from 20-100 nm. Controlling the size also allowed control of the shell thickness, which affected the diffusivity of the cargo. The shell thickness was the key factor that determined whether or not the cargo was released.

Biocompatibility of the particles was achieved by coupling the biocompatible PEG molecule with the surface amines. Highly cleaned water-soluble discrete particles were obtained, and the addressability of any residual amines was successfully tested using dansyl chloride after the particles were PEGylated. If a long PEG was used, the bulkiness of the PEG sterically blocked other long PEG from reacting with the amines, but when a short PEG was used, there were no free amines for further reaction. This allowed targeting agents to be installed on the surface of the PEGylated particles even as water solubility was retained.

CHAPTER SEVEN
CURRENT AND FUTURE WORK

Methods to construct SPR substrates with an organosilicate layer with added physical morphology and functionality are powerful tools in the early detection of specific disease-causing agents or disease bioproducts at very low concentrations. These biosensors are ideal tools for early diagnoses because of the high sensitivity and selectivity of the surfaces. Additional experiments must be performed, however, to develop optimum optical instrumentation and noise reduction.

In the studies described here, the surfaces of the SPR substrates were rendered anti-fouling using PEG with added physical morphology. A method for stalling specific bio-receptors was devised. The surface of the SPR substrates is currently being adapted for specific detection of biological substances such as antibody-antigen, enzyme-substrate, and receptor-ligand models. One of the models currently being studied is the receptor-ligand pair biotin and streptavidin. Tests must be performed to analyze size selectivity in conjunction with chemo-selectivity of the porous biosensors; proteins of different sizes can be used to analyze the ability of the biosensor to screen out larger unwanted proteins. Furthermore, larger sacrificial star polymers are currently being synthesized to nanostructure the surface of the sensor with larger pores. They will be able to target biomolecules of different sizes by nanoengineering the surface accordingly.

Another planned phase of this work is to target specific potential biomarkers using antibody and protein pairs; one such biomarker is the activated leukocyte cell adhesion molecule (ALCAM), a reliable breast cancer marker [78]. The detection limits

of the SPR biosensors must be assessed and compared with current SPR biosensors that utilize only chemo-selectivity.

The core-shell dye-occluded silica particles are of great interest in the biomedical field for their extraordinary potential. The particles could be used as cellular targeting agents, drug delivery vehicles, biocompatible magnetic materials, and image-enhancing agents. It is possible to make a cargo-occluded star polymer encapsulated in a silica shell, complete with installed functionality, to make the particles biocompatible. Currently, methods to isolate the water-soluble PEGylated nanoparticles into a resuspendable powder form have been developed. This would allow the particles to be resuspended in desired biological solutions with specific concentrations relevant to biological applications.

The next planned phase of this work is to expose the dye-occluded PEGylated SNPs to a specific cell line to investigate the toxicity, intake, and fluorescence of the particles inside the cells. So far, solvatochromic fluorescent dyes have been used as the cargo to track the location of particles as well as their surface functionality when the dyes were used as surface tags. Eventually, pharmaceuticals need to be used as the cargo in conjunction with fluorescent surface tags to build multifunctional drug delivery vehicles that can be tracked by fluorescence microscopy.

REFERENCES

1. J. Homola, S.Y. Sinclair and G. Gauglitz, *"Surface plasmon resonance sensors: Review,"* Sens. Actuators, B, **54**, 3-15 (1999).

2. Y. Piao, A. Burns, J. Kim, U. Wiesner and T. Hyeon, *"Design and fabrication of silica-based nanostructured particle systems for nanomedicine applications,"* Adv. Funct. Mater., **18**, 1-14 (2008).

3. W. Tan, K. Wang, X. He, X.J. Zhao, T. Drake, L. Wang and R.P. Bagwe, *"Bionanotechnology based on silica nanoparticles,"* Med. Res. Rev., **24**, 621-638 (2004).

4. P. Torreri, M. Ceccarini, P. Macioce and T.C. Petrucci, *"Bimolecular interactions by surface plasmon resonance technology,"* Ann. Ist. Super. Sanita, **41**, 437-441 (2005).

5. H. Ow, D.R. Larson, M. Srivastava, B.A. Baird, W.W. Webb and U. Wiesner, *"Bright and stable core-shell fluorescent silica nanoparticles,"* Nano Lett., **5**, 114-117 (2005).

6. J. Melendez, R. Carr, D.U. Bartholomew, K. Kukanskis, J. Elkind, S. Yee, C. Furlong and R. Woodbury, *"A commercial solution for surface plasmon sensing,"* Sens. Actuators, B, **35-36**, 212-216 (1996).

7. J. Homola, *"Surface plasmon resonance sensors for detection of chemicals and biological species,"* Chem. Rev., **108**, 462-493 (2008).

8. SPR History. Surface Plasmon Resonance [Online]. Available at http://www.sprpages.n1/SPRtheory/SprHistory01.thm#ref14 (accessed September 18, 2008).

9. P. Englebienne, A.V. Hoonacker and M. Verhas, *"Surface plasmon resonance: Principles methods and applications in biomedical sciences,"* Spectrosc., **17**, 255-273 (2003).

10. B. Liedberg, C.Nylander and I. Lundstrom, *"Biosensing with surface plasmon resonance-how it all started,"* Biosen. & Bioelectron., **10**, i-ix (1995).

11. Total Internal Reflection Hyperphysics [Online]. Available at http://hyperphysics.phy-astr.gsu.edu/Hbase/phyopt/totint.html (accessed September, 18, 2008).

12.   I.D. Alves, C.K. Park and V.J. Hruby, *"Plasmon resonance methods in GPCR signaling and other membrane events,"* Curr. Protein Pept. Sc., **6**, 293-312 (2005).

13.   A. Ramanavieius, F.W. Herberg, S. Hutschenreiter, B. Zimmermann, I. Lapenaite, A. Kausaite, A. Finkelsteinas and A. Ramanayieiene, *"Biomedical application of surface plasmon resonance biosensors,"* Acta Med. Litu., **12**, 1-9 (2005).

14.   M.A. Cooper, *"Optical biosensors in drug discovery,"* Nature, **1**, 515-528 (2002).

15.   J.C Love, L.A Estroff, J.K. Kriebel, R.G. Nuzzo and G.M. Whitesides, *"Self-assembled monolayers of thiolates on metals as a form of nanotechnology,"* Chem. Rev., **105**, 1103-1169 (2005).

16.   J. Lahiri, L. Issacs, J. Tien and G.M. Whitesides, *"A strategy for the generation of surfaces presenting ligands for studies of binding based on an active ester as a common reactive intermediate: A surface plasmon resonance study,"* Anal. Chem., **71**, 777-790 (1999).

17.   R. K. Iler, <u>The colloid chemistry of silica and silicates</u>, (Cornell University Press, New York, 1955), pp. 3-120.

18.   L.L. Hench and J.K West, *"The sol-gel process,"* Chem. Rev., **90**, 33-72 (1990).

19.   E.M. Rabinovich, <u>Sol gel processing-general principles</u>, (Kluwer Academic Publishers, 1994), pp. 2-30.

20.   G. Kolbe, *"Das komplexchemische verhalten der kieselsaure,"* Dissertation, University of Jena, 1956 (1956).

21.   W. Stober, A. Fink and E. Bohn, *"Controlled growth of monodisperse silica spheres in the micron zise range,"* J. Colloid. Interface. Sci., **26**, 62-69 (1968).

22.   G.H. Bogush, M.A. Tracy and C.F. Zukoski, *"Preparation of monodisperse silica particles: control of size and mass fraction,"* J. Non-Crist. Solids, **104**, 95-106 (1988).

23.   M. Grun, I. Lauer and K.K. Unger, *"The synthesis of micrometer-and submicrometer-size spheres of ordered mesoporous oxide MCM-41,"* Adv. Mater., **9**, 254257 (1997).

24.   T. Nann and P. Ulvaney, *"Single quantum dots in spherical silica particles,"* Angew. Chem. Int. Ed., **43**, 5393-5396 (2004).

25. Y. Kobayashi, H. katakami, I. Mine, D. Nagao, M. Konno and L.M. Liz-Marzan, *"Silica coating of silver nanoparicles using a modified Stober method,"* J. Colloid. Interface. Sci., **283**, 392-396 (2005).

26. I. Tissot, C. Novat, F. Lefebvre and E. Bourgeat-Lami, *"Hybrid latex particles coated with silica,"* Macromolecules, **34**, 5737-5739 (2001).

27. A. Burns, H. Ow and U. Wiesner, *"Fluorescent core-shell silica nanoparticles: towards "lab on a particle" architectures for nanobiotechnology,"* Chem. Soc. Rev. , **35**, 1028-1042 (2006).

28. B.G. Trewyn, J.A. Nieweg, Y. Zhao and V.S. Lin, *"Biocompatible mesoporous silica nanoparticles with different morphologies for animal cell membrane penetration,"* Chem. Eng. J, **137**, 23-29 (2008).

29. S. Tabatabaei, A. Shukohfar, R. Aghababazadeh and A. mirhabibi, *"Experimental sudy of the synthesis and characterisation of silica nanoparticles via the sol-gel method,"* J. Phys: Conference Series, **26**, 371-374 (2006).

30. C.C. Perry and TK. Tucker, *"Biosilicification: the role of the organic matrix in structure control,"* J. Biol. Inorg. Chem., **5**, 537-550 (2000).

31. T. Coradin and P.J. Lopez, *"Biogenic silica patterning: simple chemistry or subtle biology?,"* Chem. Bio. Chem., **3**, 1-9 (2003).

32. T.P. Ding, J.X. Zhou, D.F. Wan, Z.Y. Chen, C.Y. Wang and F.Zhang, *"Silicon isotope fractionation in bamboo and its significance to the bigeochemical cycle of silicon,"* Geochim. Cosmochim. Acta, **72**, 1381-1395 (2009).

33. M. Calomme, P. Geusens, N. Demeester, G.J. Behets, P. D'Haese, J.B. Sindambiwe, V.V. Hoof and D.V. Berghe, *"Partial prevention of long term femoral bone loss in aged ovarectomized rats supplemented with choline-stabilized orthosilicic acid,"* Calcif. Tissue Int., **78**, 227-232

34. D.K. Yi, S.T. Selvan, S.S. Lee, G.C. Papaefthymiou, D. Kundaliya and J.Y. Ying, *"Silica-coated Nanocomposites of magnetic nanoparticles and quantum dots,"* J. Am. Chem. Soc, **127**, 4990-4991 (2005).

35. S.W. Ha, C.E. Camalier, G.R. Beck and J.K. Lee, *"New method to prepare very stable and biocompatible fluorescent silica nanoparticles,"* Chem. Commun., **20** 2881-2883 (2009).

36. D. Luo, E. Han, N. Belcheva and W.M. Saltzman, *"A self-assembled modular DNA delivery system mediated by silica nanoparticles,"* J. Controlled Release, **95**, 333-341 (2004).

37. J. Choi, A.A. Burns, R.M. Williams, Z.Z.A. Flesken-Nikitin, W.R. Zipfel, U. Wiesner and A.Y. Nikitin, *"Core-shell silica nanoparticles as fluorescent labels for nanomedicine,"* J. Biomed. Opt., **12**, 1-11 (2007).

38. S.M. Borisov and O.S. Wolfbeis, *"Optical biosensors,"* Chem. Rev., **108**, 423-461 (2008).

39. B. Panchapakesan, *"Nanotechnology: Part 2, Tiny technology-Tremendous therapeutic potential,"* Oncol. Issues, Nov/Dec, 20-23 (2005).

40. B. Liedgerg, C. Nylander and I. Lundstrom, *"Surface plasmon resonance for gas detection and biosensing,"* Sens. Actuators, **4**, 299-304 (1983).

41. Y. Lei, H. Chen, H. Dai, Z. Zeng, Y. Lin, F. Zhou and D. Pang, *"Electroless-plated gold films for sensitive surface plasmon resonance detection of white spot syndrome virus,"* Biosen. & Bioelectron., **23**, 1200-1207 (2008).

42. S. Szunerits and R. Boukherroub, *"Preparation and characterization of thin films of SiOx on gold substrates for surface plasmon resonance studies,"* Langmuir, **22**, 1660-1663 (2006).

43. M.G. Manera, G. Leo, M.L. Curri, P.D. Cozzoli, R. Rella, P. Siciliano, A. Agostiano and L. Vasanelli, *"Investigation on alcohol vapours/TiO2 nanocristal thin films interaction by SPR technique for sensing application,"* Sens. Actuators, B, **100**, 75-80 (2004).

44. S. Oh, J. Moon, T. Kang, S. Hong and J. Yi, *"Preparation of a sensor substrate using functionalized mesoporous silica on a gold film for surface plasmon resonance (SPR),"* J. Electroceram., **17**, 999-1003 (2006).

45. L. D. Stefano, L. Rotiroti, I. Rendina, L. Moretti, V. Scognamiglio, M. Rossi and S. D'Auria, *"Porous silicon based optical microsensor for the detection of 1-glutamine,"* Biosen. & Bioelectron., **21**, 1664-1667 (2006).

46. J.D Wright, J.V. Oliver, R.J.M. Nolte, S.J. Holder, N.A.J.M. Sommerdijk and P.I. Nikitin, *"The detection of phenols in water using a surface plasmon resonance system with specific receptors,"* Sens. Actuators, **51**, 305-310 (1998).

47. M.D. Musick, Keating C.D, L.A. Lyon, S.L. Botsko, D.J. Pena, W.D. Holliway and T.M. McEvoy, *"Metal films prepared by stepwise assembly: Construction and*

126

characterization of colloidal Au and Ag multilayers," Chem. Mater., **12**, 28692881 (2000).

48. C.R. Evans, T.A. Spurlin and B.L. Frey, *"In situ FT-IR measurements of competitive vapor adsorption into porous thin films containing silica nanoparticles,"* Anal. Chem., **74**, 1157-1164 (2002).

49. X. Wang, K. Naka, M. Zhu, H. Kuroda, H. Itoh and Y. Chujo, *"Self-organized multilayer films and porous nanocomposites of gold nanoparticles with octa(3-aminopropyl)octasilsesquioxane,"* Polym. Mater., **17**, 447-457 (2007).

50. R.D. Miller, J. Sly, V.Y. Lee, B.C. Carter and P.J. Brock, *"Versatile controlled support architectures for nano-scale construction,"* (Unpublished Results 2007).

51. G. Pistolis, A. Malliaris, D. Tsiourvas and C.M. Paleos, *"Poly(propyleneimine dendrimers as pH-sensitive controlled-release systems,"* Chem-Eur. J., **5**, 1440-1444 (1999).

52. M.Y. Hong, H.C. Yoon and H.S. Kim, *"Protein-ligand interactions of poly(amidoamine) dendrimer monolayers on gold,"* Langmuir, **22**, 2222-2226 (2003).

53. Y. Chang, S. Chen, Z. Zhang and S. Jiang, *"Highly protein-resistant coatings from well-defined diblock copolymers containing sulfobetaines,"* Langmuir, **22**, 2222-2226 (2005).

54. T.L. Clare, B.H. Clare, B.M. Nichols, N.L. Abbot and R.J. Hamers, *"Functional monolayers for improved resistance to protein adsorption: oligo (ethylene glycol)-modified silicon and diamond surfaces,"* Langmuir, **21**, 6344-6355 (2005).

55. J.L. Dalsin, B.H. Hu, B.Pl Lee and P.B. Messersmith, *"Mussel adhesive protein mimetic polymers for the preparation of nonfouling surfaces,"* JACS, **125**, 4253-4258 (2003).

56. K.V. Gobi, H. Iwasaka and N. Miura, *"Self-assembled PEG monolayer based SPR immunosensor for label-free detection of insulin,"* Biosen. & Bioelectron., **22**, 1382-1389 (2007).

57. L.A.R. Taylor, T.L. Martin, F.G. Zaugg, K.Witte, P. Indermuhle, S. Nock and P. Wagner, *"Monolayers of derivatized poly(L-lysine)-grafted poly(ethylene glycol) on metal oxides as a class of biomolecular interfaces,"* PNAS, **98**, 852-857 (2001).

58. C. Graf, D.L. Vossen, A. Imhof and A.V. Blaaderen, *"A general method to coat colloidal particles with silica,"* Langmuir, **19**, 6693-9700 (2003).

59. R. Kumar, I. Roy, T.Y. Ohulchanskyy, L.N. Goswami, A.C. Bonoiu, E.J. Bergey, K.M. Tramposch, A. Maitra and P.N. Prasad, *"Covalently dye-linked, surface-controlled, and bioconjugated organically modified silica nanoparticles as targeted probes for optical imaging,"* JACS Nano, **2**, 449-456 (2008).

60. R. Bakalova, Z. Zhelev, I. Aoki, H. Ohba, Y. Imai and I. Kanno, *"Silica-shelled single quantum dot micelles as imaging probes with dual or multimodality,"* Anal. Chem., **78**, 5925-5932 (2006).

61. T. Nann, J. Riegler, P. Nick and P. Mulvaney, *"Quantum dots with silica shells,"* P. Soc. Photo Opt. Ins., **5705**, 77-84 (2005).

62. L.M. Liz-Marzan, M. Giersig and P. Mulvaney, *"Synthesis of nanosized gold-silica core-shell particles,"* Langmuir, **12**, 4329-4335 (1996).

63. T. Nakamura, M. Mizutani, H. Nozaki, N. Suzuki and K. Yano, *"Formation mechanism for monodispersed mesoporous silica spheres and its application to the synthesis of core/shell particles,"* J. Phys. Chem. C., **111**, 1093-1100 (2007).

64. K. Nozawa, H. Gailhanou, L. Raison, P. Panizza, H. Ushiki, E. Sellier, J.P. Delville and H.H. Delville, *"Smart control of monodisperse Stöber silica particles: Effect of reactant addition rate on growth process,"* Langmuir, **21**, 1516-1523 (2005).

65. Z. Zhang, A.E. Berns, S. Willbold and J. Buitenhuis, *"Synthesis of poly(ethylene glycol) (PEG)-grafted colloidal silica particles with improved stability in aqueous solvents,"* J. Colloid. Interface. Sci., **310**, 446-455 (2007).

66. H. Wang, M. Peng, J. Zheng and P. Li, *"Encapsulation of silica nanoparticles by redox-initiated graft polymerization from the surface of silica nanoparticles,"* J. Colloid. Interface. Sci., **326**, 151-157 (2008).

67. A.V. Blaaderen and A. Vrij, *"Synthesis and characterization of monodisperse colloidal organo-silica spheres,"* J. Colloid. Interface. Sci., **156**, 1-18 (1993).

68. Y.S. Lin and C.L. Haynes, *"Synthesis and characterization of biocompatible and size-tunable multifunctional porous silica nanoparicles,"* Chem. Mater, **21**, 3979-3986 (2009).

69. D.R. Larson, H. Ow, H.D. Vishwasrao, A.A. Heikal, U. Wiesner and W.W. Webb, *"Silica nanoparticle architecture determines radiative properties of encapsulated fluorophores,"* Chem. Mater, **20**, 2677-2684 (2008).

70. F. Parayandeh, *"Increasing the sensitivity of a surface plasmon resonance biosensor,"* Graduate Thesis, (2009).

71. V.Y. Lee and R.D. Miller, *"IBM Corporation,"* private communication, (2007).

72. R.D. Miller, J. Sly, V.Y. Lee, B.C. Carter and P.J. Brock, *"Versatile controlled support architectures for nano-scale construction,"* Polym. Prepr., **47**, 929 (2006).

73. E.A. Appel, V.Y. Lee, J.L. Hedrick, R.D. Miller and J. Sly, *"Star polymers, methods of preparation thereof, and uses thereof,"* Patent Application US12/750147, (2008).

74. T.K. Miyamoto, N. Sugita, Y. Matsumoto, Y. Sasaki and M. Konno, *"A new antineoplastic methylgermanium (IV) porphyrin,"* Chem. Lett., **12**, 1695-1698 (1983).

75. L. Chang, *"Effect of coordination chemistry on layer by layer deposition of star polymers,"* Graduate Thesis, (2008).

76. B. Congjian, W. Yunkuan and H. Xingzhou, *"Surface modification of polyolefine by uv light/ozone treatment,"* J. App. Pol. Sc., **60**, 2397-2402 (1996).

77. M.J. Roberts, M.D. Bentley and J.M. Harris, *"Chemistry for peptide and protein PEGylation,"* Adv. Drug Deliver. Rev., **54**, 459-476 (2002).

78. J. Ladd, A.D. Taylor, M. Piliarik, J. Homola and S. Jiang, *"Label-free detection of cancer biomarker candidates using surface plasmon resonance imaging,"* Anal. Bioanal. Chem., **393**, 1157-1163 (2009).